Doctoral thesis (Hiroshima University)

広島大学　博士論文

Isotopic study on geochemical behavior of radionuclides in and around the natural fission reactors

天然原子炉内部とその周囲における放射性核種の地球化学的挙動に関する同位体研究

2010

Department of Earth and Planetary Systems Science,
Graduate School of Science, Hiroshima University

広島大学大学院理学研究科地球惑星システム学専攻

Makiko Kikuchi

菊池　麻希子

目次

1. 主論文

Isotopic study on geochemical behavior of radionuclides in and around the natural fission reactors

天然原子炉内部とその周囲における放射性核種の地球化学的挙動に関する同位体研究

Makiko Kikuchi

2. 公表論文

(1) Redistribution of REE, Pb and U by supergene weathering studied from in-situ isotopic analyses of the Bangombé natural reactor, Gabon.
Kikuchi M., Hidaka H., Horie K. and Gauthier-Lafaye F.
Geochimica et Cosmochimica Acta, **71**, (2007) 4716-4726.

(2) Geochemical behavior of radionuclides in highly altered zircon above the Bangombé natural fission reactor, Gabon.
Kikuchi M., Hidaka H. and Horie K.
Physics and Chemistry of the Earth, **33**, (2008) 978-982.

(3) In-situ U–Pb analyses of highly altered zircon from sediments overlying the Bangombé natural fission reactor, Gabon.
Kikuchi M. and Hidaka H.
Geosciences Journal, **13**, (2009) 257-264.

1. 主論文

Isotopic study on geochemical behavior of radionuclides in and around the natural fission reactors

天然原子炉内部とその周囲における放射性核種の地球化学的挙動に関する同位体研究

Makiko Kikuchi

Department of Earth and Planetary Systems Science,

Graduate School of Science, Hiroshima University

2010

Abstract

In-situ isotopic analyses of rare earth elements (REE), U, Pb, Zr, Mo and Ru were performed using a sensitive high resolution microprobe (SHRIMP) to investigate the migration and retardation processes of fission products in and around the natural fission reactor.

REE isotopic data of the secondary minerals found in clays and black shales above the Bangombé natural reactor show that most of fission products were effectively trapped in the clays and not distributed into the black shales over the clays, which reveals that the clays play an important role in preventing fission products from spreading. The Pb data suggest that galena grains in the clays were formed by the mixing of the two components during a recent alteration event, and that a significant amount of Pb was derived from 2.05-Ga-old original uraninite rather than reactor uraninite.

Zircon crystals in the clays above the Bangombé natural reactor heterogeneously contain high-U regions (up to 28.3 wt%) with normal $^{235}U/^{238}U$ ratios (=0.00725) and significant amounts of fissiogenic REE, which suggest the occurrence of significant chemical fractionation between REE and U during the dissolution of reactor uraninite and the recrystallization of secondary U minerals. Although the zircons in clay layer trapped most of the fissiogenic REE derived from the reactor, only the Ce isotopic ratios of the clay and black shale layers have about 2 times larger variations than the other REE. This result suggests that a large chemical fractionation between Ce and other

REE above the reactor occurred under the oxidizing condition.

The U–Pb systematics of zircon above the Bangombé natural reactor provide chronological information on the old igneous activity associated with the basement rock formation at 2.8 Ga and geochemical evidence of the incomplete mixing of independent Pb and U sources. This result is consistent with previous chronological results in this area.

Metallic aggregates with a size of a few tens of microns and consisting mainly of Ru, Rh, Pd, Te, Pb, As, Sb, S and Bi were found in the acid residue of SD37-S2/CD uraninite taken from Oklo natural reactor zone (RZ) 13. Quantitative analyses of major elements using an electron probe microanalyzer and *in situ* isotopic analyses of Zr, Mo, Ru, Pb and U using a sensitive high-resolution ion microprobe were performed on the metallic aggregates to determine the geochemical behaviors of fission products and actinides and to ascertain the processes of formation of the aggregates in the RZs. The chemical compositions of the aggregates investigated in this study are significantly different from those reported previously, showing lower Pb content and no correlation between the contents of Pb and S in the individual grains. The $^{235}U/^{238}U$ ratios in metallic aggregates vary significantly from 0.00478 to 0.01466, indicating chemical fractionation between U and Pu during the formation of the aggregates. The Pb isotopic data indicate that most of the Pb in the aggregates decayed from 2.05 Ga-old uraninite that existed in the RZ originally and that there was chemical fractionation between U and Pb in some aggregates. The Zr and Mo isotopic ratios, $^{90}Zr/^{91}Zr$ and $^{95}Mo/^{97}Mo$, for most of the aggregates had small variations, which can be simply explained by constant separate mixing of fissiogenic and nonfissiogenic components. On the other hand, a large variation in the $^{99}Ru/^{101}Ru$ ratio (0.324–1.73) cannot be

explained only by a two-component mixing theory; thus, chemical fractionation between Tc and Ru during the reactor criticality is suggested. The large variations in the $^{235}U/^{238}U$ and $^{99}Ru/^{101}Ru$ isotopic ratios suggest that the aggregates formed under various redox conditions owing to the radiolysis of water.

CONTENTS

CHAPTER 1

CHAPTER 2

CHAPTER 3

CHAPTER 4

CHAPTER 1

Introduction

1.1 Natural fission reactors

The present-day isotope ratio of $^{235}U/^{238}U$ is 0.00725 and is invariant in natural materials, a fact demonstrated by the measurement of the isotopic composition of U in numerous ore bodies by Cowan and Alder (1976). There is, however, one place on Earth that we know, where the $^{235}U/^{238}U$ ratio deviates dramatically and can be as low as 0.0038 (Gauthier-Lafaye et al., 1996). This is a group of U deposits located in the south-west part of Gabon in the Precambrian sedimentary basin of Franceville (Fig. 1). Sustained fission chain reactions occurred in these U deposits approximately 2 billion years ago.

The discovery of natural U depleted in fissile ^{235}U was made in June 1972 in the U enrichment plant at Pierrelatte in France (Bodu et al. 1972). Some samples of U ore gave a $^{235}U/^{238}U$ isotope ratio of 0.007214, some 0.5% lower than the natural value. Subsequent investigation indicated that the U deposit at Oklo was the source of the isotopic anomaly. Although various hypotheses were advanced as to the reason for this deficiency in ^{235}U, the samples from Oklo U deposit displayed convincing evidence of fission product contamination. This result provided firm evidence that the depletion in ^{235}U in these samples had been resulted from the spontaneous nuclear chain reactions at some time in the past (Neuilly et al. 1972). Before this discovery, the possibility that the chain fission reaction occurred in U ore had been proposed in some reports (e.g. Wetherill and Inghram, 1953; Kuroda, 1956). In 1956, Kuroda calculated factors

necessary to start chain fission reactions in rich U ore from Johangeorgenstadt deposit in Saxony and came to the conclusion that self-sustained fission reactions might have occurred about 2 billion years ago.

Since 1972, many programs have been conducted in order to understand the processes by which fission reactions could occur and the effects of these nuclear reactions on the surrounding rocks. An impressive amount of data on geology, geochemistry, geochronology and physics of the natural reactors was gathered and published in two conference proceeding volumes: The Oklo Phenomenon (1975) and Natural Fission Reactors (1978). Although most of the early works focused on physics and chemistry of the natural reactors, the usefulness of the Oklo deposit as natural analogues for nuclear waste disposal has been recognized since 1990s (e.g., Blanc 1996; Gauthier-Lafaye et al., 1996) and research is now mainly focused on the behavior of actinides and fission products in a geological environment.

1.2 Geological setting

1.2.1 Oklo and Bangombé uranium deposits

The Franceville basin is the host for the Oklo and the Bangombé uranium deposits and consists of five sedimentary units designated as the FA to the FE layers (Gauthier-Lafaye and Weber, 1989). The uranium deposits of the Franceville basin are the oldest known high-grade uranium deposits in the sedimentary rocks that were formed by dissolution-precipitation processes (Gauthier-Lafaye and Weber, 1989).

Uranium deposits are located at the top of a 400 to 1000 meters thick FA formation mainly made of sandstones and conglomerates. This formation is underlain by the FB formation made of black shales with organic carbon content ranging between

1 to 15% and few carbonate (dolomite) layers. In the central part of the basin the FB formation is 1000 meters thick (Gauthier-Lafaye, 1986).

Most of the uranium is of the form of uraninite and is closely associated with migrated hydrocarbons that fill the secondary porosity of the sandstone (Gauthier-Lafaye and Weber, 1981). Uranium mineralization occurred when oxidized uranium bearing fluids met reduced fluids associated with hydrocarbons in tectonic traps (Gauthier-Lafaye and Weber, 1981). The sources of uranium are believed to be detrital uranium bearing minerals such as monazite ($LaPO_4$) and thorite ($ThSiO_4$) which are concentrated in several 100 m thick conglomerates in the lower FA formation (Gauthier-Lafaye and Weber, 1989).

The Francevillian series has been dated by several geochronometers. Weber and Bonhomme (1975) summarized existing geochronological information on the Franceville Series as determined by the Rb-Sr geochronological technique when applied to clay minerals, to give a range of ages from 1.75 to 2.2×10^9 years. The U-Pb technique was used to give an ill-defined age of mineralization of the reactor zones of 1.75×10^9 years (Lancelot al., 1975), whereas Devillers et al. (1975) determined an age between 1.8 and 2.05×10^9 years by the same technique. In an attempt to clarify the conflicting age estimates of the Oklo deposit, Gancarz (1978) measured the isotopic composition of U and Pb of ten, U-rich ore samples that were located 2–8 m within the boundaries of the reactor zones. The data gave a formation age of the deposit of $(2.05\pm0.03)\times10^9$ years.

1.2.2 Reactor zones

The first reactor zones (hereafter RZ) were discovered between 1972 and 1974

in the open pit of the Oklo and were numbered 1 to 6 in the order of their discovery (Fig. 2). In 1978, three other RZs numbered 7, 8, and 9 were discovered in the open pit of Oklo. Since 1982, five other RZs, namely 10, 13, 16, OK84 (at Okelobondo site), and 15 were discovered at Oklo. Among the sixteen RZs, the early discovered RZs 1 to 9 have been weathered under oxidizing condition. On the other hand, the later discovered RZs 10 to 16 have been little weathered, because they have been located in the underground mine under more reducing environment than those of near-surface RZs 1 to 9 (Fig. 3). In addition, the small natural RZ was found at the Bangombé site 30 km south of Oklo in 1985 (Fig. 1). The size of RZs is quite variable. The biggest reactor (RZ 2) is a 12 m long, 18 m deep and 20 to 50 cm thick lens, while at Bangombé, the RZ is only 5 m long, 1 m wide and a few centimeters thick (Fig. 4(a)).

Later dykes of dolerite intrude the overall Francevillian series in the Franceville basin forming two orthogonal systems oriented NNW-SSE and ENE-WSW (Fig. 1). These dolerites were dated by K-Ar method on feldspathic fractions giving an age of 970±30 Ma (Bonhomme et al., 1982).

1.2.3 Reactor operating conditions

The conditions for the occurrence of nuclear fission reactions in a geological system have been discussed by Naudet (Naudet, 1991). Fission reactions occur spontaneously in ^{238}U resulting in the production of the fast neutrons. If these neutrons are slowed down and thermalized, they may induce fission in ^{235}U or ^{239}Pu. Four main conditions must be achieved to initiate fission reaction in a geological system:

1. The uranium content should be high in order to reach the critical mass.
2. The geological environment should have a low content in poison elements such as B

and REEs which are neutron-capturing nuclei.

3. The environment should be rich in light nuclei (hydrogen from water) which act as a neutron moderator and allows for the regulation of the nuclear reaction.

4. The uranium ore must have concentration of fissionable nuclei.

The radioactive decay constant for ^{235}U ($9.85x10^{-10}$) is smaller than that for ^{238}U ($1.55x10^{-10}$) (Jaffey et al., 1971). The concentration of ^{235}U in a 2.0 billion years old natural uranium deposit was 3.7 % as compared to 0.725 % at present. Therefore, at ages > 2.0 Ga, the $^{235}U/^{238}U$ was sufficient to sustain fission in natural reactors. However, no traces of nuclear fission reactions have been found in pre-2.0 Ga uranium deposits. High-U concentration in a sedimentary rock needs to be subjected to one or more dissolution-precipitation episodes and enough oxygen which allow oxidation-reduction reactions of U. Although the oxygen content of the atmosphere was low before 2.0 Ga, Holland (1994) has suggested that the P_{O2} level in the atmosphere increased rapidly from < 1 % PAL to > 15 % PAL during the early Proterozoic. Therefore, 2.0 Ga is a crucial age that allows a high $^{235}U/^{238}U$ ratio for the first time of the Earth's history.

Estimates of nuclear parameters for natural fission reactors rely on isotopic abundance of elements and are, therefore, sensitive to losses of elements from the system. If certain isotopes were partially released from reactors, then the calculated nuclear parameters are meaningless. The detailed age of the fission reaction was obtained by Ruffenach (1978) and Naudet (1991). They studied in detail a bore-hole (SC36) which cross-cuts RZ 2 and demonstrated that there was no migration of U and REE during the reaction. By comparing the fluence of the fission reaction to the amount of fission elements (mainly REE), it is possible to determine the date of the

fission reaction with a great precision. The result gave an age of 1950±40 Ma (Ruffenach, 1978, 1979; Holliger, 1988; Naudet, 1991).

Neutron capture on ^{238}U produces the fissionable isotope ^{239}Pu, which can decay to ^{235}U. Analyses of the isotopic composition of fission products from REE, Ru, and Pd indicated that approximately 90% of the fission reactions in Reactor Zone 2 resulted from ^{235}U fission, with only minor contributions from ^{239}Pu thermal fission and ^{238}U fast fission (Ruffenach et al., 1980). It is apparent that because approximately 50% of the ^{235}U fissions resulted from the decay of ^{239}Pu to ^{235}U, the duration of criticality must have been long relative to the half-life of ^{239}Pu (24,000 years). Ruffenach et al. (1980) reported that the duration of nuclear reactions that occurred in RZ 2 was approximately 780,000 years, but that the duration of criticality varies widely for the various RZ. Hidaka and Holliger (1998) reported that the duration time of RZ 10 and Bangombé RZ was about 10^5 years and that of RZ 13 was 2.41×10^4 years. Meshik et al. (2004) investigated the xenon isotopic ratios of aluminous hydroxyl phosphate in RZ 13 and characterized the reactor operation. The specific isotopic structure of xenon in the mineral defined a cycling operation for the reactor with 30-min active pulses separated by 2.5 h dormant periods.

The temperatures of the fluids in the reactors and during criticality have been subjected of many different studies based on microthermometric measurements of fluid inclusions (Openshaw et al., 1978; Gauthier-Lafaye, 1986). From such works, it was suggested that, the temperature in the core reached 400 °C and a convective hydrothermal system around the reactor started when fission reactions started. On the other hand, the $^{176}Lu/^{175}Lu$ ratios closely depends on the average equilibrium temperature of neutrons at the time of reactor criticality, because the effective neutron

capture cross-section of ^{176}Lu is a sensitive indicator of temperature (Holliger and Devillers, 1981). The $^{176}Lu/^{175}Lu$ ratios in the samples varied significantly from 0.0054 to 0.0254. The average temperature was calculated to be 280±50 °C. However, the calculated temperature has been considered to be underestimated temperature due to the migration of Lu during and after reactor operations and the uncertainly on the neutron capture section of ^{175}Lu (Gauthier-Lafaye et al., 1996).

1.3 Isotopic studies of the natural fission reactors

Many elements consisting of the reactor samples show variable isotopic compositions due to nuclear fission and neutron capture reactions (e.g., De Laeter and Hidaka, 2007). Therefore, isotopic studies of the reactor materials provide practical information on the long-term behavior of fission products in geological media, which is applicable to radioactive waste disposal (e.g., Gauthier-Lafaye et al., 1996; Hidaka and Holliger, 1998). Most of previous isotopic analyses for the Oklo studies were based on bulk analysis of the rock samples with chemical separation for individual elements. As the first stage of the Oklo study, retentivities of the most of the fissiogenic isotopes such as rare earth elements (REE), platinum group elements (PGE), and alkaline elements in the Oklo reactors were quantitatively determined from the isotopic data of the systematic bulk analyses (e.g. Gauthier-Lafaye et al., 1996; Hidaka and Holliger, 1998). However, some kinds of fission products are heterogeneously distributed in uranium matrices, even if they have been well retained in the RZs. In addition, even fission products having chemically good affinity with uranium might have remobilized out of the reactor in association with dissolution of reactor uraninite due to late weathering. From the mineralogical observation using scanning electron microscope

(SEM) and transmission electron microscope (TEM), partial dissolution of uraninite and recrystallization of uranium minerals in and around the RZs were confirmed (Janeczek and Ewing, 1996a; Jensen and Ewing, 2001). Therefore, for better understanding of the migration mechanism of fission products out of the RZs, it is essential to perform microscopic isotopic observation on the Oklo samples.

To address this issue, *in-situ* isotopic analyses of the micro-minerals found in the RZ and peripheral rocks have been performed by secondary ion mass spectrometry (SIMS) (Janeczek and Ewing, 1996b; Bros et al., 2003; Horie et al., 2004; Hidaka et al., 2005). SIMS has been widely applied for the *in-situ* isotopic analyses of geological samples for two decades. *In-situ* isotopic analyses of individual minerals using SIMS provide information on the detailed thermal history of geological materials.

Our major concern is when and how fission products were released from the reactor and trapped in the individual minerals. In this thesis, *in-situ* isotopic analyses of individual tiny minerals in and around reactor zones have been performed using a Sensitive High Resolution Ion Microprobe (SHRIMP). Then, we report the following topics: (1) Geochemical behaviors of fissiogenic LREE and U above the Bangombé RZ during 2.0 billion years. (2) Mechanism and timing of migration and fixation of LREE into secondary U- and REE-bearing minerals above the Bangombé RZ. (3) Geochemical behaviors of REE, U and Pb in highly altered zircons found above the Bangombé RZ and their chronological interpretations. (4) Formation processes of metallic aggregates including fissiogenic Zr, Mo, Ru, Rh and Pd found in RZ 13.

Acknowledgement

Before we move on to the substantive contents, I would like to express my gratitude to several people for helping me bring this thesis to fruition.

I would like to express my deepest gratitude to prof. Hiroshi Hidaka (Department of Earth and Planetary Systems Science, Graduate School of Science, Hiroshima University) for much patience advice in my research and critical reviews of the manuscript. Thanks must also go to prof. Kentaro Terada (Department of Earth and Planetary Systems Science, Graduate School of Science, Hiroshima University) for his valuable comments on my research and critical guidance in SHRIMP analysis. It was a pleasure to work with them.

I am very grateful to Dr. François Gauthier-Lafaye (Ecole et Observatoire des Sciences de la Terre, UMR7517-CNRS-UdS) for donate Oklo and Bangombé samples and his helpful advice for the manuscript. I am deeply grateful to Dr. Kenji Horie (National Institute of Polar Research) for his advice and cooperation in SHRIMP analysis. Thanks are also due to Yoshihiro Shibata (Hiroshima University) for EPMA analysis and Hayami Ishisako (Hiroshima University) for preparing the samples.

Special thanks are due to Yoko Shimamoto, Tomoe Hirotaka, Aya Katsube and members in our laboratory who have influenced and enhanced my research. I am so grateful to my parents, Takeshiro Kikuchi and Ruriko Kikuchi for their understanding and financial support throughout my study life.

A part of this thesis was financially supported by a doctoral fellowship grant of Japan Society for the Promotion of Science (JSPS).

CHAPTER 2

Redistribution of REE, Pb and U by supergene weathering studied from *in-situ* isotopic analyses of the Bangombé natural reactor, Gabon

The isotopic analyses of lighter REE (LREE) in micro-regions using SIMS have been effectively used to discuss the migration processes of fissiogenic isotopes into U- and REE-bearing minerals, because a large amount of LREE is produced by U fission in natural reactors. Isotopic and chemical analyses of whole rock samples from the Bangombé RZ apparently show that fissiogenic REE have been well-preserved in the RZ (Hidaka and Gauthier- Lafaye, 2000). However, from a microscopic viewpoint, a trace of fissiogenic REE was released from the RZ in association with the partial dissolution of the reactor uraninite, and formed secondary minerals in the peripheral rocks. Several kinds of secondarily formed U- and REE-bearing minerals such as florencite ($(REE)Al_3(PO_4)_2(OH)_6$) and coffinite ($USiO_4$) have been found in the peripheral rocks of the RZ (Janeczek and Ewing, 1996a). The phosphate minerals found in the host rock contain an excess of fissiogenic LREE (Janeczek and Ewing, 1996b; Dymkov et al., 1997; Hidaka et al., 2005), which suggests that the large amount of LREE in the RZ was released in association with the alteration of the reactor uraninite and precipitated as phosphate minerals. Stille et al. (2003) reported the isotopic variations of $^{143}Nd/^{146}Nd$ and $^{149}Sm/^{147}Sm$ in one of the drill cores BAX8, including the RZ, and concluded that fissiogenic REE were not detected at a distance of more than 3 m from the reactor. Therefore, in this study, we focused on the region within 1 m above and beneath the reactor.

In this study, the isotopic analyses of REE, Pb and U in U- and REE-bearing minerals found in the clay and black shale layers above the Bangombé RZ were performed using SHRIMP to understand the detailed migration profiles of depleted-U and fissiogenic REE in the clay and black shale layers and when and how the migration occurred.

2.1 Bangombé uranium deposit

The Bangombé uranium deposit is located approximately 30 km southeast from the Oklo–Okélobondo uranium deposits (Fig. 1). The Bangombé RZ is located at 11.80 m depth within the groundwater discharge area, and is significantly affected by weathering and chemical reactions due to the flow of groundwater (Fig. 4). At Bangombé uranium deposit, uranium mineralization is located at the top of the sandstone layer, which is overlain by the clay and black shale layers (Fig. 5). Closer to the surface, the main feature of Bangombé RZ is the occurrence of brown to rubefied pelites resulting from a supergene weathering of the shales. The interface between black shales and weathered pelite is marked by strong Fe oxides accumulation. Red oxides are found in all lithological facies of the bore-hole but this interface correspond probably to a major redox front (Bros et al., 1993). Because geochemical stability of uranium largely depends upon redox conditions, the Bangombé site provides a unique opportunity to study the geochemical behavior of fission products released from the uranium matrix under severe weathering. More than 20 boreholes have been drilled to investigate the geological setting of the Bangombé RZ, but only three boreholes (BA145, BAX3 and BAX8) intersect the RZ (Gauthier-Lafaye et al., 1996; Hidaka and Holliger, 1998) (Fig. 4). The intrusion of numerous dolerite dykes were caused by

regional extension in the Franceville basin, which was confirmed as several episodes of significant Pb mobilization in Late Proterozoic period (Gauthier-Lafaye et al., 1996). However, at Bangombé, the influence of the dolerite dike intrusion on the reactor chemistry is less obvious because recent weathering affects the geochemical signature of the RZ. These geological events have been considered to allow that a part of the fission products have been released from the reactor and distributed in the peripheral rocks. The migration behavior of fissiogenic REE can be discussed from the distribution profile of isotopic variations with the distance from the RZ. In early research, the isotopic data of the Bangombé site suggested that the fission products released from the RZ during recent weathering have been distributed over a distance of 1 m into a sandstone beneath the RZ (Hidaka et al., 2005), but have been retained in a clay layer above the RZ (Stille et al., 2003).

2.2 Samples

In previous study, four samples, BAX3.1215, 1225, 1240 and 1290, from the sandstone layer beneath the Bangombé RZ were used. The LREE isotopic data showed that the proportion of fissiogenic and non-fissiogenic REE components gradually change with the distance from the RZ (Hidaka et al., 2005). Three samples, BAX3.1040, 1065 and 1170, used in this study were collected from BAX3. The sub-number (four digits) of each sample corresponds to its depth in the BAX3 borehole in centimeters. The reactor part of Bangombé corresponds to BAX3.1180. BAX3.1170 consists of clays from 10 cm above the reactor (Fig. 5). BAX3.1040 and 1065 are black shales taken from 140 and 115 cm above the RZ, respectively. The black shales include fine fractures filled with iron and manganese oxides.

Because the sizes of individual samples from black shale and clay layers used in this study were limited, they were not large enough to perform mineral separation. Therefore, each sample was cut and mounted on an epoxy resin disk of 2.5 cm diameter. Then, the surface of the sample was polished with 1/4 μm diamond paste.

2.3 Analytical procedures

2.3.1 Mineral observation and quantitative analysis by EPMA

Before SHRIMP analysis, an electron probe micro analyzer (EPMA: JEOL JXA-8200) was used for quantitative analysis of major elements and for obtaining back-scattered electron (BSE) images of individual grains.

In this study, coffinite, françoisite ($(REE)(UO_2)_3O(OH)(PO_4)$), U-rich inclusions coexisting with galena (PbS), and zircon ($ZrSiO_4$) were found in the clays. On the other hand, no REE minerals of over 1 μm length were found in the black shales of the drill-core. Only uranium-rich phases of less than 1 μm (hereafter micro-uraninite) were included in the matrices of the black shales. BSE images of typical U- and REE-bearing minerals measured in this study are shown in Fig. 6(A–F). Besides the U- and REE-bearing minerals, number of fine galena grains (Fig. 7(A) as a typical example) and zircon crystals (Fig. 7(C)) were also found in the clay. The quantitative analysis of Pb-rich area by EPMA revealed that a few galena grains in the clay layer coexist with anglesite ($PbSO_4$) (Fig. 7(B)). Detailed microscopy observation and Raman spectrum analysis indicated that a large quantity of anglesite grains exist along the cracks in the clay samples (Fig. 8). The results of quantitative analyses of zircon grains were performed using analytical spot size of 3 μm and the electron beam current

was 50 nA at 15 kV of acceleration voltage. The 91500 zircon was used as a reference material for the determination of U concentration by EPMA analysis. As the results, the quantitative analysis revealed that the zircon grains found in the clay layers are heterogeneous grains containing the various U concentrations up to 2.83×10^5 ppm.

2.3.2 *In-situ* isotopic analyses by SHRIMP

SHRIMP II at Hiroshima University was used for *in-situ* isotopic analyses in this study. For the REE measurements, the mass resolution was set to higher than 8800 (M/ΔM at 1% of peak height) to avoid the isobaric interferences of the oxide and unknown species onto atomic REE ion peak. The masses of ^{140}Ce, ^{142}Ce+^{142}Nd, ^{143}Nd, ^{144}Sm+^{144}Nd, ^{145}Nd, ^{146}Nd, ^{147}Sm, ^{148}Nd, ^{149}Sm, ^{150}Nd+^{150}Sm, ^{151}Eu, ^{152}Sm, ^{153}Eu, ^{155}Gd, ^{156}Gd+^{156}Dy, ^{157}Gd, ^{158}Gd+^{158}Dy, ^{160}Gd+^{160}Dy and ^{161}Dy were scanned for the isotopic analyses. ^{142}Ce, ^{144}Sm and ^{150}Sm isotopic abundances can be obtained from the subtraction of the ^{142}Nd, ^{144}Nd and ^{150}Nd isotopic abundances, respectively, because the isotopic abundances of ^{142}Nd, ^{144}Nd and ^{150}Nd can be predicted from those of ^{145}Nd, ^{146}Nd and ^{148}Nd (Hidaka et al., 2005). Similarly, ^{156}Gd, ^{158}Gd and ^{160}Gd isotopic abundances were calculated after the subtraction of the isobaric interference of the Dy isotopes from the ^{161}Dy isotopic abundance, although the isotopic abundances of ^{156}Dy, ^{158}Dy and ^{160}Dy were negligibly low (Horie et al., 2004).

For the Pb isotopic analysis of galena, the masses of ^{204}Pb, ^{206}Pb, ^{207}Pb and ^{208}Pb were scanned with a mass resolution of 5800. For U–Pb analyses of zircon, ^{196}Zr2O, ^{204}Pb, ^{206}Pb, ^{207}Pb, ^{208}Pb, ^{238}U, ^{248}ThO and ^{254}UO peaks were measured with a mass resolution of 5800. For the U–Pb data calibration of zircon samples, FC1 (^{206}Pb/^{238}U = 0.1859, 1099 Ma) was used as a standard material (Paces and Miller, 1993). In

addition, SL13 (U content = 238 ppm) was also used as a standard material for the determination of U concentration.

2.4 Results and discussion

2.4.1 REE distribution in REE- and U-bearing minerals

The REE isotopic ratios of the individual minerals found in the clays (BAX3.1170) and those of the micro-uraninite in the black shales (BAX3.1065 and 1040) are listed in Table 1. Fission and neutron capture are main reactions that cause the significant isotopic anomalies of the elements in a natural reactor. The ^{140}Ce, ^{142}Ce, ^{143}Nd, ^{146}Nd, ^{147}Sm, ^{149}Sm, ^{151}Eu and ^{153}Eu isotopes of the samples measured in this study include the fissiogenic component as well as the non fissiogenic component, because they are not shielded by β^- decay. Considering the fission product yields of individual isotopes, the $^{140}Ce/^{142}Ce$ isotopic ratios of the samples are expected to be lower than those of the non-fissiogenic standard sample ($^{140}Ce/^{142}Ce = 7.73\pm0.03$). On the other hand, the $^{143}Nd/^{146}Nd$ and $^{151}Eu/^{153}Eu$ isotopic ratios of the samples are expected to be higher than those of the standard samples ($^{143}Nd/^{146}Nd = 0.735\pm0.01$ and $^{151}Eu/^{153}Eu = 1.092\pm0.002$). The $^{149}Sm/^{147}Sm$ ratios are expected to be lower than those of the standard materials ($^{149}Sm/^{147}Sm = 0.906\pm0.001$) because of the extremely large neutron capture cross-section of ^{149}Sm. The most important difference in mineralogy between BAX3 and the other drill cores is the occurrence of uraninite with coffinite and phosphatian U-minerals. The coffinite and posphatian minerals are considered to be formed by supergene weathering (Stille et al., 2003; Gauthier-Lafaye et al., 2004). The isotopic data of $^{140}Ce/^{142}Ce$, $^{143}Nd/^{146}Nd$ and $^{149}Sm/^{147}Sm$ show clear

evidence of the incorporation of fissiogenic isotopes in the minerals, while those of $^{151}Eu/^{153}Eu$ are unclear because of the low fission-product yields of ^{151}Eu and ^{153}Eu. The isotopic variations of $^{140}Ce/^{142}Ce$, $^{143}Nd/^{146}Nd$ and $^{149}Sm/^{147}Sm$ values depend upon the proportion of the fissiogenic component relative to the total fraction of individual minerals. Fig. 9 shows the depth-dependent variations of $^{140}Ce/^{142}Ce$, $^{145}Nd/^{146}Nd$, $^{149}Sm/^{147}Sm$ and $^{153}Eu/^{151}Eu$ isotopic ratios of REE- and U-bearing minerals in the BAX3 drill core. The isotopic data from previous works are also plotted in the same figure (Janeczek and Ewing, 1996b; Hidaka and Gauthier-Lafaye, 2000; Hidaka et al., 2005). The vicinity of the RZ, corresponding to BAX3.1180, has the lowest $^{140}Ce/^{142}Ce$ (2.209) and $^{149}Sm/^{147}Sm$ (0.1010) values and the highest $^{145}Nd/^{146}Nd$ (1.025) and $^{153}Eu/^{151}Eu$ (1.230) values, as shown in Table 1(A). These isotopic ratios gradually change with the distance from the reactor in the sandstone layer (1215–1290), which reveals that supergene weathering led to the redistribution of fissiogenic REE. However, the variations of the isotopic ratios above the RZ (BAX3.1050 to 1180) are different from those under the RZ. The isotopic variations of Ce, Nd and Sm in the clay layer (BAX3.1170) are much larger than those in the sandstones (BAX3.1225, 1240 and 1290) and black shales (BAX3.1040 and 1065), which indicates that the migration of fissiogenic LREE was limited. The variations of the isotopic ratios of REE drastically change in the clay, while the isotopic ratios gradually change with the distance from the reactor in the sandstone. Our isotopic data suggest that most of the fissiogenic Ce, Nd and Sm were effectively trapped in the clays, and not moved to the black shales. This result provides a practical illustration of the performance of a clay barrier in the uptake of fission products by adsorption onto clays and their incorporation in secondarily formed U- and REE-bearing minerals. Gd isotopic compositions are

strongly affected by neutron capture reactions, because ^{155}Gd and ^{157}Gd have large neutron-capture cross sections and become ^{156}Gd and ^{158}Gd, respectively (Hidaka and Masuda, 1988; Hidaka and Holliger, 1998; Horie et al., 2004). Therefore, the isotopic depletion of ^{155}Gd and ^{157}Gd corresponds to the enrichment of ^{156}Gd and ^{158}Gd, respectively. If the Gd isotopic compositions of the samples are affected by only neutron capture reactions, the isotopic ratios $(^{155}Gd+^{156}Gd)/^{160}Gd$ and $(^{157}Gd+^{158}Gd)/^{160}Gd$ should be constant because of the isotopic balance between the depletion of ^{155}Gd and ^{157}Gd and the enrichment of ^{156}Gd and ^{158}Gd. As shown in Table 1(B), the ratios of both $(^{155}Gd+^{156}Gd)/^{160}Gd$ and $(^{157}Gd+^{158}Gd)/^{160}Gd$ for coffinite-1 to coffinite-3 grains are in good agreement with those of the standard material within analytical precision. However, the corresponding isotopic ratios of coffinite-4 and the U-rich inclusion are 5–7% higher than those in the standard material, which reveal isotopic evidence of the addition of a fissiogenic Gd component as well as neutron-capture products in the samples.

2.4.2 Pb isotopic evolution of galena

Although the chronological interpretation of U–Pb and Pb–Pb data from the Oklo and Bangombé samples is often complicated because of the significant mobilization of Pb due to later igneous events (Gauthier-Lafaye et al., 1996), detailed comparison of the Pb isotopic data makes it possible to discuss the alteration history of the Oklo and Bangombé sites since the deposition of uranium ores (Mathieu et al., 2001; Evins et al., 2005; Hidaka et al., 2005). The Pb isotopic data of galena in the clay sample (BAX3.1160) are listed in Table 2. The variation of $^{207}Pb/^{206}Pb$ (0.1157–0.1362) is small and correlates with that of $^{204}Pb/^{206}Pb$. The Pb isotopic data

of galena grains from the clay layer (BAX3.1160) are plotted in Fig. 10. For comparison, the Pb data of secondary U minerals from the sandstone layer beneath the RZ (BAX3.1215 to 1290) are also plotted in the same figure. The Pb isotopic data points of individual minerals including galena measured in this study are plotted on the same single line. The Pb data of the secondary U minerals plotted on the single line can be explained by two-component mixing between the 2.05-Ga-old original uraninite and the reactor material including fissiogenic isotopes (Hidaka et al., 2005). Uraninite and U-rich goethite from the BAX3.1290 sandstone showed normal U isotopic compositions ($^{235}U/^{238}U$ = 0.00725) and higher $^{207}Pb^*/^{206}Pb^*$ ratios (0.126–0.128) corresponding to those 2.05 Ga, which represent the older original minerals as an end-member of the two-component mixing model. The data suggest that Pb in secondary U minerals was derived from uraninite with normal isotopic composition and not from the fissioned uraninite. All of the Pb data points of the galena measured in this study are close to those of the 2.05-Ga-old original minerals. The Pb data suggest that the galena grains in the clay were also formed by the mixing of the two components during a recent alteration, and that a significant amount of Pb was derived from 2.05-Ga-old original uraninite rather than reactor uraninite.

2.4.3 Isotopic characterization of zircon

2.4.3.1 U and REE isotopes

The seven zircon grains found in the BAX3.1170 sample show a wide range of UO_2 content from < 0.01 to 2.83×10^5 ppm. BSE images of the zircon grains are shown in Fig. 7(C). Two grains, numbered zircon 1 and 5, partly remain in a euhedral shape

with an oscillatory zonal structure, and include numerous fractures. REE and U isotopic data of the zircon grains are summarized in Table 3. Although the U-rich region of individual zircon grains shows a normal $^{235}U/^{238}U$ ratio (=0.00725) within analytical uncertainties, it includes fissiogenic REE. Uraninite found in the sandstone (BAX03.1290) also has normal $^{235}U/^{238}U$ ratios and REE isotopic anomalies (Hidaka et al., 2005), suggesting the occurrence of chemical fractionation between REE and U during the recrystallization of secondary U minerals. The depleted U from the RZ was partially dissolved and mixed with a large amount of normal U from non reactor materials.

2.4.3.2 U–Pb chronological interpretation

In-situ U–Pb dating of detrital zircon grains helps us to understand the thermal history of the sediments. However, as described in the previous section, the zircon crystals in this study include numerous high-U regions in micro-scale. Generally, it is difficult to determine an accurate $^{206}Pb/^{238}U$ ratio for high-U zircon from *in-situ* isotopic analysis because of the inaccurate U–Pb calibration between the standard material and the analyzed samples (Williams and Hergt, 2000). The conventional U–Pb calibration technique is not appropriate for high-U zircon, because high-U zircon might have a different chemical composition from the standard zircon. Williams and Hergt (2000) studied the relationship between the SHRIMP U/Pb ages and the U contents of zircon, and revealed that the calibrated $^{206}Pb/^{238}U$ data increases as a function of U content over 2500 ppm. Therefore, in this study, only four analytical data with U concentrations of less than 2500 ppm (zircon 1-1, 1-3, 2-2 and 3-4 in Fig. 7(C)) were selected from 13 analytical spots, and used as reliably calibrated SHRIMP U–Pb data. In addition, the

$^{206}Pb/^{238}U$ ratios of the other nine analytical spots with high-U contents (zircon 1-2, 1-4, 1-5, 3-3, 3-4, 4-5, 5-1, 5-2 and 7-1 in Fig. 7(C)) were determined from the analytical combination of U/Pb elemental ratios obtained by EPMA and Pb isotopic compositions obtained by SHRIMP. Although the U contents of zircon 1-2, 1-4 and 1-5 were less than 2500 ppm, SHRIMP analysis could not provide good statistics. Therefore, the three sets of data were collected from EPMA analysis. The U contents from 11 analytical spots (zircon 3-1, 3-2, 4-1, 4-2, 4-3, 4-4, 5-3, 6-1, 6- 2, 6-3 and 7-2), showing more than 2500 ppm by SHRIMP analysis, were not determined by EPMA, because the analytical regions in the grains were partly damaged after several SHRIMP analyses. Therefore, the 13 data sets from 24 analytical spots are used for further discussion. Fig. 11 shows a Tera-Wasserburg Concordia diagram. All of data from the 13 analytical spots from the six zircon grains are listed in Table 4. If U–Pb decay system works as a chronometer, we can generally discuss geochronological history of the sample from the data points of $^{238}U/^{206}Pb$ and $^{207}Pb/^{206}Pb$ on a Concordia diagram. However, in this case, in spite of the large variation of the $^{238}U/^{206}Pb$ data from 0.2 to 18, the $^{207}Pb/^{206}Pb$ ratios show a small variation except for two data points (0.1924 from zircon 1-1 and 0.1387 from zircon 2-2). The result suggests the existence of independent U and Pb sources that have migrated into zircon. Judging from the $^{207}Pb/^{206}Pb$ ratios (=0.115–0.126) commonly observed especially in the low-U/Pb parts of the zircon, the migrated Pb into the zircon was probably derived from the same source as that which formed the galena.

In Fig. 11, the Pb isotopic data of the zircon are plotted in the same region of those of the galena. Furthermore, high $^{238}U/^{206}Pb$ points such as the analytical spots 5-1 and 5-2 show slightly higher $^{207}Pb/^{206}Pb$ ratios (0.122–0.126) than the other points

($^{207}Pb/^{206}Pb < 0.12$), which also supports the incomplete mixing of independent Pb and U sources in this system. Previous Pb isotopic studies of U- and REE-bearing minerals in the sandstones beneath the Bangombé RZ show that a large mobilization of Pb, U and fissiogenic isotopes occurred by dolerite dyke intrusion (~0.8 Ga ago), and that the secondary minerals were formed by mixing between 2.05-Ga-old original minerals (non-depleted U) and reactor materials (depleted U) during a recent alteration (Hidaka et al., 2005). The similarity of the Pb isotopic compositions suggests that the additional Pb and U fractions in the altered part of the zircon in the clay originated from the same sources as those of the secondary minerals in the sandstones. The U–Pb data from the analytical spots 1-1, 2-1 and 2-2 are different from the others, suggesting chronological information on the old igneous activity associated with the basement rock formation. The three data points appear to form a single line with a different trend from the other 10 data points. The U–Pb diagram in Fig. 11 suggests that the U–Pb system of the inherited zircon was also disturbed by the mixing of the materials having $^{207}Pb/^{206}Pb$ ~0.12 with a low U content ($^{238}U/^{206}Pb$ <0.5). As shown in Fig. 11, the intercept of the U–Pb Concordia and the single line consisting of the three data points gives a U–Pb age of 2.80 Ga, probably corresponding to the formation age of the basement rocks. Mathieu et al. (2001) reported an age of 2.87 Ga from the SHRIMP U–Pb analyses of two zircon crystals in the basement rocks. Ages of 2.7–2.9 Ga are reported for U–Th–Pb chemical ages of six of the 79 monazite crystals found in the FA sandstones and conglomerates (Montel et al., 1996). Therefore, it is reasonable to consider that the two zircon crystals are detrital materials derived from the basement in this site.

2.5 Conclusions

The isotopic data using a SHRIMP clearly show the distribution patterns of the fissiogenic REE isotopes from the RZ to the peripheral rocks. The isotopic variations of fissiogenic REE in the clay layer are much larger than those in the sandstone and black shales. The variations of the isotopic ratios of REE drastically change in the clay, while the isotopic ratios gradually change with the distance from the reactor in the sandstone. Our data demonstrate the important role of clays in effectively adsorbing the fission products released from the RZ.

The zircon crystals in the clays heterogeneously contain a U-rich region (up to 28.3 wt%) with normal $^{235}U/^{238}U$ ratios (=0.00725) and significant amounts of fissiogenic REE, which indicate the migration of U-rich fluid in the grain. Although crystalline zircon is generally considered to be durable under most geochemical conditions, highly damaged zircon in this study showed significant migration of U and REE.

From the Pb–Pb data of galena, it is interpreted that the galena grains in the clay were also formed by the mixing of the two components during a recent alteration, and that the significant amount of Pb was derived from 2.05-Ga-old original uraninite rather than reactor uraninite.

The U–Pb systematics of zircon provides chronological information on the old igneous activity associated with the basement rock formation at 2.8 Ga and geochemical evidence of the incomplete mixing of independent Pb and U sources.

CHAPTER 3

Geochemical behavior of REE and U in highly altered zircon above the Bangombé natural reactor and their geochronological interpretations

As shown in CHAPTER 2, it was revealed that the U- and REE-bearing minerals and zircon grains in the clay layer above the Bangombé RZ effectively trapped large amounts of the fissiogenic REE derived from the reactor and prevented them migrating into the black shale layer. This result agrees with the depth-dependent variations of Nd and Sm isotopic ratios in BAX8 obtained from whole rock analyses in Stille et al. (2003). In BAX8 drill core, the Nd and Sm isotopic ratios in the clay layer are dramatically varied due to the contribution of fissiogenic components. On the other hand, there is no contribution of fissiogenic Nd and Sm in the black shale layer. The REE isotopic data above the Bangombé RZ suggest that the geochemical behaviors of fissiogenic REE in the clay layer and near the boundary between clay and black shale layers are very important to understand fixation and retardation effects of radionuclides above the RZ. However, the detailed geochemical behaviors of fissiogenic REE at the boundary have not been obvious yet. Although the secondary U- and REE-bearing minerals in the black shale layer have been rarely found, detrital zircon grains exist in both of the clay and black shale layers. Since zircon grains are resistant to the weathering due to their high physico-chemical stability, it is considered that zircon could be less affected by the severe supergene weathering in comparison with secondary U- and REE-bearing minerals. Therefore, zircon may be useful to understand the mechanism of migration of fissiogenic components above the Bangombé RZ.

On the other hand, zircon is also powerful tool to interpret chronological

information on migration of fissiogenic and radiogenic nuclides around the RZ. Indeed, seven zircon grain found in the clay layer provide chronological information on the old igneous activity associated with the basement rock formation at 2.8 Ga and geochemical evidence of the incomplete mixing of independent Pb and U sources. However, it was revealed that the zircons above the Bangombé RZ have various U contents (up to 28.3 wt. %) and the conventional calibration methods for U-Pb in SHRIMP analysis cannot be applied to the high-U zircons over 2500 ppm. For further discussion of chronological interpretation around the Bangombé RZ, we have to check the reliability of the calibration technique in the case of high-U zircon.

In this study, the zircons found in the clays and black shales near the boundary of the clay and black shale layers were analyzed by EPMA to check the U contents. Then, the isotopic analyses of REE, Pb and U in zircon grains were performed using SHRIMP to understand the detailed migration profiles of depleted-U and fissiogenic REE in the clay and boundary of the clay and black shale layers and when and how the migration occurred.

3.1 Sample preparation

Two samples, BAX3.1130 and 1170 were taken from the BAX3 drill-core. The sub-number (four digits) of each sample corresponds to depth location of the BAX3 drill-core in cm. The sample BAX3.1170 is clay from 10 cm above the reactor (Fig. 5). The sample BAX3.1130 is black shales taken near the boundary of the clay and black shale layers, which is 50 cm above the reactor.

Block samples from BAX3.1170 and 1130 were mounted on a resin disk of 2.5 cm and the surfaces were polished with 1/4 μm diamond paste.

3.2 Analytical procedures

3.2.1 Quantitative analysis by EPMA

EPMA (JEOL JXA-62 8200) was used for quantitative analysis of Al, Si, Ca, Mn, Fe, Zr, Hf, Pb, Th and U and for obtaining back-scattered electron (BSE) images of individual zircon grains. The analytical spot size was 3 μm and the electron beam current was 50 nA at 15 kV of acceleration voltage. The 91500 zircon was used as a reference material for the determination of U concentration by EPMA analysis. As a result, 48 zircons of which 29 were in BAX3.1170 and 19 in BAX3.1130 were identified and they show a wide range of U-contents from <0.01 to 2.22×10^5 ppm (Table 5 and Figs. 12 and 13).

3.2.2 *In-situ* isotopic analyses by SHRIMP

The isotopic analyses of REE, U and Pb in the zircon grains were performed by SHRIMP II at Hiroshima University. The analytical methods for REE isotopic analyses by SHRIMP are described in section 2.3.2 (CHAPTER 2).

3.2.2.1 U-Pb calibration methods in U-rich zircons

In-situ U–Pb analysis of zircon using an ion microprobe has been widely applied to understand the detailed thermal history of geological samples because zircon is a common accessory mineral in many type of rocks and suited for the U–Pb dating due to the incorporation of large amounts of U and little initial Pb during their formation. The difference of ionization efficiencies between U and Pb during the analysis gives

rise to the necessity of calibration between secondary ion ratios ($^{206}Pb^{+}/^{238}U^{+}$) and isotopic ratios ($^{206}Pb/^{238}U$) for in-situ U–Pb dating. The U/Pb calibration technique was established from the comparison of the data between standard and analyzed zircon grains (e.g., Compston et al., 1984). However, previous study indicated that the conventional U–Pb calibration technique is not appropriate for the high-U zircon, because the high-U zircon is considered to have a different chemical composition from the standard zircon in SHRIMP (e.g., McLaren et al., 1994; Williams and Hergt, 2000; Butera et al., 2001; Zeck and Williams, 2002). According to Williams and Hergt (2000), the Pb/U of zircons having U < 2500 ppm were well-corrected by conventional SHRIMP calibration techniques, but the data of zircons over 2500 ppm U increase at a rate of between 1.5 and 2.0% per thousand ppm U. The problems with U–Pb calibration for high-U zircon have been also reported in Cameca IMS1270 analyses (Lee and Whitehouse, 2007). Since high-U zircon including U concentration more than 2500 ppm is rarely found, up to the present, relatively few studies have been reported on how to calibrate the U–Pb isotopic data obtained by SHRIMP analysis.

3.2.2.2 In-situ U-Pb analysis by SHRIMP

A few nA beam of O_2^- primary ion was used to sputter a 10 μm analytical spot on the sample. Before the SHRIMP measurements, the Pb/U elemental ratios of three spots around the analytical spots in EPMA measurements were determined from EPMA. In this study, the analytical spots where the Pb/U ratios of three spots were consistent within ±10% variation were considered as candidates for SHRIMP measurements. Overall, 46 analytical spots from 33 zircon grains were selected for SHRIMP measurement and show a wide range of U contents from <100 to 59000 ppm. For

U–Pb analyses, $^{196}Zr_2O$, ^{204}Pb, background (at mass 204.1), ^{206}Pb, ^{207}Pb, ^{208}Pb, ^{238}U, ^{248}ThO and ^{254}UO peaks were measured with a mass resolution of 5800 (M/ΔM at 1% of peaks height). For the U–Pb calibration of zircon samples, FC1 ($^{206}Pb/^{238}U$ = 0.1859, 1099 Ma) was used as a standard material (Paces and Miller, 1993). In addition, SL13 (U content = 238 ppm) was also used as a standard material for the determination of U concentration. Correction for common Pb was done by measuring ^{204}Pb. Common Pb in the zircon analyzed in this study can originate mainly from two sources. One is initial Pb incorporated into the zircon crystal at the formation. The isotopic composition of initial Pb was estimated from two stage evolution model (Stacey and Kramers, 1975). The other is initial Pb added to the zircon from uraninite through the dissolution of uraninite. The isotopic composition of initial Pb originated from the uraninite was assumed as $^{206}Pb/^{204}Pb$ = 18.61 and $^{207}Pb/^{204}Pb$ = 15.75 from galena inclusions in the altered zircon in FA sandstone layer at Bangombé (Mathieu et al., 2001). The radiogenic $^{207}Pb/^{206}Pb$ isotopic ratios corrected by the two methods were consistent within the analytical errors because of significantly large amounts of radiogenic Pb against non-radiogenic Pb.

3.3 Results and discussion

3.3.1 REE distribution in zircons

Table 6 and Fig. 14 show the $^{140}Ce/^{142}Ce$, $^{145}Nd/^{146}Nd$, $^{149}Sm/^{147}Sm$ and $^{153}Eu/^{151}Eu$ isotopic ratios of the zircons found in the clay (BAX3.1170) and black shale layers (BAX3.1130) above the reactor. The isotopic ratios of Nd, Sm and Eu in the clay layer exhibit large variations ($^{143}Nd/^{146}Nd$ = 0.598–1.004, $^{149}Sm/^{147}Sm$ =

0.528–0.819 and $^{153}Eu/^{151}Eu$ = 1.093–1.139), which is a result of the mixture of fissiogenic with non-fissiogenic component at various rates. On the other hand, the isotopic ratios of Nd, Sm and Eu in the black shales layer are almost similar with standard values, which indicate little contamination of fissiogenic component. These differences of the isotopic ratios between the clay and black shale layers show that the migration of Nd, Sm and Eu into the black shale layer was limited and most of the fissiogenic Nd, Sm and Eu derived from the reactor was probably adsorbed by clays. However, the large isotopic variation of Ce in the clay ($^{140}Ce/^{142}Ce$ = 2.86–8.04) was similarly observed in the black shale layers ($^{140}Ce/^{142}Ce$ = 3.43–7.03). Magnification of the isotopic variation of Ce in the clay is about 2 times larger than other REE. This is isotopic evidence for significant migration of fissiogenic Ce into the black shale layer and large chemical fractionations between fissiogenic Ce and other REE occurred during the migration from the reactor to the black shale layer.

3.3.2 Chemical fractionation of REE in zircon grains

The depth-dependent variations of REE suggest that Ce and other REE released from the reactor have a different behavior above the reactor. Hidaka et al. (2005) reported that the elemental abundances of Ce in REE-bearing minerals of the sandstone layer under the reactor are ~5 times larger than that of Nd, Sm and Eu due to a change of oxidizing state from Ce^{3+} to Ce^{4+}. Fig. 15 shows diagrams for isotopic ratios of two different elements, Ce–Nd, Sm–Nd and Eu–Nd, of zircon. The data for standard material and the reactor sample are also plotted in the same figure. The REE components in the individual minerals resulted from mixing between the two end-members, non-fissiogenic (STD) and fissiogenic (reactor) materials (Hidaka et al.,

2005). All data points in the diagrams for $^{149}Sm/^{147}Sm$ vs. $^{145}Nd/^{146}Nd$ and $^{153}Eu/^{151}Eu$ vs. $^{145}Nd/^{146}Nd$ can be explained by two-component mixing between STD and reactor materials with a little fractionation factor (Nd:Sm:Eu = 1:1–5:0.5–2). On the other hand, the data for $^{140}Ce/^{142}Ce$ vs. $^{145}Nd/^{146}Nd$ show a large chemical fractionation of Ce relative to Nd (Ce:Nd = 1–50:1). One of major reasons to make a large fractionation of Ce from other REE is a difference of oxidizing states. Under the oxidizing condition, Ce is compatible in zircon because the ionic charge and radius of Ce^{4+} (0.97 Å) are closer to Zr^{4+} (0.84 Å) than those of other $LREE^{3+}$ (Ce^{3+} 1.143 Å, Nd^{3+} 1.109 Å, Sm^{3+} 1.079 Å and Eu^{3+} 1.066 Å). In addition, the Ce concentration in altered zone of the present suite of zircons is extremely higher (1–2 wt.%) than that in typical zircons (e.g., 3–160 ppm (Hoskin and Schaltegger, 2003)) and the Ce concentration was occurred during the intensive alteration (Utsunomiya et al., 2007). Considering these geochemical processes, the chemical fractionation between Ce and other REE observed in this study results from the chemical characteristics of the altered zircon under the oxidizing condition and severe weathering. The presence of significant amount fissiogenic Ce in the clay and black shales layers suggests that fissiogenic Ce existed as Ce^{3+} and Ce^{4+} above the reactor, and fissiogenic Ce^{3+} and other trivalent REE which escaped from trapping in the clay layer finally migrated into the black shale layer. Then, increase of the amount of Ce^{4+} formed from Ce^{3+} in the black shale layer under the more oxidizing condition led to the mixing of fissiogenic Ce into altered zircons around the boundary of the clay and black shale layers.

3.3.3 U–Pb chronological interpretations

The data of 46 analytical spots from 33 zircon grains were selected for *in-situ*

U–Pb analyses by SHRIMP and/or EPMA, and are listed in Table 7. Although all of the analytical data were once reduced by conventional SHRIMP calibration method, it was considered that the $^{238}U/^{206}Pb$ isotopic data deviate from the accurate $^{238}U/^{206}Pb$ isotopic data due to their wide variations of U contents (<100 to 59000 ppm). Therefore, the fractional difference ($\Delta^{206}Pb/^{238}U$) between the $^{206}Pb/^{238}U$ data measured by EPMA and SHRIMP versus U content was plotted to check whether the bias between $^{206}Pb/^{238}U$ and U content as reported in Williams and Hergt (2000) can be identified from the altered zircons in this study (Fig. 16). If the $\Delta^{206}Pb/^{238}U$ in analyzed zircon is due to the inaccurate calibration, a plot in Fig. 16 should have a slope equivalent to a bias about 1.5 to 2.0% per 1000 ppm U as observed in high-U unaltered zircon analyzed by Williams and Hergt (2000). However, Fig.16 shows that there is no clear correlation between $\Delta^{206}Pb/^{238}U$ and U content in analyzed zircons. The reason for the scattered data points especially in high-U content region (>5000 ppm U) in Fig.16 might be that the high-U zircons have incorporated uranium derived from uraninite in and around Bangombé RZ. Therefore, the U/Pb correction by Williams and Hergt (2000) could not be applied for the analyzed zircons in this study. In Fig. 16, large variations of $\Delta^{206}Pb/^{238}U$ appear beyond 2000-3000 ppm U. Moreover, even if some of the analyzed zircons have not incorporated uranium derived from uraninite, the conventional Pb/U calibration technique does not function for high- U zircon over 2500 ppm U as reported in Williams and Hergt (2000). Therefore, calibrated SHRIMP $^{206}Pb/^{238}U$ data for the zircons having <2500 ppm U were directly adopted. On the other hand, the $^{206}Pb/^{238}U$ data with high-U concentration over 2500 ppm were determined by the analytical combination of U/Pb elemental ratios by EPMA and Pb isotopic compositions by SHRIMP. The analytical data of zircons with U

concentration less than 2500 ppm are shown in Table 7(A), in which the U–Pb data and U concentration were obtained by SHRIMP analyses. On the other hand, those with U concentration more than 2500 ppm are shown in Table 7(B), in which the U–Pb data by SHRIMP and EPMA and U concentration by EPMA are also listed. In order to calculate a $^{238}U/^{206}Pb$ elemental ratio from the analytical data of EPMA, $^{235}U/^{238}U$ ratio is essential. The $^{235}U/^{238}U$ ratios obtained by SHRIMP analyses are shown in Table 7, which indicates that large numbers of $^{235}U/^{238}U$ ratios are slightly lower or higher than a normal $^{235}U/^{238}U$ (= 0.00725). The depletion of ^{235}U suggests that the depleted-U derived from fission reactions of ^{235}U in the reactor zone ($^{235}U/^{238}U$ = 0.005855 ± 0.000003) migrated into zircon grains above the reactor zone. Although the excess of ^{235}U is rare, a few examples have been observed in clay mineral and apatite (e.g., Bros et al., 1993; 1996; Horie et al., 2004). The ^{235}Uenrichment can be interpreted as the selective uptake of ^{239}Pu produced by neutron-captured ^{238}U. Previous works suggested that the chemical fractionation between U and Pu might be occurred in associated with a locally oxidizing condition arising from radiolysis of water (Savary and Pagel, 1997; Horie et al., 2004).

Fig.17 shows Tera-Wasserburg U–Pb Concordia diagrams. In Fig. 17(a), all of the SHRIMP data including high-U zircons were reduced with the conventional calibration method. On the other hand in Fig. 17(b), the data derived from the analytical spots having U concentrations less than 2500 ppm were obtained by the conventional calibration technique and those more than 2500 ppm were obtained by the analytical combination of EPMA and SHRIMP. The detailed comparison of two data sets between Fig. 17(a) and (b) indicates that most of the $^{238}U/^{206}Pb$ values having U > 2500 ppm calibrated by the conventional method (Fig. 17(a)) are lower than those

estimated from U/Pb elemental ratios by EPMA analyses (Fig. 17(b)). However, the both U–Pb data between Fig. 17(a) and (b) have same tendencies in low $^{238}U/^{206}Pb$ region ($^{238}U/^{206}Pb < 7$), which allows us to understand the geological history in this site. If the U–Pb decay system works as a chronometer, the individual data on a concordia diagram provide geochronological information. The U–Pb data in Fig. 17 suggest that the U–Pb decay system of the zircons above the reactor zone are largely disturbed and the data in the diagram have mainly two trends derived from at least three-components (points A, B and C in Figs. 17(a) and (b)). One of three end-members (point A in Figs. 17(a) and (b)) corresponds to a concordant U–Pb age of 2.8 Ga. Two zircon grains plotted on the mixing line of components A and B are from the sample in CHAPTER 2 and showed higher crystallinity than the other zircon grains in Raman spectroscopic analysis and have low U concentrations less than 400 ppm. As shown in section 2.4.3.2 (CAHPTER 2), the SHRIMP U–Pb analyses of two zircon crystals in the basement rock have shown the age of 2.8 Ga (Mathiue et al., 2001). Therefore, it is reasonable to consider that at least two zircon grains plotted on the mixing line of components A and B were derived from the basement rock in this site. The other two end-members (points B and C in Figs. 17(a) and (b)) have the large variation of the $^{238}U/^{206}Pb$ data from 0.23 to 38.8 and the small variation of $^{207}Pb/^{206}Pb$ data (most values are near 0.11–0.12), which suggests the existence of independent U and Pb sources that have migrated into zircon grains. Judging from the $^{207}Pb/^{206}Pb$ ratios commonly observed especially in low U/Pb parts of the zircon, the migrated Pb into the zircon was probably derived from the same source as that which formed the galena above the Bangombé RZ. The previous studies revealed that the U and Pb originated 2.05-Ga old uraninite have occurred a large chemical fractionation under recent severe

weathering within one million years (Hidaka et al., 2005). Because the $^{207}Pb/^{206}Pb$ data show a small variation of ~0.12 corresponding to the mean age of 1959 ± 12 Ma selected from 23 of 46 as the best of the zircon analyses, U and Pb of these two components were originated from 2.05-Ga old uraninite and migrated into zircon grains independently under the recent severe weathering.

3.4 Conclusions

The isotopic data using a SHRIMP clearly show the distribution patterns of the fissiogenic REE isotopes from the RZ to the peripheral rocks. The zircon in the clay layer effectively trapped large amounts of the fissiogenic Nd, Sm and Eu derived from the reactor and prevented them migrating into the black shale layer. On the other hand, Ce isotopic ratios of the zircons in the clay and black shale layers have larger variations than those the other REE. This is clear evidence of a large chemical fractionation between Ce and other REE above the reactor caused by the chemical characteristics of the altered zircon under the oxidizing atmosphere and severe weathering condition.

The conventional U–Pb calibration technique for *in-situ* SHRIMP zircon analysis does not always function especially for high-U zircon (>2500 ppm U), as Williams and Hergt (2000) pointed. However, the bias of $^{206}Pb/^{238}U$ with U content over 2500 ppm could not be identified in this study. Therefore, the conventional calibration technique was applied to only the zircons with U < 2500 ppm. High-U zircon grains having U over 2500 ppm were determined by the analytical combination of U/Pb elemental ratios by EPMA and Pb isotopic composition by SHRIMP. The U–Pb data of zircons provide chronological information on the igneous activity associated with the basement rock formation at 2.8 Ga and geochemical evidence of the

incomplete mixing of independent Pb and U sources originated from 2.05-Ga old uraninite under the recent severe weathering.

CHAPTER 4

Formation and geochemical significance of micrometallic aggregates including fissiogenic platinum group elements in the Oklo natural reactor, Gabon

The long-term behavior of radioactive isotopes in the geosphere is of great interest in terms of establishing an underground nuclear waste repository. Studies of natural analogues in uranium and thorium deposits provide information on fixation and/or release processes of radioactive isotopes in geological formations over long periods of time (e.g., Cramer and Smellie, 1992; Maravic and Smellie, 1992). Among the natural analogues, the Oklo uranium deposit is considered a unique and important example because of the large-scale fission reactions that occurred 1.95 Ga ago (Gauthier-Lafaye et al., 1996).

Since the discovery of the first reactor zone (hereafter RZ) in 1972 (Bodu et al., 1972; Neuilly et al., 1972), 16 RZs have been identified in the Oklo uranium deposit and numbered in the chronological order of their discovery (Fig. 2). Among these 16, RZs 1 to 9 were discovered during open pit mining operations and have since undergone considerable weathering under the prevailing oxidizing condition near the surface. On the other hand, RZs 10 to 16, which were discovered later, have experienced only a little weathering because they are located in an underground mine in a more reducing environment (Fig. 3).

One of the major concerns is to identify the factors that control the mobility and retention of fission products in geological media. Radionuclide migration out of the RZs was caused mainly by three events. During the criticality, there was extensive

hydrothermal alteration due to the heat of nuclear reactions (Gauthier-Lafaye et al., 1989). After the criticality, the RZs were altered 1000–700 Ma ago by regional extension and the intrusion of the Neoproterozoic dykes (Bonhomme et al., 1978; Gauthier-Lafaye et al., 1996; Evins et al., 2005), and finally by recent alteration and supergene weathering (Janeczek and Ewing, 1996a, 1996b; Stille et al., 2003).

The chemical states of fission products in artificially irradiated nuclear fuels obtained from elemental analyses have indicated that fissiogenic Mo, Tc, Ru, Rh, Pd, Ag, Cd, In, Sn, Sb and Te form metallic precipitates (Kleykamp, 1985). The first transmission electron microscope observation of the alloy particles in light-water reactor spent fuel was performed by Thomas and Guenther (1989), and alloy particles referred to as epsilon phase were found to exist in the fuel-clad gap or at the boundaries of fuel grains. The chemical compositions of the epsilon phase extracted from spent fuel vary in a narrow range and the average composition (wt.%) is 32.7% Mo, 40.5% Ru, 7% Tc, 4.2% Rh, 11.7% Pd and 3.8% Te (Cui et al., 2004). Similar aggregates (in common parlance, metallic aggregates) have been found in RZs 10 and 13 of the Oklo uranium deposit (Gauthier-Lafaye et al., 1996; Hidaka et al., 1993, 1999; Utsunomiya and Ewing, 2006), and in sandstone below the Bangombé RZ (Janeczek, 1999). The aggregates consist of several fine minerals intergrown with galena (PbS) and U minerals (Gauthier-Lafaye et al., 1996). The sizes of the aggregates range from a few microns to 100 μm. In particular, larger-sized aggregates with diameters of ~100 μm were found in the sample SD37-S2/CD collected from RZ 13 (Gauthier-Lafaye et al., 1996). The chemical compositions of the aggregates found in RZ 13, determined by electron probe microanalysis (EPMA), are mainly Pb, Ru, Rh, Te, U, As and S, with the average composition (wt.%) being 38.89% Pb, 33.51% Ru, 4.64% Rh, 2.71% Te, 0.39% U,

7.99% As and 7.43% S (Hidaka et al., 1999). There is good correlation between the Ru-Rh-Te-As-S content and Pb-S content, suggesting that the aggregates are a mixture of these two components (Gauthier-Lafaye et al., 1996; Hidaka et al., 1999). Considering complexly mixed textures of the aggregates observed using a high-resolution transmission electron microscope, Utsunomiya and Ewing (2006) suggested that dissolution and precipitation occurred within the aggregates in association with As-bearing and Pb-rich fluids.

Ru isotopic compositions of the Oklo samples can be used to deduce Tc behavior because ^{99}Tc decays to ^{99}Ru with a relatively long half-life of 2.1×10^5 years. ^{99}Tc is an isotope of great concern in safety assessments of nuclear waste repositories as it can contribute significantly to the calculated dose for 10,000 years after repository closure (e.g., Chen et al., 2000). Previous isotopic studies of whole rocks using Oklo reactor samples indicated that the isotopic abundance of ^{99}Ru expected from the experimentally obtained fission product yield deviates from the measurement values (Fréjacques et al., 1975; Curtis, 1986). The deviations of fissiogenic ^{99}Ru can be interpreted as an addition or depletion of ^{99}Tc, and suggest the occurrence of chemical fractionation between Ru and Tc in RZs. Although all of the ^{99}Tc has already decayed to ^{99}Ru at the Oklo site, the geological behavior of fissiogenic ^{99}Tc in the RZs can be inferred from the isotopic composition of fissiogenic ^{99}Ru. As the metallic aggregates in RZs constitute the host phase for large amounts of fissiogenic Mo, Ru, Rh and Pd, microscale analyses of the individual aggregates are necessary for further discussion. *In situ* isotopic analyses of the aggregates found in RZs 10 and 13 employing secondary ion mass spectrometry (Gauthier-Lafaye et al., 1996; Hidaka et al., 1993, 1999) revealed a more selective incorporation of ^{99}Tc than Ru in the metallic aggregates.

There are scant data on Ru isotopic compositions of individual metallic aggregates. Therefore, the purpose of this study is to understand the long-term geological behavior of fission products and actinides such as Zr, Mo, Tc, Ru and U incorporated in the metallic aggregates from *in situ* isotopic analyses. Moreover, we propose to discuss the prevailing processes and conditions during the formation of metallic aggregates, as predicted from chemical and isotopic compositions measured in this study.

4.1 Reactor zone 13 in Oklo uranium deposit

RZ 13 was discovered in 1984 at the south dome of the Oklo uranium deposit (Fig. 2). Although RZ 13 is a small reactor which is 30 cm thick, 6 m wide, and 10 m long, its vicinity has a very high uranium content (up to 87%) with highly depleted ^{235}U (down to $^{235}U/^{238}U = 0.0038$) (Gauthier-Lafaye et al., 1996). RZ 13 exists between two galleries, SD35 and SD37. The sample SD37-S2/CD used in this study was collected from an area with the highest depletion of ^{235}U ($^{235}U/^{238}U = 0.004630$) within the borehole SD37-S2 in RZ 13 (Holliger, 1993). Although both the RZs of 10 and 13 contain metallic aggregates that show certain degrees of alteration in weathering and redox conditions, they have different distances from the dolerite dykes, RZ 13 being closer (25 m) whereas RZ 10 is far away (Fig. 2). Large scale of U and Pb mobilization in RZ 13 in association with the dolerite dike dated 860 Ma has been reported (Holliger, 1992, 1995; Nagy et al., 1993; Gauthier-Lafaye et al., 1996; Evins et al., 2005). In addition, significant differences in the nuclear characteristics of RZ 13 from those of other RZs are known and they are as follows: (1) The proportion of ^{238}U fission of SD37 is extremely high at 18% of the total fission, while those of other RZs

are less than 5.0%. (2) Estimated criticality duration time of SD37-S2/CD is shorter ($2.42x10^4$ years) than those of other RZs (2.0 to $8.0x10^5$ years), although the neutron fluence is nearly the same as those of others (Hidaka and Holliger, 1998).

4.2 Sample preparation

A few grams of the SD37-S2/CD were leached with 2M HNO_3 in order to completely dissolve uraninite in the matrix and the residues were collected for this study. The residues were then mounted on epoxy resin, and polished with 1/4 μm diamond paste.

4.3 Analytical procedures

4.3.1 Quantitative analyses by EPMA

Before conducting a sensitive high-resolution ion microprobe (SHRIMP) analysis, EPMA (JEOL JXA-8200) was performed to quantitatively determine the major elements and obtain back-scattered electron (BSE) images of individual aggregates. The analytical spot size for the quantitative analysis was 2 μm, and the electron beam current was 20 nA at an acceleration voltage of 15 kV. The EPMA data were calibrated using reference materials consisting of pure metals (Ru, Rh, Pd, Te and Bi in ASTIMEX METM25-44) and compounds (UO_2, GaAs, PbS, $CuFeS_2$, NiO and Sb_2S_3). The analysis lines and crystals used were Ru Lα, Rh Lα, Pd L β, Te Lα, Bi Mα, U M β, As Lα, Pb Mα, S Kα, Cu Kα, Ni Kα and Sb Lα and LiF for Ni and Cu, TAP for As and PET for Ru, Rh, Pd, Te, Bi, U, S, Pb and Sb. The average limits of detection were 240 ppm for Ru, 250 ppm for Rh, 430 ppm for Pd, 250 ppm for Te, 360

ppm for Bi, 410 ppm for U, 240 ppm for As, 370 ppm for Pb, 90 ppm for S, 350 ppm for Cu, 260 ppm for Ni and 250 ppm for Sb. As a result, 34 aggregates were identified by EPMA in this study. Fig. 18 shows BSE images of typical metallic aggregates measured in this study. The BSE images indicate that the sizes of the aggregates range from <10 μm to 50 μm, and the aggregates seem to be polyphase grains consisting of fine particles smaller than the micron scale (Figs. 18(a) and (b)). Major elements of the aggregates are Ru, Rh, Pd, Te, Pb, As, S and Bi. In addition, the existence of U, Sb, Ni and Cu as minor elements in the aggregates was confirmed.

4.3.2 *In-situ* isotopic analyses by SHRIMP

Although the concentrations of Mo and Zr in the aggregates were below the detection limit of quantitative EPMA (less than 0.01 wt.%), they could be measured through SHRIMP analysis. In this study, 14 relatively large aggregates (larger than 20 μm) were selected from 34 aggregates for *in situ* isotopic analysis. The isotopic analyses of Zr, Mo, Ru, Pb and U were performed using SHRIMP II at Hiroshima University. A nanoamp-scale beam of O_2^- primary ions was used to sputter a 5 μm analytical spot on the individual aggregates. The peaks of ^{90}Zr, ^{91}Zr, ^{92}Zr+^{92}Mo, ^{94}Zr+^{94}Mo, ^{95}Mo, ^{96}Zr+^{96}Mo+^{96}Ru, ^{97}Mo, ^{98}Mo+^{98}Ru, ^{99}Ru, ^{100}Mo+^{100}Ru, ^{101}Ru, ^{102}Ru+^{102}Pd, ^{104}Ru+^{104}Pd, ^{204}Pb, ^{206}Pb, ^{207}Pb, ^{208}Pb, ^{235}U and ^{238}U were measured with a mass resolution of 5800 (M/ΔM at 1% of the peak height) using a 80 μm wide source slit and a 100 μm wide collector slit.

An ASTIMEX metal standard mount METM 25-44 was used as the standard material of nonfissiogenic isotopes, and isotopic analyses in terms of Zr, Mo and Ru

were performed to confirm the analytical precision and the instrumental mass fractionation. Since the mass numbers of 92, 94, 96, 98, 100, 102 and 104 have isobaric interference for Zr, Mo and Ru isotopic measurements in SHRIMP analysis, only the isotopic ratios of $^{90}Zr/^{91}Zr$, $^{97}Mo/^{95}Mo$ and $^{99}Ru/^{101}Ru$ are discussed in this study. The isotopic ratios, $^{91}Zr/^{90}Zr$, $^{97}Mo/^{95}Mo$ and $^{99}Ru/^{101}Ru$, in the standard materials were corrected for instrumental mass fractionation by an exponential law using the values of $^{94}Zr/^{90}Zr = 0.3381$, $^{96}Mo/^{95}Mo = 1.0527$ and $^{96}Ru/^{101}Ru = 0.3249$ as normalization factors (Minster and Ricard, 1981; Poths et al., 1987; Wieser et al., 2007). For the convenience of comparing with previous isotopic data (Hidaka et al., 1994; Bros et al., 2003), the Zr isotopic data were finally treated as $^{90}Zr/^{91}Zr$ after conversion from $^{91}Zr/^{90}Zr$.

Only after the analyses for Zr, Mo and Ru were conducted, Pb and U isotopic analyses were performed separately. For Pb and U isotopic analyses, NIST SRM610 glass was used as the standard material. In the case of U isotopic analysis, AS3 standard zircon ($^{235}U/^{238}U = 0.00725 \pm 0.00004$) was also measured to check the terrestrial U isotopic ratio.

4.4 Results

4.4.1 Chemical compositions of metallic aggregates

Twenty-two analytical spots from 14 typical metallic aggregates were selected for EPMA in this study. The data of the chemical compositions are presented in Table 8. Data previously obtained for metallic aggregates in RZs 10 and 13 (Gauthier-Lafaye et al., 1996; Hidaka et al., 1999) are also presented for comparison.

The chemical compositions of the aggregates investigated in this study are significantly different from those for RZs 10 and 13 reported previously. In this study, we used the same sample SD37-S2/CD that was used previously to find metallic aggregates (Hidaka et al., 1999). This suggests that the heterogeneity of the metallic aggregates in the sample is extremely high.

The Pb contents in the aggregates (1.24–4.49 wt.%) found in this study are lower than those of other aggregates in RZs 10 and 13 (14.16–59.02 wt.%) reported previously. Hidaka et al. (1999) reported the data of chemical compositions of individual aggregates in RZ 13, and demonstrated a good correlation between Ru+Rh+Te+As+S and PbS components. Therefore, the metallic aggregates are considered to have been formed by the mixing of two end-members: one component being mainly Ru, Rh and Te produced by fission and the other being galena existing in the RZ uraninite. However, the aggregates found in this study show no correlation between the contents of Pb and S, which suggests that the Pb does not exist in the aggregates as galena (Fig. 19(a)). A positive correlation between the contents of Pb and U was observed in this study (Fig. 19(b)). This result implies that a major part of the Pb in the aggregates found in this study might be radiogenic Pb derived from U.

The fundamental difference between metallic aggregates in natural reactors and epsilon phase in spent fuel is their chemical forms; the metallic aggregates are bound to As or S (or both), while the epsilon phase has a metallic bond (e.g., Janeczek, 1999). The metallic aggregates have been considered to be affected by hydrothermal fluids bearing As, S and other trace metals derived from the criticality and/or intrusion of dolerite dyke (Utsunomiya and Ewing, 2006). In previously reported studies, all of the metallic aggregates found in RZs 10 and 13 have shown a positive correlation among

Ru-, Rh- and Pd-As (Gauthier-Lafaye et al., 1996; Hidaka et al., 1999). However, the aggregates investigated in this study show different trends among the concentrations of Ru, Rh, Pd and As. The concentration of Ru has a clear negative correlation with that of As (Fig. 20(a)), while that of Pd has a positive correlation with that of As (Fig. 20(b)). The concentration of Rh has no correlation with that of As. These results suggest that the fissiogenic Ru, Rh and Pd have different chemical behaviors in the aggregates. The concentration of Ru in the aggregates has a clear positive correlation with that of Cu (Fig. 20(c)). The concentrations of Ru and Cu have negative correlations with the concentration of As and no discernible correlation with the concentration of S. Therefore, we can reasonably surmise that Ru and Cu might exist in the aggregates as an alloy. Judging from the correlations of elements, two main phases might compose the metallic aggregates found in this study: Ru-Cu phase and Rh-Pd-Te-Pb-U-As-S-Bi-Sb-Ni phase. In the Rh-Pd-Te-Pb-U-As-S-Bi-Sb-Ni phase, Rh has coexisted with Te and S, and Pd has coexisted with As, Bi, Pb, U and Sb. On the other hand, the concentration of As is also positively correlated with the concentrations of Te and Ni. Therefore, it is possible that some phases have congregated in the As-bearing phase in the aggregates in a complicated manner.

The average ratios of Ru/Rh/Te in RZs 10 and 13 have been reported as 36/7/1 and 12/2/1 (Te = 1), respectively (Gauthier-Lafaye et al., 1996; Hidaka et al., 1999), which would reflect the conditions of the reactor operation and the degrees of alteration by thermal events through intrusion of the dolerite dyke. The average ratio of Ru/Rh/Te in the aggregates observed in this study is 13/2/1. Although the chemical compositions differ between the aggregates in this work and those in the work of Hidaka et al. (1999), especially the contents of Pb and S, the ratios of Ru/Rh/Te are

almost the same. This suggests that the effects of hydrothermal fluid that led to the migration of Pb and the precipitation of PbS would have been different in the local area of RZ 13 while the fissiogenic Ru, Rh and Te have been well preserved in the aggregates since they were formed.

4.4.2 Isotope distribution in metallic aggregates determined by *in situ* SHRIMP analysis

4.4.2.1 Uranium

The $^{235}U/^{238}U$ isotopic ratios in 14 metallic aggregates of RZ 13 measured in this study are presented in Table 9 and plotted in Fig. 21. The $^{235}U/^{238}U$ ratios of metallic aggregates (0.00478–0.01466) have large variations compared with the standard value (0.00725). Depletion of ^{235}U is commonly observed in and around the RZs because of the consumption of ^{235}U by fission. Besides the depleted $^{235}U/^{238}U$ in the whole rock sample SD37-S2/CD, two metallic aggregates found in RZ 13 also show depleted $^{235}U/^{238}U$ of the order of 0.0038 (Gauthier-Lafaye et al., 1996). The enriched $^{235}U/^{238}U$ ratios have been observed only in a few samples of clay minerals and apatite, around the reactor zone (Bros et al., 1993, 1996; Horie et al., 2004). In the Oklo RZs, ^{239}Pu was produced by fast neutron capture of ^{238}U. The presence of excess ^{235}U has been explained by the mechanism of selective incorporation of ^{239}Pu into specific minerals after the incidence of chemical fractionation between U and Pu, as ^{239}Pu decays to ^{235}U with a half-life of 2.4×10^4 years (Bros et al., 1993, 1996; Horie et al., 2004). The enriched $^{235}U/^{238}U$ isotopic ratio observed in apatite around RZ 10 has been explained by the chemical fractionation between U and Pu in an oxidizing condition made

possible by a rise in the concentration of radiolytic oxygen (Horie et al., 2004).

4.4.2.2 Lead

As described in section 4.4.1, the metallic aggregates investigated in this study have extremely low Pb contents and a portion of Pb in the aggregates might be of radiogenic origin from RZ uraninite. This result may provide a clue to understanding the formation processes of the metallic aggregates, as the aggregates investigated in this study appear to have been formed under a different condition or at a different time compared with the previously found aggregates. The chronological interpretation of Pb-Pb data in the Oklo samples is complicated owing to the significant mobilization of Pb due to the intrusion of the dolerite dyke (Gauthier-Lafaye et al., 1996). Therefore, only a detailed comparison of the Pb isotopic data would make a discussion on the origin of the Pb component in the metallic aggregates possible.

The Pb isotopic data of 12 metallic aggregates are presented in Table 9 along with the previously generated data of aggregates in SD37-S2/CD (Gauthier-Lafaye et al., 1996). Moreover, to ascertain the evolutionary history of Pb isotopes, the $^{204}Pb/^{206}Pb$ vs. $^{207}Pb/^{206}Pb$ data of the metallic aggregates are plotted in Fig. 22. The Pb in metallic aggregates at the Oklo site is assumed to have had two modes of origins: (1) Pb originated from galena, which originally existed in uraninite matrices and/or was precipitated by the thermal event accompanied by the intrusion of the dolerite dyke, and (2) radiogenic Pb was derived from RZ uraninite. The Pb isotopic data of galena and uraninite in RZ 13 are also plotted in Fig. 22 for comparison. As shown in Table 9 and Fig. 22, all of the $^{207}Pb/^{206}Pb$ and $^{208}Pb/^{206}Pb$ isotopic ratios in this study (0.091–0.121 and 0.00715–0.00894, respectively) are lower than those of the aggregates reported

previously (0.1259–0.1266 and 0.01376–0.01413, respectively) and galena (0.12990 and 0.01382, respectively) in SD37-S2/CD. The difference in Pb isotopic ratios was perhaps due to the mode of origin of Pb in the aggregates. The lower $^{204}Pb/^{206}Pb$, $^{207}Pb/^{206}Pb$ and $^{208}Pb/^{206}Pb$ isotopic ratios observed in the aggregates found in this study are similar to those of the native lead found in RZs (0.00012–0.00013, 0.10160–0.10170 and 0.00613–0.00614, respectively), which are also plotted in Fig. 22 for comparison. Native lead has been found in RZs 10 and 13 and is considered to contain radiogenic lead from highly depleted ^{235}U (Gauthier-Lafaye et al., 1996). Since the Pb in the aggregates does not bond to S and may be radiogenic Pb derived from U, the mode of origin of Pb in some aggregates having depleted ^{235}U is considered similar to that of native lead.

4.4.2.3 Zirconium

Zr has five stable isotopes with mass numbers of 90, 91, 92, 94 and 96, and all are produced by fission. The $^{90}Zr/^{91}Zr$ ratios obtained in 14 metallic aggregates are presented in Table 10 and Fig. 24(a), together with isotopic ratios of fissiogenic and nonfissiogenic Zr. Fissiogenic $^{90}Zr/^{91}Zr = 0.9456$ presented in Table 10 is calculated from the fission yield of ^{90}Zr relative to ^{91}Zr (England and Rider, 1988) after taking into consideration the fission inventory for ^{235}U, ^{238}U and ^{239}Pu in SD37-S2/CD (Hidaka et al., 1999). The $^{90}Zr/^{91}Zr$ ratios of metallic aggregates (1.648–2.651) show that the $^{90}Zr/^{91}Zr$ data of the aggregates are between fissiogenic and nonfissiogenic $^{90}Zr/^{91}Zr$ ratios (0.9456 and 4.659, respectively). This result indicates that the Zr isotopic compositions in the aggregates are attributed to a mixture of two components: nonfissiogenic Zr from native material and fissiogenic Zr from RZ material. However,

the data of three analytical spots (metallic aggregates 2-1, 2-2 and 3-2) show significant excess of the ^{90}Zr isotope. The BSE image of metallic aggregates 2-1 and 2-2 in Fig. 18(a) shows the existence of microinclusions in the aggregates. Moreover, the existence of silicates of U and Zr has been reported in the aggregates found in RZ 10 (Gauthier-Lafaye et al., 1996). Therefore, the mixing ratios of fissiogenic and native Zr might be different in such an inclusion from those of Ru-, Rh- and Pd-rich regions.

4.4.2.4 Molybdenum

The ^{97}Mo/^{95}Mo isotopic ratios for 14 metallic aggregates are presented in Table 10 and Fig. 24(b). The results indicate that the Mo isotopic compositions (^{97}Mo/^{95}Mo = 0.817 ± 0.005–0.932 ± 0.005) are due to mixing between fissiogenic and nonfissiogenic Mo (^{97}Mo/^{95}Mo = 0.9768 and 0.5986 ± 0.0002). In addition, the ^{97}Mo/^{95}Mo isotopic ratios are consistent among all aggregates. This consistency suggests that the mixing ratios of fissiogenic and nonfissiogenic Mo were the same in all metallic aggregates.

4.4.2.5 Ruthenium

Ru is a minor element in common crustal rock, but is present in high quantities in RZs because of the high fission yields of Ru (Loss et al., 1989). Ru has seven stable isotopes with mass numbers of 96, 98, 99, 100, 101, 102 and 104. Among these seven Ru isotopes, ^{99}Ru, ^{101}Ru, ^{102}Ru and ^{104}Ru are produced by fission, while ^{96}Ru, ^{98}Ru and ^{100}Ru (shielded by ^{96}Zr, ^{98}Zr and ^{100}Mo, respectively) are not produced in any appreciable quantity by fission. The ^{99}Ru/^{101}Ru isotopic ratios measured in this study

are presented in Table 10 and Fig. 24(c). Figure 24(c) also contains a plot of the expected fissiogenic and nonfissiogenic $^{99}Ru/^{101}Ru$ (0.7550 and 1.136). The figure shows significant deviations of the $^{99}Ru/^{101}Ru$ ratios measured in this study from the expected values assumed from mixing between the expected fissiogenic and nonfissiogenic $^{99}Ru/^{101}Ru$. The deviations of $^{99}Ru/^{101}Ru$ ratios from the expected fissiogenic value in the Oklo samples have been recognized to be a result of chemical fractionation between Ru and Tc, as ^{99}Ru is produced by ^{99}Tc with a relatively long half-life of 2.1×10^5 years (e.g., Fréjacques et al., 1975; Curtis, 1986; Hidaka et al., 1993, 1999). Indeed, the metallic aggregates reported by Hidaka et al. (1993) have shown the presence of enriched $^{99}Ru/^{101}Ru$, the existence of which is interpreted as a case of selective uptake of ^{99}Tc into metallic aggregates under a reducing condition. On the other hand, the depleted $^{99}Ru/^{101}Ru$ in the metallic aggregates has never been reported. An isotopic enrichment and depletion of ^{99}Ru have been observed in uraninite matrices (Hidaka et al., 1993, 1999). Such a variation of the ^{99}Ru isotopic abundance in uraninite samples is considered to have been caused by the presence of a local oxidizing condition in UO_2 matrix due to the radiolysis of water. The U isotopic ratios in the aggregates investigated in this study suggest that the aggregates might have been affected by the radiolysis of water and that the redox conditions changed locally. The variation in $^{99}Ru/^{101}Ru$ confirms a change in the redox condition in the aggregates during the reactor operation.

4.5 Discussion

4.5.1 Effect of the radiolysis of water

Radiolysis of water is commonly observed when the spent fuel is directly exposed to groundwater, where both oxidants (OH*, H_2O_2, HO_2* and O_2) and reductants (hydrated electrons (e_{aq}^-), H* and H_2) are produced. Interestingly, the radiolysis of water being effectively catalyzed by Pd (as a model for noble metal particles) has been reported (Nilsson and Jonsson, 2008). Therefore, radiolysis of water in the metallic aggregates in the natural reactors is envisaged, and this reaction has led to oxidizing and reducing conditions inside the aggregates.

4.5.2 Chemical fractionation

4.5.2.1 U and Pu

Aggregates that contain O, Zr, Mo, Ru, Pd, U and Pu have been observed in spent fuel (Buck et al., 2004). The individual particles forming the aggregates are only a few microns across, and the particles that contain O, Zr, U and Pu are mixed within the aggregates. Likewise, the metallic aggregates could well have incorporated a part of the RZ uraninite containing O, Zr, U and Pu during their formation. U rather than Pu very likely underwent selective dissolution within the oxidized area owing to the radiolysis of water in the aggregates, which resulted in chemical fractionation between U and Pu. The ratios of chemical fractionation between U and Pu could have led to the heterogeneous distribution of ^{235}U and depletion and enrichment of $^{235}U/^{238}U$ in the aggregates.

4.5.2.2 U and Pb

U in the aggregates is considered to have been derived from the 2.05 Ga-old

uraninite in RZ. The incorporation of the 2.05 Ga-old uraninite of RZ in the metallic aggregates perhaps occurred 1.95 Ga ago when the fission chain reactions of ^{235}U were initiated and the formation of fissiogenic platinum group element (PGE) particles began. The chemical fractionation between U and Pu must have completed during the reactor operation because of the short half-life of ^{239}Pu. After the chemical fractionation, the radiogenic Pb isotopic compositions should vary depending on the $^{235}U/^{238}U$ isotopic ratio. $^{235}U/^{238}U$ vs. $^{207}Pb/^{206}Pb$ of the metallic aggregates is plotted in Fig. 6. In the absence of chemical fractionation between U and Pb since the deposition of the Oklo uraninite 2.05 Ga ago, the $^{207}Pb/^{206}Pb$ isotopic ratio of the aggregates can be expressed as a function of the $^{235}U/^{238}U$ isotopic ratio:

$$\left(\frac{^{207}Pb}{^{206}Pb}\right) = \left(\frac{^{207}Pb}{^{206}Pb}\right)_{2.05\ Ga} - \left(\frac{^{235}U}{^{238}U}\right)_n \cdot \frac{\exp(\lambda_5 t) - 1}{\exp(\lambda_8 t) - 1} + \left(\frac{^{235}U}{^{238}U}\right) \cdot \frac{\exp(\lambda_5 t) - 1}{\exp(\lambda_8 t) - 1},$$

where $(^{207}Pb/^{206}Pb)$ is the calculated $^{207}Pb/^{206}Pb$ ratio of the metallic aggregates, $(^{207}Pb/^{206}Pb)_{2.05\ Ga} = ^{207}Pb/^{206}Pb$ is derived from normal U for 2.05 billion years after the consideration of common lead ($^{206}Pb/^{204}Pb = 18.61$, $^{207}Pb/^{204}Pb = 15.74$ (Mathieu et al., 2001)), $(^{235}U/^{238}U)_n$ is the normal $^{235}U/^{238}U$ ratio, λ_5 is the decay constant of ^{235}U, λ_8 is the decay constant of ^{238}U, t is the age of the criticality (1.95×10^9 a), and $^{235}U/^{238}U$ is the varying $^{235}U/^{238}U$ ratio.

The calculated $^{207}Pb/^{206}Pb$ values are shown in Fig. 23 and are seen to increase linearly with $^{235}U/^{238}U$ (see the line denoted "f = 1" in Fig. 23). Although the $^{207}Pb/^{206}Pb$ ratios of the aggregates measured in this study have a positive correlation with $^{235}U/^{238}U$ ratios, the measured values deviate from the calculated values as the $^{235}U/^{238}U$ ratio rises. The deviations of the measured values from the calculated values can be explained by various ratios of chemical fractionation between U and Pb in each

aggregate. The possible major events that led to U–Pb chemical fractionation are considered to have occurred during the reactor operation 1.95 Ga ago and/or during the intrusion of the dolerite dyke 0.86 Ga ago (Utsunomiya and Ewing, 2006). However, our result in Fig. 23 suggests the occurrence of U–Pb fractionation during the reactor operation because the deviations between measured and calculated values increase with an increase in the $^{235}U/^{238}U$ ratio. As described in section 4.4.2.1, the $^{235}U/^{238}U$ ratios of the aggregates changed with the degree of chemical fractionation between U and Pu under various redox conditions during the reactor operation. Since the chemical behaviors of U and Pb differ, the occurrence of chemical fractionation between U and Pb during the dissolution of U from the aggregates is considered reasonable. Assuming that the chemical fractionation between U and Pb occurred during the reactor operation, the $^{207}Pb/^{206}Pb$ isotopic ratio of the aggregates can be calculated as

$$\left(\frac{^{207}Pb}{^{206}Pb}\right)_f = \left(\frac{^{207}Pb}{^{206}Pb}\right) \times f + \left(\frac{^{207}Pb}{^{206}Pb}\right)_{Pb} \times (1-f)$$

$$\left(\frac{^{207}Pb}{^{206}Pb}\right)_{Pb} = \left(\frac{^{207}Pb}{^{206}Pb}\right)_{2.05\ Ga} - \left(\frac{^{235}U}{^{238}U}\right)_n \cdot \frac{\exp(\lambda_5 t) - 1}{\exp(\lambda_8 t) - 1},$$

where $(^{207}Pb/^{206}Pb)_f$ is the calculated $^{207}Pb/^{206}Pb$ ratio of the metallic aggregates during chemical fractionation between U and Pb 1.95 Ga ago, f is the proportion of the nonfractionated U and Pb component relative to the total fraction, $(^{207}Pb/^{206}Pb)$ is the nonfractionated U and Pb component, and $(^{207}Pb/^{206}Pb)_{Pb}$ is the fractionated Pb component 1.95 Ga ago. The $(^{207}Pb/^{206}Pb)_f$ values calculated using f = 0.3, 0.5, 0.8 and 1 (nonfractionated value) are shown in Fig. 23. In the figure, the aggregates having $^{235}U/^{238}U$ = 0.004 to 0.005 indicate that there was no chemical fractionation between U and Pb, and their $^{207}Pb/^{206}Pb$ apparent ages are from 2.01 ± 0.24 to 2.30 ±

0.18 Ga (metallic aggregates 1-1, 1-2, 10-1, 13-1 and 13-2 in Table 9), which roughly correspond to the depositional age of the uraninite at Oklo dated 2.05 Ga. The $^{207}Pb/^{206}Pb$ ratio of one analytical spot with $^{235}U/^{238}U = 0.00497$ (metallic aggregate 5-1 in Table 9) is higher than the calculated value, and its $^{207}Pb/^{206}Pb$ apparent age is 2.41 ± 0.08 Ga. As shown in Table 9, metallic aggregate 5 (5-1 and 5-2) exhibits depletion as well as enrichment of $^{235}U/^{238}U$, which demonstrates heterogeneous distributions of $^{235}U/^{238}U$ and radiogenic $^{207}Pb/^{206}Pb$ on a microscale. Therefore, it is difficult to demonstrate an accurate relationship between Pb and U isotopic compositions using the data from metallic aggregate 5 (5-1 and 5-2). On the other hand, chemical fractionation between U and Pb in the aggregates having $^{235}U/^{238}U > 0.007$ was observed. In Fig. 23, the data point having the highest $^{235}U/^{238}U$ (0.01466) is plotted in the area of f = 0.3–0.4. This result demonstrates that the $^{207}Pb/^{206}Pb$ present in the aggregate that underwent the most severe chemical fractionation was derived from the mixing of two components, one being the nonfractionated U-Pb (30%–40%) and the other being the fractionated U-Pb (60%–70%).

4.5.3 Effects of leaching on metallic aggregates

The differences in redox conditions strongly affect the dissolution rates of Mo, Tc, Ru, Rh and Pd in metallic aggregates (e.g., Forsyth, 1996; Cui et al., 2001, 2004). Leaching experiments on Mo-Ru-Tc-Pd-Rh-Te alloy particles extracted from spent fuel have demonstrated similar rates of leaching for ^{99}Tc and ^{100}Mo (1.5 ppb/day), which are three orders of magnitudes higher than those for Ru, Rh and Pd. Moreover, the rate of leaching of the epsilon phase under an oxidizing condition is ~100 times that under a reducing condition.

4.5.3.1 Mo

The chemical compositions of the epsilon phase in spent nuclear fuel indicate that fissiogenic Mo has the highest abundance of 40 wt.% among fissiogenic Mo, Tc, Ru, Rh and Pd (e.g., Cui et al., 2004). However, inclusion of Mo in the metallic aggregates found in RZs has never been reported (Gauthier-Lafaye et al., 1996; Hidaka et al., 1999). Since Mo has a high fission yield, large amounts of fissiogenic Mo are expected to have been produced in the RZs and incorporated into the metallic aggregates during the reactor criticality. In this study, however, EPMA revealed a Mo concentration under the limit of detection (hundreds of parts per million) in the aggregates. The low concentration of Mo in the aggregates found at the Oklo site is probably due to the partial leaching of Mo from the metallic aggregates under reducing conditions (Cui et al., 2001, 2004). According to Hidaka et al. (1999), the metallic aggregates in SD37-S2/CD formed during reactor operation. Therefore, the length of time over which Mo leached from the aggregates might be about two billion years. A calculation of the leached amounts of Mo during the aforesaid period of two billion years using a leaching rate of 1.5 ppb/day shows the total leached amounts exceed the total Mo content in the epsilon phase (about 40 wt.%). This result implies that Mo in the aggregates should have leached out entirely during the previously mentioned two billion years even under a reducing condition. However, the presence of some Mo has been identified in SHRIMP analyses in this study. The difference between expected and measured values of the concentrations of Mo suggests the leaching of fissiogenic Mo out of the aggregates.

4.5.3.2 Tc

Under changing redox conditions, two factors probably affect the chemical fractionation between Tc and Ru: (1) the incorporating ratios of Tc and Ru during formation of metallic aggregates, and (2) the rates of leaching of Tc and Ru during and after formation. Taking into account the half-life of 2.1×10^5 years for ^{99}Tc, the fractionation between Tc and Ru must have occurred over a period of $\sim 2.1 \times 10^5$ years. In such a relatively long period of time, the ^{99}Ru/^{101}Ru ratios should be strongly affected by the leaching behavior of ^{99}Tc. As shown in section 3.2.4, the rate of leaching of Tc is 10^3–10^4 times that of Ru even under a reducing condition, and is about 1.5 ppb/day. Considering the length of time of $\sim 2.1 \times 10^5$ years over which ^{99}Tc leached, the total amount of leached ^{99}Tc is estimated as $\sim 1.2 \times 10^5$ ppm under a reducing condition. The lowest ^{99}Ru/^{101}Ru ratio observed in this study is 0.324 ± 0.001, which indicates that the total amount of leached ^{99}Tc was the highest in all metallic aggregates. Assuming that the rate of leaching of ^{99}Tc under an oxidizing condition is ~100 times that under a reducing condition, the ^{99}Ru/^{101}Ru ratios of the aggregates decrease to 0.324.

4.5.4 Formation processes of metallic aggregates

Summarizing the results and discussions in this study, the formation processes of the metallic aggregates at SD37-S2/CD in RZ13 can be described as follows (Fig. 25). (i) The fissiogenic Mo, Tc, Ru, Rh, Pd and Te formed fine particles (less than a few microns in size) during the criticality and were gathered at the grain boundaries of 2.05 Ga-old UO_2 matrix. At the same time, the hydrothermal fluid including As, S, Te, Bi, Sb, Ni and Cu started to circulate in and around the RZ, which altered and dissolved the

original fissiogenic PGE particles and UO_2 matrix. Through interaction between the fissiogenic PGE particles and hydrothermal fluid, the metallic aggregates (a few tens of microns to 100 μm in size) formed having two main end-members where the fissiogenic Ru bonded to Cu while Rh and Pd formed complicated phases with As, S, Te, Bi, Sb and Ni. In addition, the 2.05-Ga fine uraninite grains including U, Pu, Zr and radiogenic Pb might have been derived from the alteration of UO_2 matrix and incorporated in the aggregates. (ii) During the criticality, there were oxidizing and reducing conditions due to the radiolysis of water inside the metallic aggregates. In the oxidizing regions, U, Mo and Tc might have leached from the aggregates, which led to the chemical fractionations between U and Pu, U and Pb, and Tc and Ru in the aggregates. (iii) Subsequently, the second hydrothermal fluid was derived from intrusion of the dolerite dyke 0.86 Ga ago at the Oklo site. Since this thermal event is considered to have mobilized a large amount of Pb and U, the radiogenic Pb accumulated in the UO_2 matrix could dissolve in the fluid and produce the Pb-rich hydrothermal fluid. Such Pb-rich fluid has been considered to lead to the precipitations of galena in the UO_2 matrix and metallic aggregates and to form the PbS-rich metallic aggregates observed in previous works. However, the absence of PbS in the aggregates studied in this work suggests that the aggregates were not affected by the Pb-rich fluids. Therefore, the degrees of interaction between the hydrothermal fluid and metallic aggregates could be different in the local area of SD37-S2/CD in RZ 13 during intrusion of the dolerite dyke.

4.5 Conclusions

The chemical compositions of the metallic aggregates investigated in this study

are quite different from those for aggregates reported previously. In the absence of any discernible correlation between Pb and S and in the existence of a positive correlation between U and Pb in the aggregates, the source of Pb in the aggregates is considered to be RZ uraninite and not galena. Although the $^{235}U/^{238}U$ isotopic ratios observed in the RZ are generally depleted, the $^{235}U/^{238}U$ isotopic ratios of the aggregates show enrichment as well as depletion. The variable $^{235}U/^{238}U$ ratio suggests that the aggregates were affected by the radiolysis of water, and there was large chemical fractionation between U and Pu in RZ 13 during criticality. The Pb isotopic ratios demonstrate that most of the Pb components in metallic aggregates were formed by radiogenic Pb derived from RZ uraninite. The deviation of the $^{207}Pb/^{206}Pb$ isotopic ratio from the expected value suggests the occurrence of radiogenic Pb and U in an incomplete chemical fractionation during the criticality. The isotopic data of the aggregates indicate that Zr and Mo isotopic compositions of metallic aggregates can be explained by the mixing of fissiogenic and nonfissiogenic components. However, the $^{99}Ru/^{101}Ru$ isotopic ratios of the aggregates show enrichment as well as depletion in each aggregate, which cannot be explained by the mixing of fissiogenic and nonfissiogenic components. The variations of $^{99}Ru/^{101}Ru$ ratios are considered to be a result of the incorporation of Tc and Ru in various ratios after chemical fractionation between Tc and Ru during reactor operation. The large variations in the $^{99}Ru/^{101}Ru$ and $^{235}U/^{238}U$ ratios probably suggest that the aggregates formed under various redox conditions owing to the radiolysis of water.

CHAPTER 5

Summary

The isotopic analyses of REE in U- and REE-bearing minerals and zircon from the clay and black shale layers above the Bangombé natural reactor, Gabon, were performed using a SHRIMP to investigate the migration and retardation processes of fission products released from the reactor. In addition, to understand the long-term geological behavior of fissiogenic Zr, Mo, Tc and Ru, the metallic aggregates taken from RZ 13 in Oklo uranium deposit were also investigated using SHRIMP. *In-situ* Pb and U isotopic data of specific minerals and metallic aggregate were useful to reveal the geological events and timing that led to the migration of fissiogenic nuclides in and around the natural reactors.

Several kinds of U and REE bearing secondary minerals, such as coffinite and françoisite, were found in the clays and black shales above the Bangombé RZ. Isotopic data of $^{140}Ce/^{142}Ce$, $^{145}Nd/^{146}Nd$ and $^{149}Sm/^{147}Sm$ clearly reveal that these minerals resulted from mixing between fissiogenic component from the reactor zones and non-fissiogenic component from native minerals by recent geologic alteration. REE isotopic data also show that most of fissiogenic LREE were effectively trapped in the clays and not distributed into the black shales over the clays, which reveals that the clays play an important role in preventing fission products from spreading.

The zircon crystals in the clays heterogeneously contain a U-rich region (up to 28.3 wt%) with normal $^{235}U/^{238}U$ ratios (=0.00725) and significant amounts of fissiogenic REE, which indicate U and REE derived from RZ occurred chemical

fractionation and depleted U from the RZ was partially dissolved and mixed with a large amount of normal U from non reactor materials. Although crystalline zircon is generally considered to be durable under most geochemical conditions, highly damaged zircon in this study showed significant migration of U and REE. Zircons taken from the clays and black shales near the boundary of clay and black shale layers indicated that large amounts of the fissiogenic Nd, Sm and Eu derived from the reactor are incorporated into the zircon grains in clay layer but did not migrate into the zircons in black shale layer. On the other hand, Ce isotopic ratios of the zircons in the clay and black shale layers have larger variations than those of the other REE. This is clear evidence of a large chemical fractionation between Ce and other REE above the reactor caused by the chemical characteristics of the altered zircon under the oxidizing atmosphere and severe weathering condition.

For accurate chronological interpretation for migration of fissiogenic components, the reliability of the calibration technique was checked using the zircon grains found above the Bangombé RZ. The conventional U–Pb calibration technique for *in-situ* SHRIMP zircon analysis does not always function especially for high-U zircon (>2500 ppm U), as Williams and Hergt (2000) pointed. However, the bias of $^{206}Pb/^{238}U$ with U content over 2500 ppm could not be identified in this study. Therefore, the conventional calibration technique was applied to only the zircons with U < 2500 ppm. High-U zircon grains having U over 2500 ppm were determined by the analytical combination of U/Pb elemental ratios by EPMA and Pb isotopic composition by SHRIMP. The U–Pb data of zircons taken from the clay layer above the Bangombé RZ provide chronological information on the igneous activity associated with the basement rock formation at 2.8 Ga and geochemical evidence of the incomplete

mixing of independent Pb and U sources originated from 2.05-Ga old uraninite under the recent severe weathering.

A few tens of μm-sized metallic aggregates consisting mainly of Ru, Rh, Pd, Te, Pb, As, Sb, S and Bi were found in the acid residue of uraninite from RZ 13 in Oklo uranium deposit. The chemical compositions of the metallic aggregates investigated in this study are quite different from the aggregates reported previously. In the absence of any discernible correlation between Pb and S and the existence of a positive correlation among U, As and Pb in the aggregates, the source of Pb in the aggregates is considered to be RZ uraninite and not galena. On the other hand, Ru and Pd show different geochemical behaviors in the aggregate; Ru might form an alloy with Cu, while Pd form a sulfide with As and S. Although the $^{235}U/^{238}U$ isotopic ratios observed in the reactor zone are generally depleted, the $^{235}U/^{238}U$ isotopic ratios of the aggregates show enrichment as well as depletion. The variable $^{235}U/^{238}U$ ratio suggests that the aggregates were affected by radiolysis of water and a large chemical fractionation occurred between U and Pu in the RZ 13 during criticality. The Pb isotopic ratios demonstrate that most of the Pb components in metallic aggregates were formed by radiogenic Pb derived from RZ uraninite. The deviation of $^{207}Pb/^{206}Pb$ isotopic ratio from the expected value, suggests the occurrence of radiogenic Pb and U in an incomplete chemical fractionation caused by radiolysis of water during the criticality. The isotopic data of the aggregates indicate that Zr and Mo isotopic compositions of metallic aggregates can be explained by a mixing between fissiogenic and non-fissiogenic components. However, the $^{99}Ru/^{101}Ru$ isotopic ratios of the aggregates show enrichment as well as depletion in each aggregate, which cannot be explained by a mixing between fissiogenic and non-fissiogenic components. The

variations of $^{99}Ru/^{101}Ru$ ratios are considered to be a result of incorporation of Tc and Ru in various ratios after the occurrence of a chemical fractionation between Tc and Ru during reactor operation. The large variations of the $^{99}Ru/^{101}Ru$ and $^{235}U/^{238}U$ ratios probably suggest that the aggregates were formed under various redox conditions due to radiolysis of water.

REFERENCES

Blanc, P.-L. (1996) Oklo-Natural analogue for a radioactive waste repository (phase 1). Volume 1. Acquirement of the project. In *European Commission*, Nuclear science and technology series VI, pp. 123 ISBN-92-827-7448-1.

Bodu R., Bouzigues H., Morin N. and Pfiffelmann J. P. (1972) Sur l'existence d'anomalies isotopiques rencontrées dans l'uranium du Gabon. *C. R. Acad. Sci. Paris* **275**, 1731–1734.

Bonhomme M. Gauthier-Lafaye F. and Weber F. (1982) An example of Lower Proterozoic sediments: the Francevillian in Gabon. *Precambrian Res.* **18**, 87–102.

Bros R., Gauthier-Lafaye F., Holliger P. and Still P. (1993) Occurrence of naturally enriched ^{235}U: Implications for plutonium behavior in natural environments. *Geochim. Cosmochim. Acta* **57**, 1351–1356.

Bros R., Carpena J., Sere V. and Beltritti A. (1996) Occurrence of Pu and fissiogenic rare earth elements in hydrothermal apatites from the fossil natural nuclear reactor 16 of Oklo (Gabon). *Radiochim. Acta* **74**, 277–282.

Bros R., Hidaka H., Kamei G. and Toshihiko T. (2003) Mobilization and mechanisms of retardation in the Oklo natural reactor zone 2 (Gabon)—inferences from U, REE, Zr, Mo and Se isotopes. *App. Geochem.* **18**, 1807–1824.

Buck E. C., Hanson B. D. and McNamara B. K. (2004) The geochemical behavior of Tc, Np and Pu in spent nuclear fuel in an oxidizing environment. In *Energy, Waste, and the Environment: a Geochemical Perspective* (eds. R. Gieré, P. Stille). The Geological Society of London Special Publication 236, pp. 65–88.

Butera K. M., Williams I. S., Blevin P. L. and Simpson C. J. (2001) Zircon U–Pb dating of Early Palaeozoic monzonitic intrusive from the Goonumbla area, New South Wales. *Australian Journal of Earth Sciences,* **48**, 457–1464.

Chen F., Burns P. C. and Ewing R. C. (2000) Near-field behavior of ^{99}Tc during the oxidative alteration of spent nuclear fuel. *J. Nucl. Mat.***278**, 225–232.

Compston W., Williams I. S. and Meyer, C. (1984) U–Pb geochronology of zircons from lunar breccia 73217 using a sensitive high mass-resolution ion microprobe. *Journal of Geophysical Research,* **89**, B525–1B534.

Cowan G. A. and Alder H. H. (1976) The variability of the natural abundance of ^{235}U. *Geochim Cosmochim Acta* **40**, 1477–1490.

Cui D., Eriksen T. and Eklund U. B. (2001) On metal aggregates in spent fuel, synthesis and leaching of Mo-Ru-Pd-Rh Alloy. In *Scientific Basis for Nuclear Waste Management XXIV.* (eds. K. P. Hart and G. R. Lumpkin) *Mater. Res. Soc. Symp. Proc.* **663**, 427.

Cui D., Low J., Sjöstedt C. J. and Spahiu K. (2004) On Mo-Ru-Tc-Pd-Rh-Te alloy particles extracted from spent fuel and their leaching behavior under Ar and H_2 atmosphere. *Radiochim. Acta* **92**, 551-555.

Curtis D. (1986) Geochemical controls on 99-Tc transport and retention. *Chem. Geol.* **55**, 227–231.

De Laeter J. R. and Hidaka H. (2007) The role of mass spectrometry to study the Oklo–Bangombé natural reactors. *Mass Spectrometry Reviews,* **26**, 683–712.

Devillers C., Ruffenach J., Menes J., Lucas M., Hagemann R. and Nief G. (1975) Age de la mineralisation de l'uranium et date de la reaction nuclaire. Int Symp of the Oklo Phenomenon. IAEA, SM-204/26:293–302.

Dymkov Y., Holliger P., Pagel M., Gorshukov A. and Artyukhina A. (1997) Characterisation of a La–Ce–Sr–aluminous hydroxyl phosphate in nuclear zone 13 in the Oklo uranium deposit (Gabon). *Miner. Deposita* **32**, 617–620.

England T. R. and Rider B. F. (1988) Chainy for MITO-TAL, Los Alamos National Laboratory Report, LA-UR-88-1696.

Evins L. Z., Jensen K. A. and Ewing R. C. (2005) Uraninite recrystallization and Pb loss in the Oklo and Bangombé natural fission reactors, Gabon. *Geochim. Cosmochim. Acta* **69**, 1589–1606.

Forsyth R. S. (1996) Spent fuel corrosion : study of the Tc-99 source term for the BWR and PWR reference fuel. SKB arbetsrepport 94–07.

Fréjacques C., Blain C., Devillers C., Hagemann R. and Ruffenach J.-C. (1975) Conclusions tirés de l'etude de la migration des produits de fission. Le phénomène d'Oklo, IAEA, pp. 509–524.

Gancarz A. J. (1978) U-Pb age ($2.05x10^9$ years) of the Oklo uranium deposit. In *Natural Fission Reactors*, International Atomic Energy Agency, Vienna, Austria. pp. 513–520.

Gauthier-Lafaye, F. (1986) Les gisements d'uranium du Gabon et les réacteurs d'Oklo. Modèle métallogénique de gites à fortes teneurs du Protérozoique inférieur. Mémoire Sciences Géologiques 78–206.

Gauthier-Lafaye F. and Weber F. (1981) Les concentration uranifères du Francevillien

du Gabon: leur association avec des gîtes à hydrocarbures fossiles du Protérozoïque inférieur. *C.R. Acad. Sci. Paris* **292**, 69–74.

Gauthier-Lafaye, F. and Weber, F. (1989) The Francevillian (Lower Proterozoic) uranium ore deposits of Gabon. *Econ. Geol.* **84**, 2267– 2285.

Gauthier-Lafaye F., Holliger P. and Blanc P.-L. (1996) Natural fission reactors in the Franceville basin, Gabon: a review of the conditions and results of a ''critical event'' in a geologic system. *Geochim. Cosmochim. Acta* **60**, 4831–4852.

Gauthier-Lafaye F., Stille P. and Bros, R. (2004) Special cases of natural analogues: the Gabon and Cigar lake U ore deposits. *In Energy, Waste, and the Environment: A Geochemical Perspectives (eds. R. Gieré and P. Stille).* Geological Society, London, Special Publication, **236**, pp. 123–134.

Hidaka H. and Masuda A. (1988) Nuclide analyses of rare earth elements of the Oklo uranium ore samples: a new method to estimate the neutron fluence. *Earth Planet. Sci. Lett.* **88**, 330–336.

Hidaka H. and Holliger P. (1998) Geochemical and neutronic characteristics of the natural fossil fission reactors at Oklo and Bangombé Gabon. *Geochim. Cosmochim. Acta* **62**, 89–108.

Hidaka H. and Gauthier-Lafaye F. (2000) Redistribution of fissiogenic and non-fissiogenic REE, Th and U in and around natural fission reactors at Oklo and Bangombé, Gabon. *Geochim. Cosmochim. Acta* **64**, 2093–2108.

Hidaka H., Shinotsuka K. and Holliger P. (1993) Geochemical behaviour of ^{99}Tc in the Oklo natural fission reactors. *Radiochim. Acta* **63**, 19–22.

Hidaka H., Sugiyama T., Ebihara M. and Holliger P. (1994) Isotopic evidence for the

retention of ^{90}Sr inferred from excess ^{90}Zr in the Oklo natural fission reactors: Implication for geochemical behaviour of fissiogenic Rb, Sr, Cs and Ba. *Earth Plan. Sci. Lett.* **122**, 173–182.

Hidaka H., Holliger P. and Gauthier-Lafaye F. (1999) Tc/Ru fractionation in the Oklo and Bangombé natural fission reactors, Gabon. *Chem. Geol.* **155**, 323–333.

Hidaka H., Janeczek J., Skomurski F. N., Ewing R. and Gauthier-Lafaye F. (2005) Geochemical fixation of rare earth elements into secondary minerals in sandstones beneath a natural fission reactor at Bangombé, Gabon. *Geochim. Cosmochim. Acta* **69**, 685–694.

Holland H. D. (1994) Paleoproterozoic atmospheric change. In: Bengtson, S. (Ed.), *Early Life on Earth, Nobel Symposium*, vol. 84. Columbia University Press, New York, pp. 237–244.

Holliger, P. (1988) Ages U–Pb définis in-situ sur oxides d'uranium à l'analyseur ionique: méthodologie et consé- quences géochimiques. *C.R. Acad. Sci. Paris* **307**, 367–373.

Holliger P. (1992) Les nouvelles zones de réaction d'Oklo: datation U-Pb et caractérisation in-situ des produits de fission à l'analyseeur ionique. *Programme "Oklo-Analogues Naturels," Note technique CEN Grenoble DEM n°01/92.* Commissariat à l'Energie Atomique.

Holliger P. (1993) SIMS studies on the Oklo natural fission reactors. *Proc. SIMS IX Conference, Yokohama*, (Invited lecture) pp. 8–12.

Holliger P. (1995) Terme source: caractérisation isotopique, paramètres nucléaires et modélisation. *Repport CCE n°F112W-CT91-0071. Programme Oklo-Analogues*

Naturels.

Holliger P. and Devillers C. (1981) Contribution a l'etude de la temperature dans les reacteurs fossils d'Oklo par la mesure du rapport isotopique du lutetium. *Earth. Planet. Sci. Lett.* **52**, 76–84.

Horie K., Hidaka H. and Gauthier-Lafaye F. (2004) Isotopic evidence for trapped fissiogenic REE and nucleogenic Pu in apatite and Pb evolution at the Oklo natural reactor. *Geochim. Cosmochim. Acta* **68**, 115–125.

Hoskin P. W. O. and Schaltegger U. (2003) The composition of zircon and igneous and metamorphic petrogenesis. In: Hanchar, J.M., Hoskin, P.W.O. (Eds.), *Reviews in Mineralogy and Geochemistry. Miner. Soc. Am.*, vol. 53, pp. 27–62.

Jaffey A. H., Flynn K. F., Glendenin L. E., Bentley W. C., and Essling A.-M. (1971) Precision measurements of half-lives and specific activities of ^{235}U and ^{238}U. *Phvs. Rev.* **4**. 1889–1906.

Janeczek J. (1999) Mineralogy and geochemistry of natural fission reactors in Gabon. *Rev. Mineral.* **38,** 321–392.

Janeczek J. and Ewing R. (1996a) Phosphatian coffinite with rareearth elements and Ce-rich françoisite from sandstone beneath a natural fission reactor at Bangombé, Gabon. *Mineral. Mag.* **60**, 665–669.

Janeczek J. and Ewing R. (1996b) Florencite–(La) with fissiogenic REEs from a natural fission reactor at Bangombé, Gabon. *Am. Mineral.* **81**, 1263–1269.

Jensen K. A. and Ewing R. C. (2001) The Okélobondo natural fission reactor, southeast

Gabon: geology, mineralogy and retardation of nuclear reaction products. *Geol. Soc. Am. Bull.* **113/1**, 32–62.

Kleykamp K. (1985) The chemical state of fission products in oxide fuels. *J. Nucl. Mat.* **131**, 221–246.

Kuroda P. K. (1956) On the nuclear physical stability of the uranium minerals. *J. Chem. Phys.* **25**, 781–782.

Lancelot J. R., Vitrac A. and Allegre C. J. (1975) The Oklo Natural Reactor Age and evolution studies by U-Pb and Rb-Sr systematics. *Earth Planet Sci Lett* **25**, 189–196.

Lee J. and Whitehouse M. J. (2007) Onset of mid-crustal extensional flow in southern Tibet: Evidence from U/Pb zircon ages. *Geol.* **35**, 45–48.

Loss R. D., Rosman K. J. R., DeLaeter J. R., Curtis D. B., Benjamin T. M., Gancarz A. J., Maeck W. J. and Delmore J. E. (1989) Fission-product retentivity in peripheral rocks at the Oklo natural fission reactors. Gabon. *Chem. Geol.* **76**, 71–84.

McLaren A. C., FitzGerald J. D. and Williams I. S. (1994) The microstructure of zircon and its influence on the age determination from Pb/U isotopic ratios measured by ion microprobe. *Geochim. Cosmochim. Acta* **58**, 933–1005.

Mathieu R., Zetterström L., Cuney M., Gauthier-Lafaye F. and Hidaka H. (2001) Alteration of monazite and zircon and lead migration as geochemical tracers of fluid paleocirculations around the Oklo–Okléobondo and Bamgombé natural nuclear reaction zones (Franceville basin, Gabon). *Chem. Geol.* **171**, 147–171.

Meshik A. P., Hohenberg C. M. and Pravdiviseva O. V. (2004) Record of cycling operation of the natural nuclear reactor in the Oklo/Okelobondo area in Gabon.

Phys. Rev. Lett. **93**, 182302-1–182302-4.

Minster J. F. and Ricard L. P. (1981) The isotopic composition of zirconium. *Int. J. Mass Spectrom. Ion Phys.* **37**, 259–272.

Nagy B., Gauthier-Lafaye F., Holliger P., Mossman D., Leventhal J. and Rigali M. (1993) Role of organic matter in the proterozoic Oklo natural fission reactors, Gabon, Africa. *Geology* **21**, 655–658.

Naudet, R. (1991) Oklo: des réacteurs nucléaires fossiles. Paris: Collection du Commissariat à l'Energie Atomique. p. 695.

Naudet R. and Renson C. (1975) Résultats des analyses systématiques de teneurs isotopiques de l'uranium. Proc. *The Oklo Phenomenon,* pp. 265–288. IAEA.

Neuilly M., Bussac J., Fréjacques C., Nief G., Vendryes G. and Yvon J. (1972) Sur l'existence dans un passé reculé d'une réaction en chaine naturelle de fission, dans le gisement d'uranium d'Oklo (Gabon). *C. R. Acad. Sci. Paris* **275,** 1847–1849.

Nilsson S. and Jonsson M. (2008) On the catalytic effects of UO_2(s) and Pd(s) on the reaction between H_2O_2 and H_2 in aqueous solution. *J. Nucl. Mater.* **372,** 160–163.

Openshaw R., Pagel M. and Poty B. (1978) Phases fluids contemporaines de la diagenesé des grés, des mouvements tectoniques et du fonctionment des réacteurs nucléaires d'Oklo (Gabon). In Natural Fission Reactors. IAEA-TC-119/9. IAEA, Vienna, p 267-296.

Paces J. B. and Miller J. D. (1993) Precise U–Pb age of Duluth Complex and related mafic intrusions, northeastern Minnesota: geochronological insights into

physical, petrogenic, paleomagnetic and tectonomagmatic processes associated with the 1.1 Ga midcontinent rift system. *J. Geophys. Res.* **98**, 13997–14013.

Poths H., Schmitt-Strecker S. and Begemann F. (1987) On the isotopic composition of ruthenium in the Allende and Leoville carbonaceous chondrites. *Geochim. Cosmochim. Acta* **51**, 1143–1149.

Ruffenach, J. C. (1978) Etude des migrations de l'uranium et des terres rares sur une carotte de sondage et application à la détermination de la date des réactions nicléaires. In: Proceedings of The Natural Fission Reactors, IAEA Symposium Proceedings, Vienna, pp. 441–471.

Ruffenach, J. C. (1979) Les réacteurs nucléaires naturels d'Oklo. Paramètres neutroniques, date et durée de fonctionnement, migrations de l'uranium et des produits de fission. Thesis Sci., Université Paris VII, p. 351.

Ruffenach J. C., Hagemann R. and Roth E. (1980) Isotopic abundances measurements: A key to understanding the Oklo Phenomenon Zeit. Naturforsch 35a, 171–179.

Stacey J.S. and Kramers J.D. (1975) Approximation of terrestrial lead isotopic evolution by a two-stage model. *Earth Plan. Sci. Lett.,* **26**, 207–221.

Stille P., Gauthier-Lafaye F., Jensen K. A., Salah S., Bracke G., Ewing R. C., Louvat D. and Million D. (2003) REE mobility in groundwater proximate to the natural fission reactor at Bangombé (Gabon). *Chem. Geol.* **198**, 289–304.

Thomas L. E. and Guenther R. J. (1989) Characterization of low-gass release LWR fuels by transmission electron microscopy. In *Scientific Basis for Nuclear Waste Management XII.* (eds. W. Lutze and R. C. Ewing). *Mater. Res. Soc. Symp. Proc.* **127,** 293.

Utsunomiya S. and Ewing R. C. (2006) The fate of the epsilon phase

(Mo-Ru-Pd-Tc-Rh) in the UO_2 of the Oklo natural fission reactors. *Radiochim. Acta* **94**, 749-753.

Utsunomiya S., Valley J. W., Cavosie A. J., Wilde S. A. and Ewing R. C. (2007) Radiation damage and alteration of zircon from a 3.3 Ga porphyritic granite from the Jack Hills, Western Australia. *Chem. Geol.* **236**, 92–111.

Weber F. and Bonhomme M. (1975) Donnes radiochronologiques nouvelles sur le Francevillien et son environnement. Int Symp of the Oklo Phenomenon. IAEA, SM-204/16:17–35.

Wetherill G. W. and Inghram M. G. (1953) Proc Conf Nucl Proc Geol Settings. National Research Council, Washington, DC, USA. pp 30–32.

Wieser M. E., DeLaeter J. R. and Varner M. D. (2007) Isotope fractionation studies of molybdenum. *Int. J. Mass Spectrom.* **265**, 40–48.

Williams I. S. and Hergt, J. M. (2000) U–Pb dating of Tasmanian dolerite: A cautionary tale of SHRIMP analysis of high-U zircon. In *Beyond 2000: New Frontiers in Isotope Geoscience* (eds. J. D. Woodhead, J. M. Hergt and W. P. Noble) Abstract and Proceedings, Lorne.

Zeck H. P. and Williams I. S. (2002) Inherited and magmatic zircon from Neogene Hoyazo cordierite dacite, SE Spain–Anatectic source rock provenance and magmatic evolution. *J. Petro.*, **43**, 1089–1104.

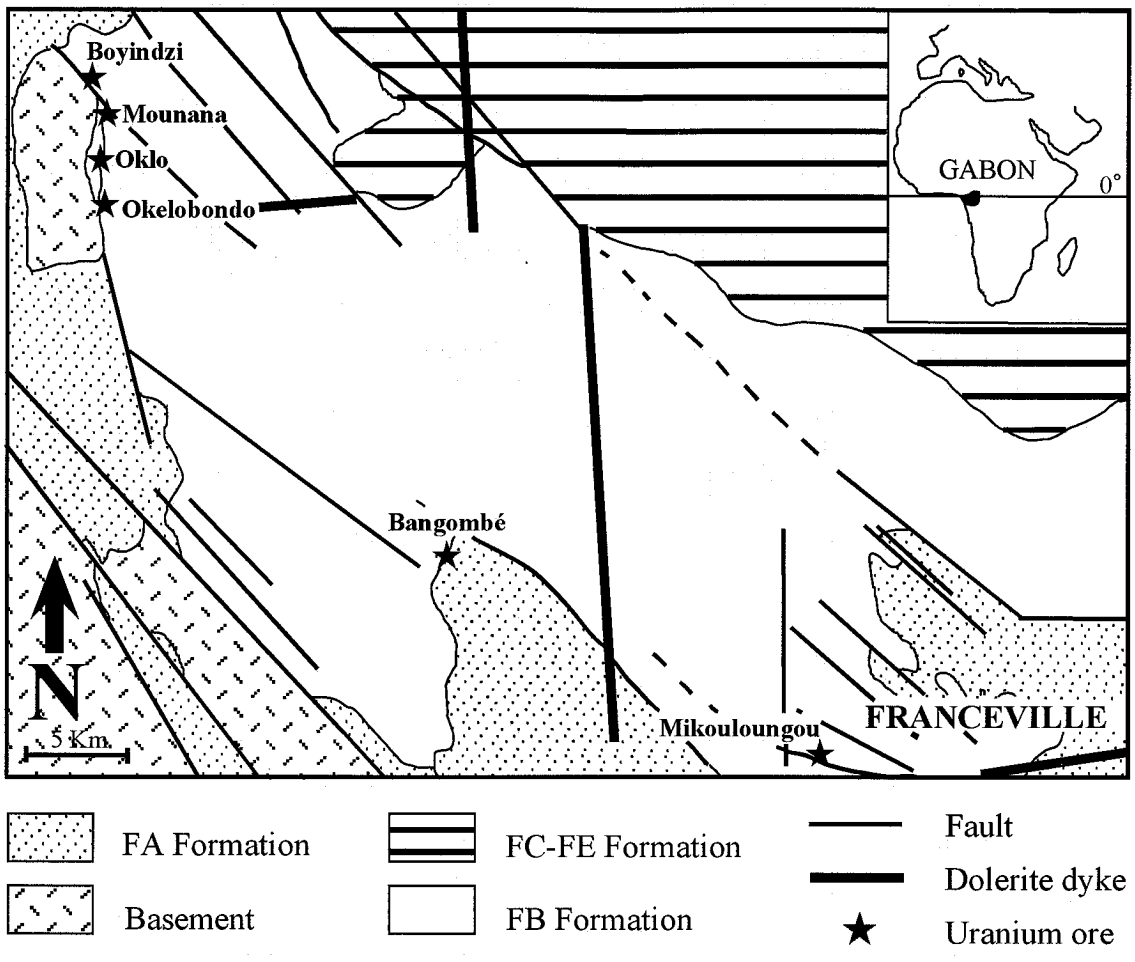

Fig. 1. Geological map of the Franceville basin.

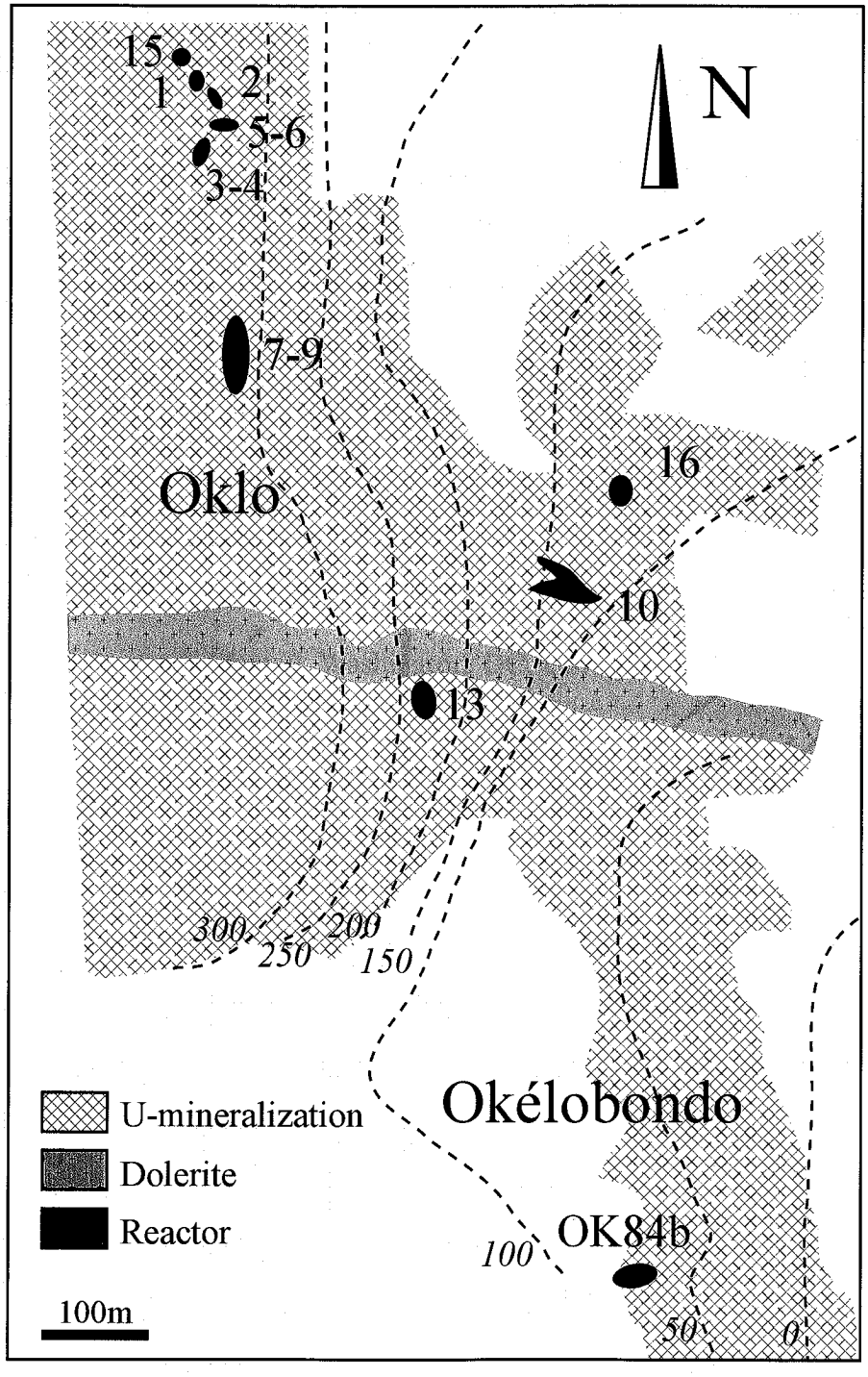

Fig. 2. The Location of Oklo reactor zones.

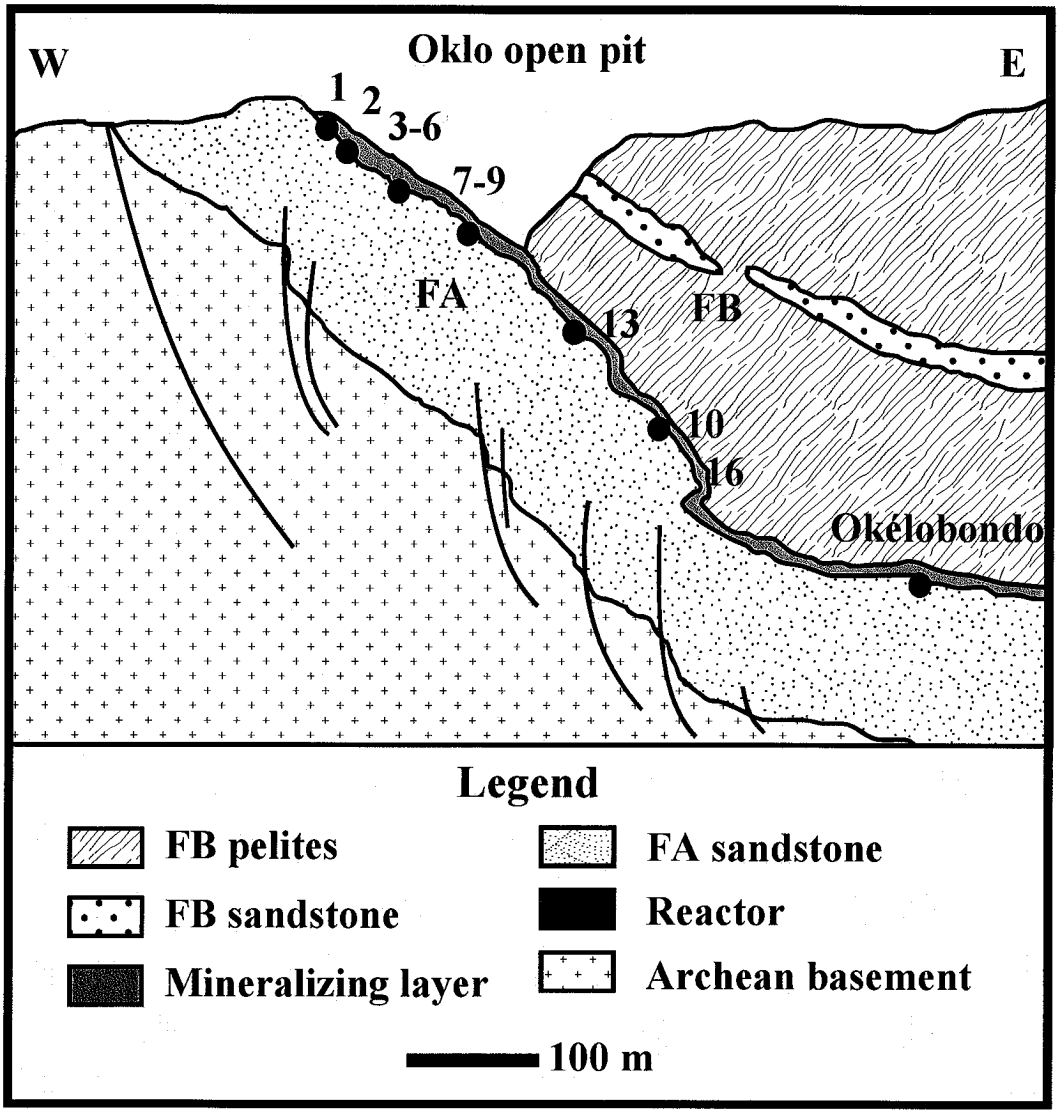

Fig. 3. Cross section of the deposit with the depth location of the reactor zones (modified after Gauthier-Lafaye et al., 1996).

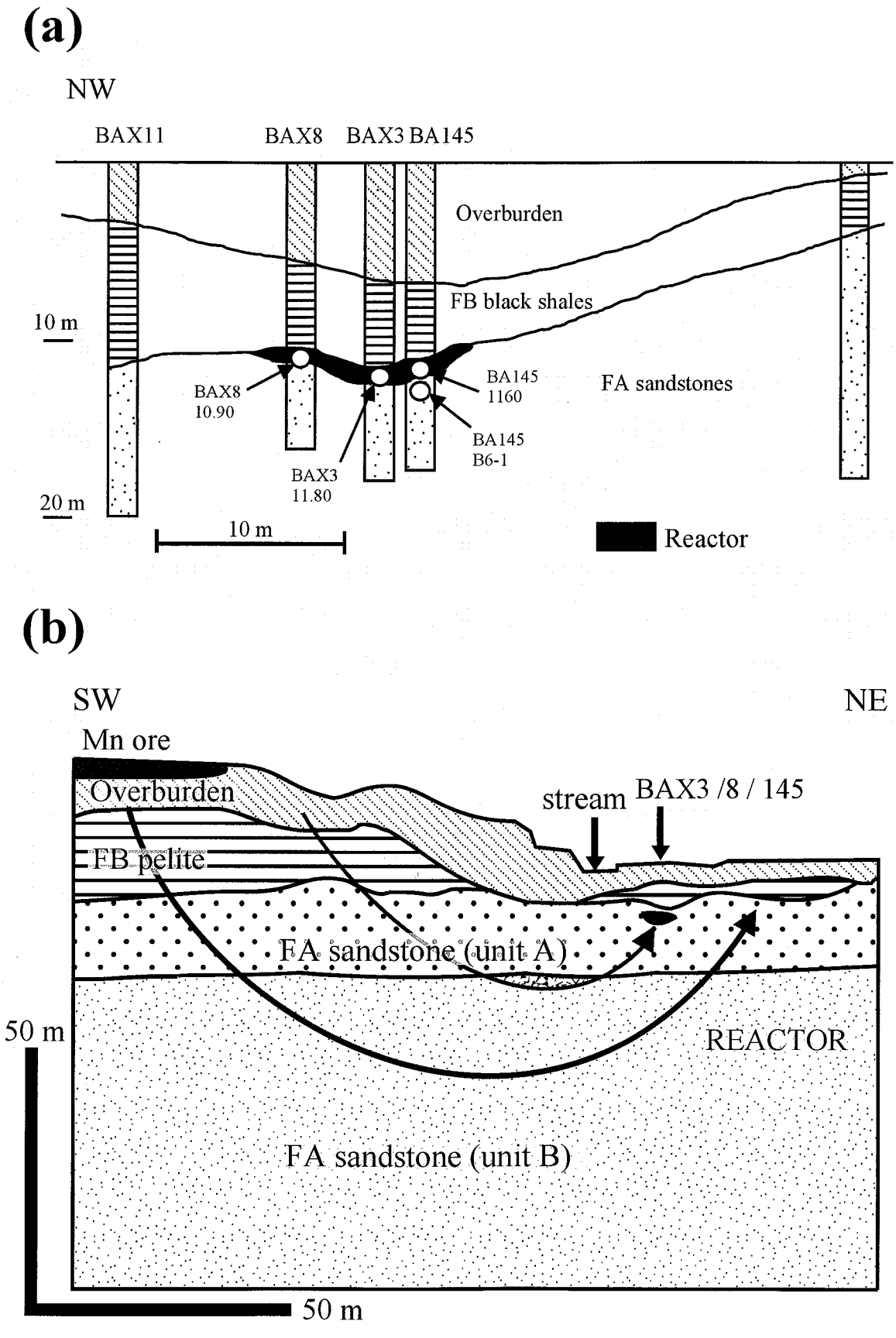

Fig. 4. (a) Location of the Bangombé RZ and the boreholes. Three boreholes, BA145, BAX3 and BAX8, intersect the RZ. (b) Lithology and groundwater flow paths in the Bangombé area (after Stille et al., 2003). The groundwater flow is indicated by arrows.

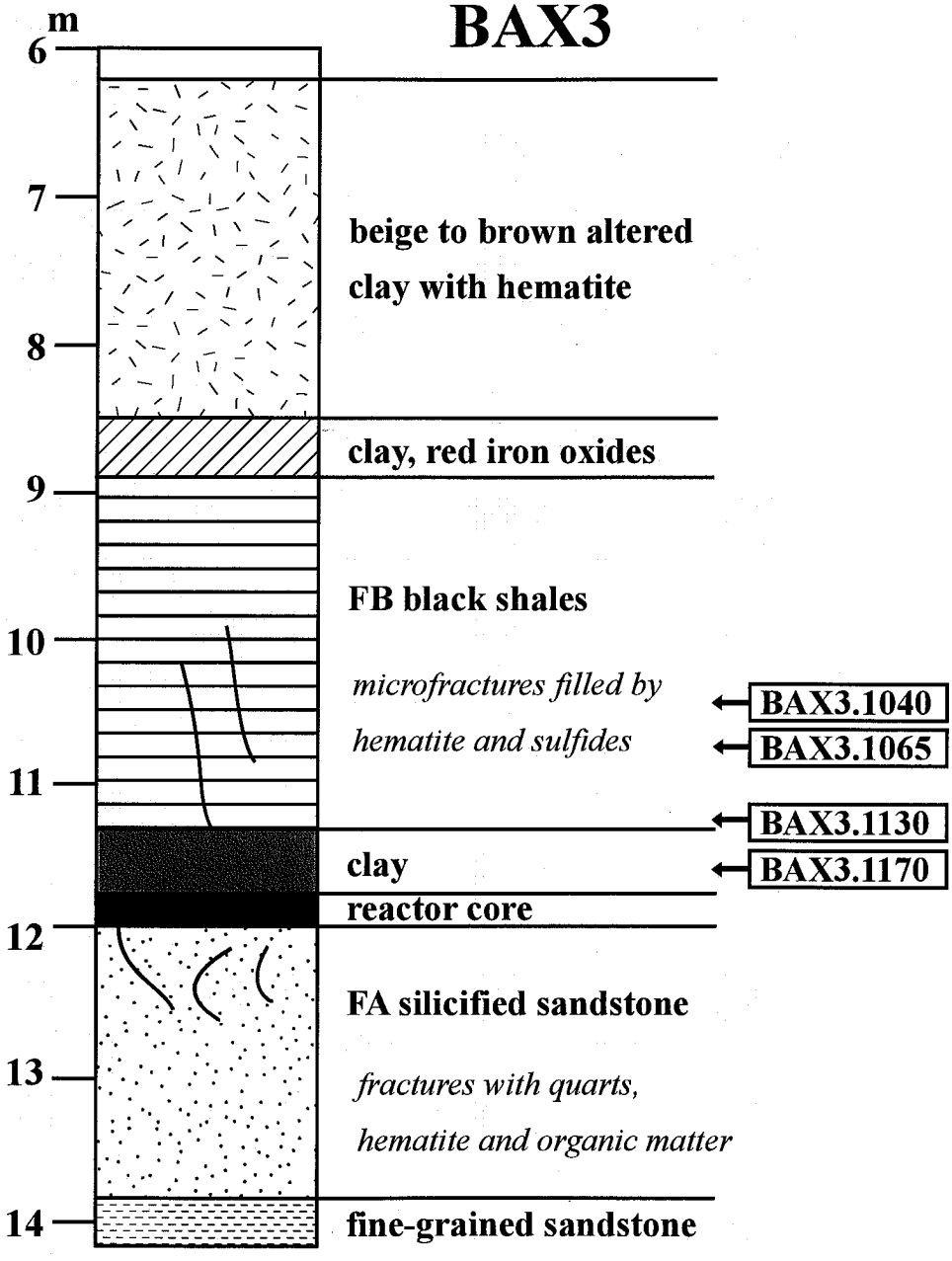

Fig. 5. Petrologic type of stratigraphic section of the BAX3 drill core and the locations of samples used in this study. BAX3.1170 is from the clay part. BAX3.1040 , 1065 and 1130 are from black shales.

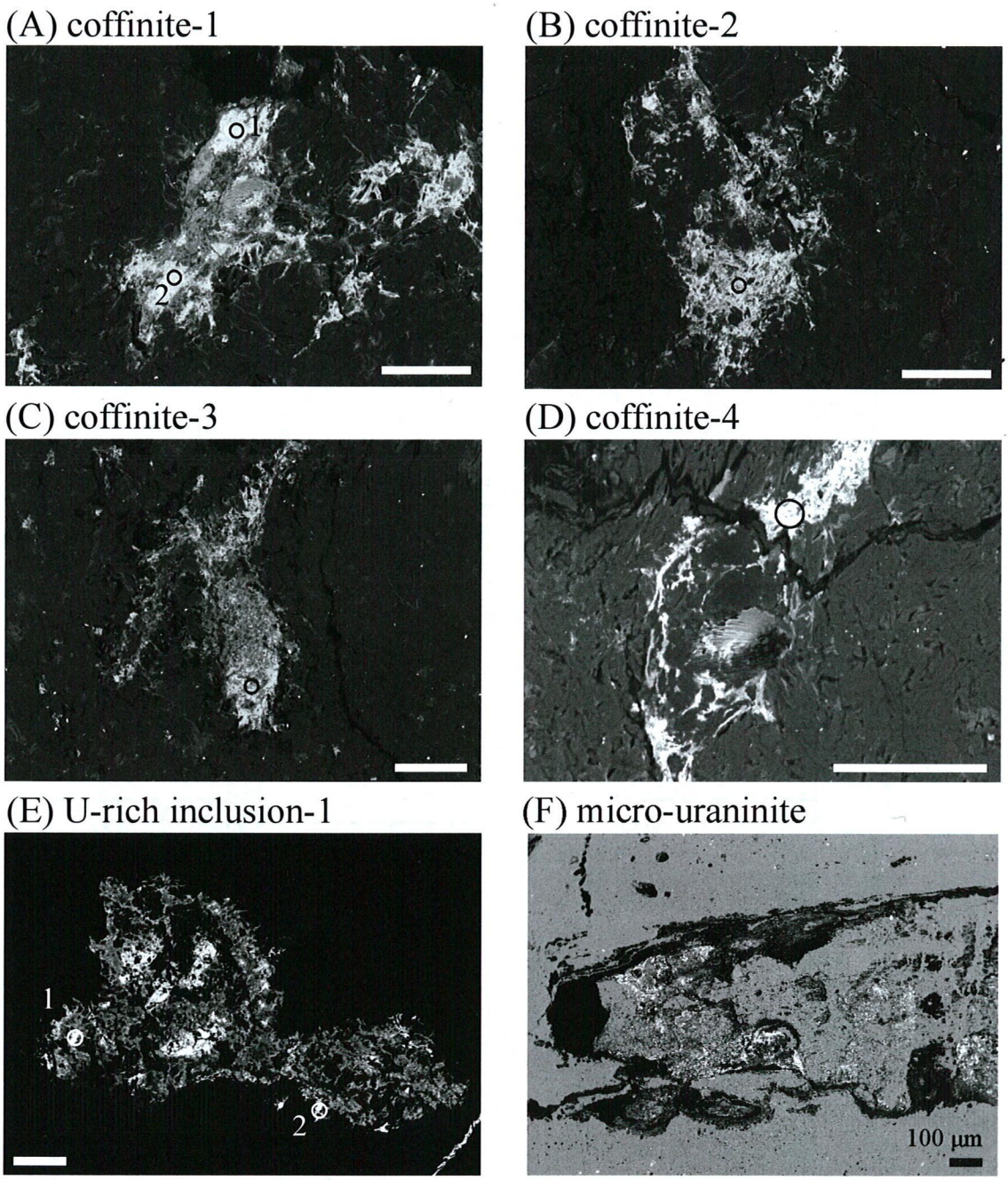

Fig. 6. BSE images of typical micro-minerals measured in this study. (A–C) Coffinite, (D) coffinite with a rim of a few micrometers of françoisite, (E) galena with U-rich inclusions, (F) micro-uraninite. The circles and the numbers in the photos reveal analytical spots. Individual scale bars in the photos are 50 μm.

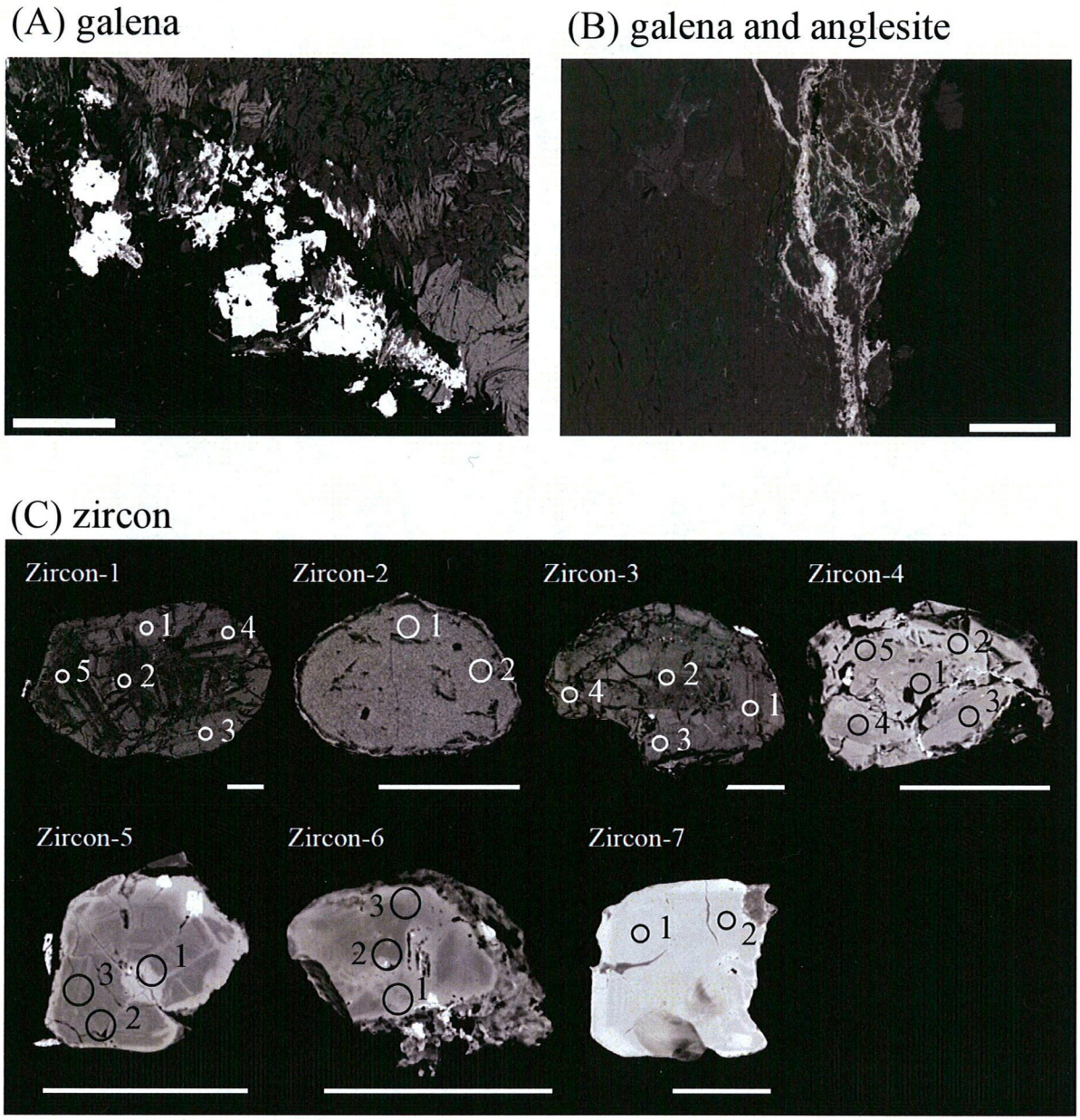

Fig. 7. BSE images of (A) galena, (B) galena (white) with a rim of a few micrometers of anglesite (gray) and (C) zircon crystals. The circles and numbers in the photos reveal analytical spots that correspond to the isotopic data. Individual scale bars in the photos are 50 μm.

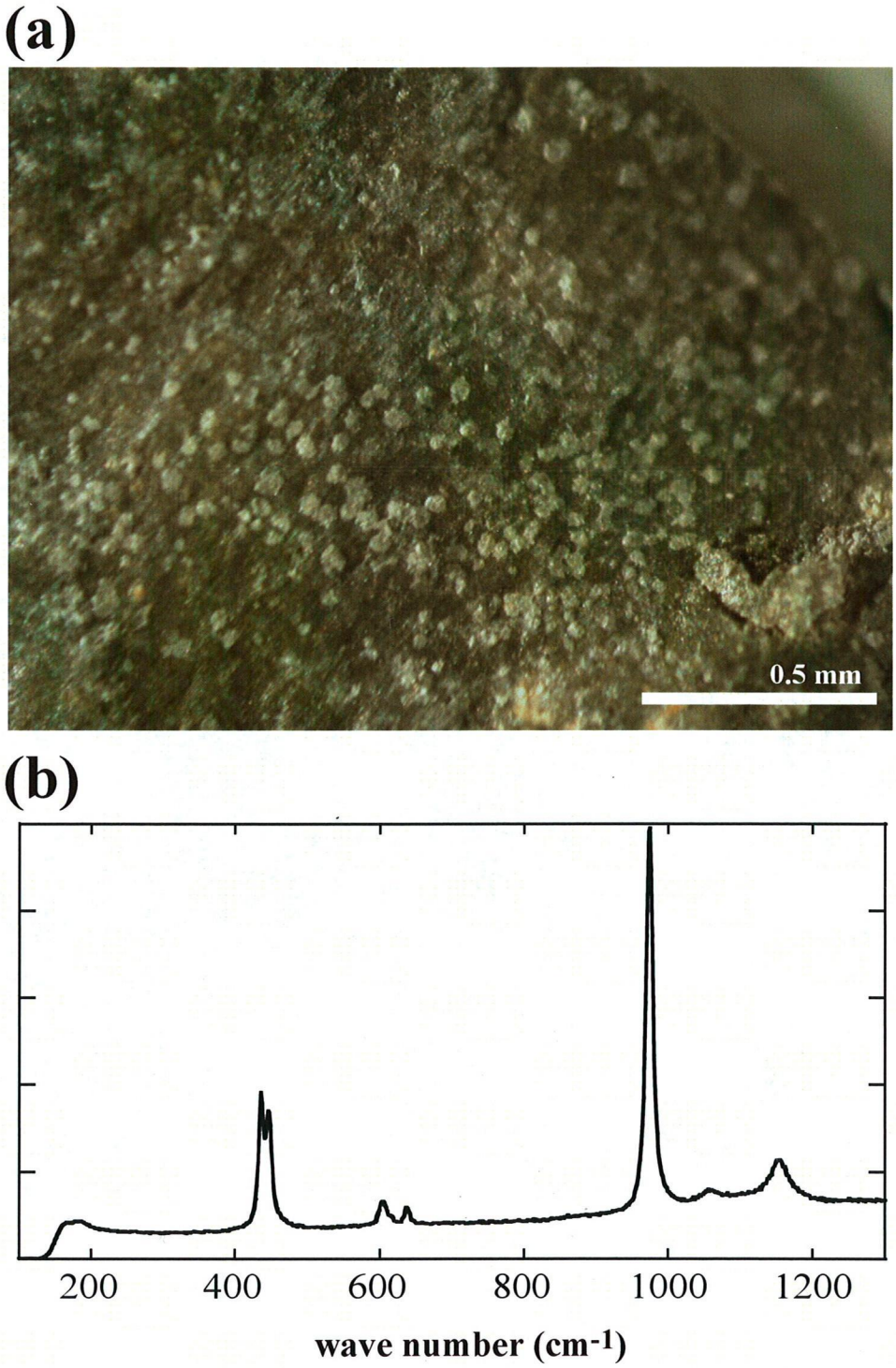

Fig. 8. Photo (a) and Raman spectum (b) of anglesite (white grain) on the surface of crack in the clay sample (BAX3.1170).

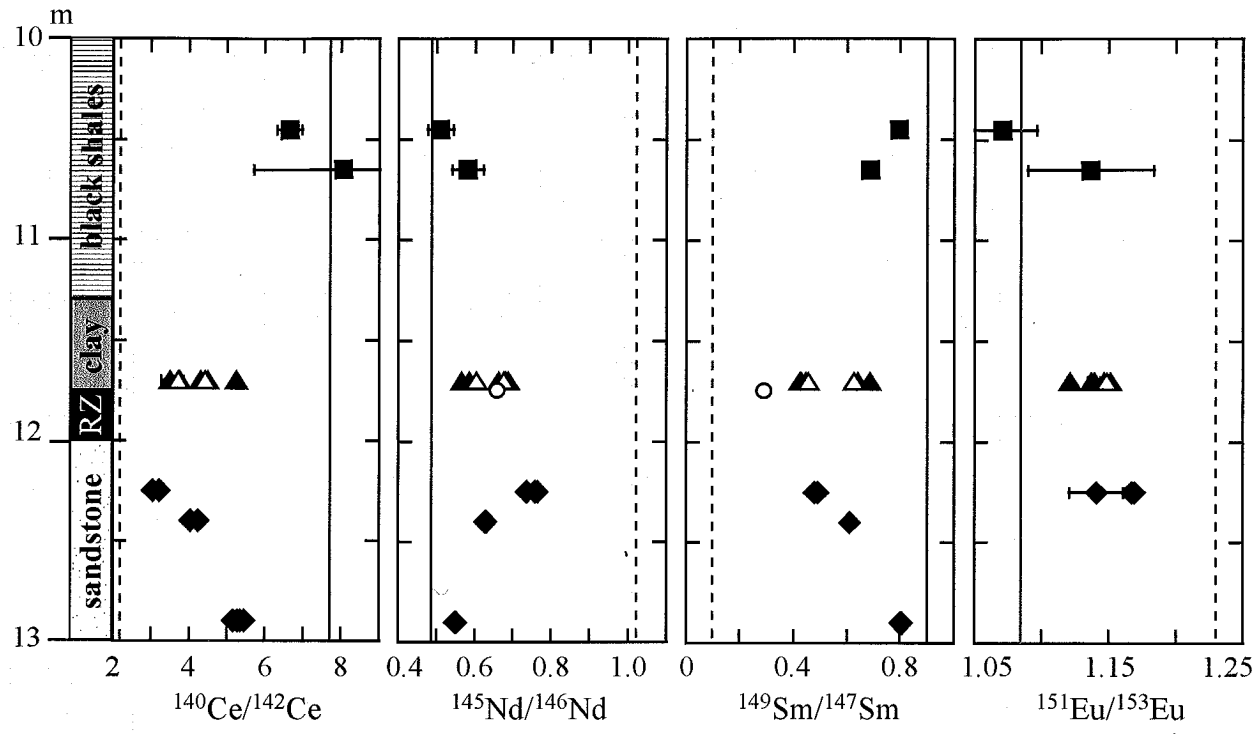

Fig. 9. Depth-dependent variations of $^{140}Ce/^{142}Ce$, $^{145}Nd/^{146}Nd$, $^{149}Sm/^{147}Sm$ and $^{153}Eu/^{151}Eu$ isotopic ratios of U- and REE-bearing minerals in the BAX3 drill core. The vertical axis indicates the depth from the surface in meters. The data points with solid squares (micro-uraninite in BAX3.1040 and 1065), solid triangles (coffinite in BAX3.1170), and open triangles (U-inclusion in BAX3.1170) are from this study. The data points with open squares (uraninite in BAX3.1180), open circle (florencite in BAX3.1175), and solid diamonds (U- and REE-bearing minerals in BAX3.1225, 1240 and 1290) are from previous works (Hidaka and Gauthier-Lafaye, 2000; Janeczek and Ewing, 1996b; Hidaka et al., 2005).

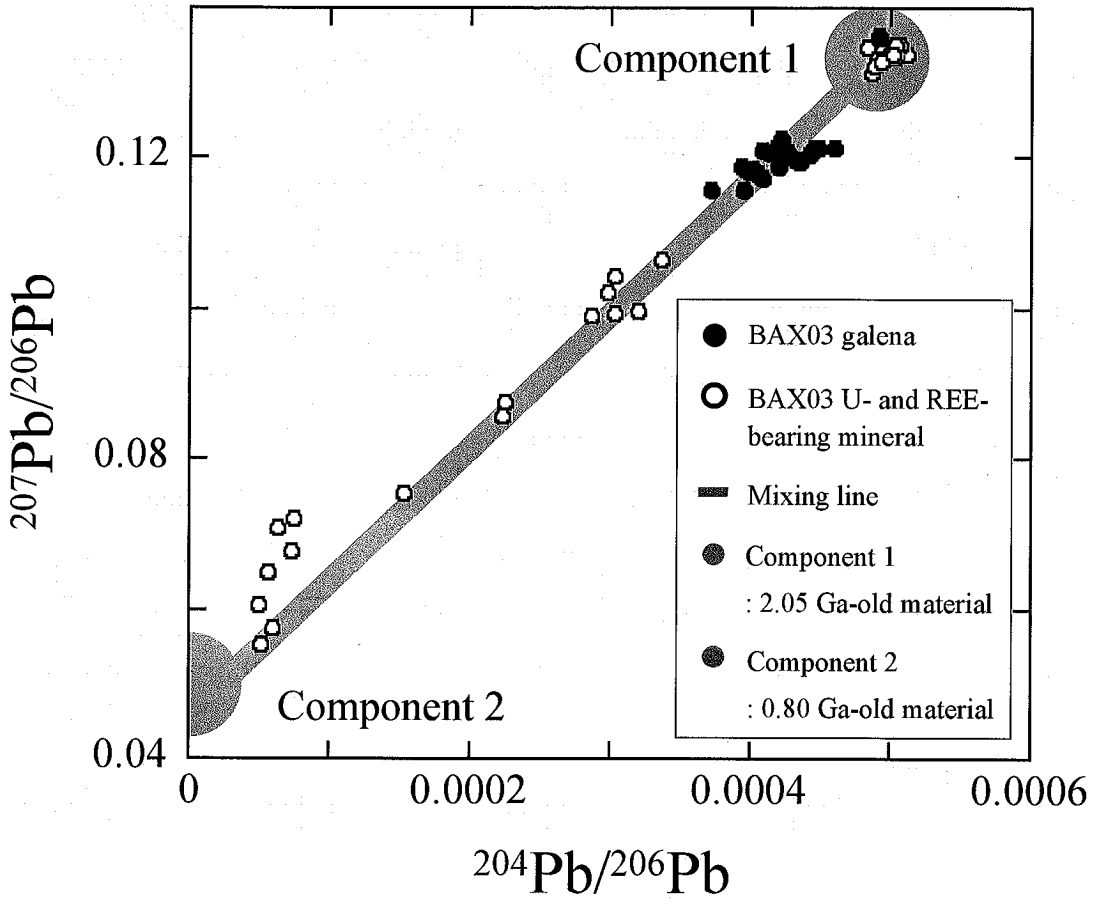

Fig. 10. $^{204}Pb/^{206}Pb$ vs. $^{207}Pb/^{206}Pb$ diagram of galena grains from the clay (BAX3.1160) above the Bangombé reactor. The data points with solid circles are from this study, and those with open circles are from U- and REE-bearing minerals in sandstone samples (BAX3.1215, 1225, 1240 and 1290) beneath the reactor by Hidaka et al. (2005).

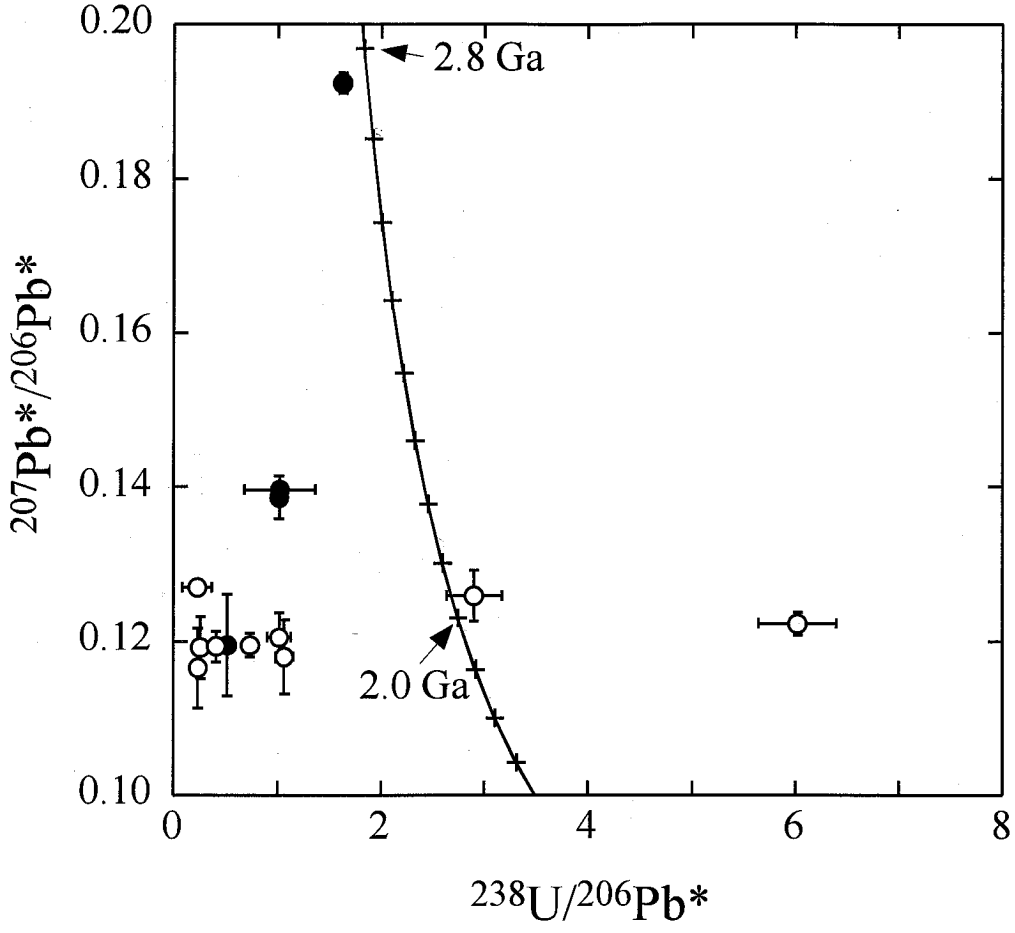

Fig. 11. Tera-Wasserburg U–Pb Concordia diagram of six zircon grains from the clay (BAX3.1160) above the Bangombe reactor. The data points with solid circles are from SHRIMP analyses, and those with open circles are from the combination of SHRIMP and EPMA analyses (see text).

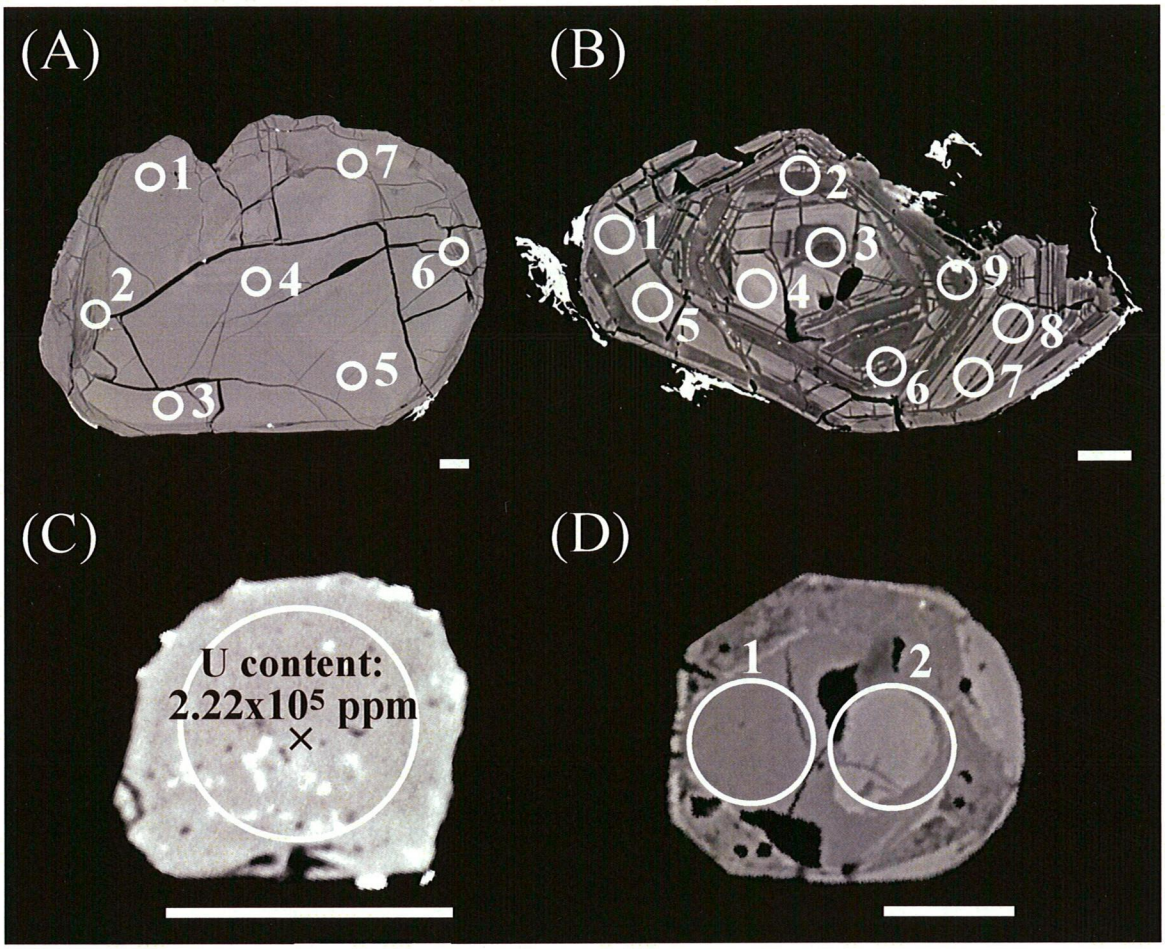

Fig. 12. BSE image of typical zircons found in this study. (A), (B) and (C) Zircon grains in BAX3.1170. (D) Zircon grains in BAX3.1130. The circles and the numbers in the photos reveal analytical spots. Scale bar in each photo is 10 μm.

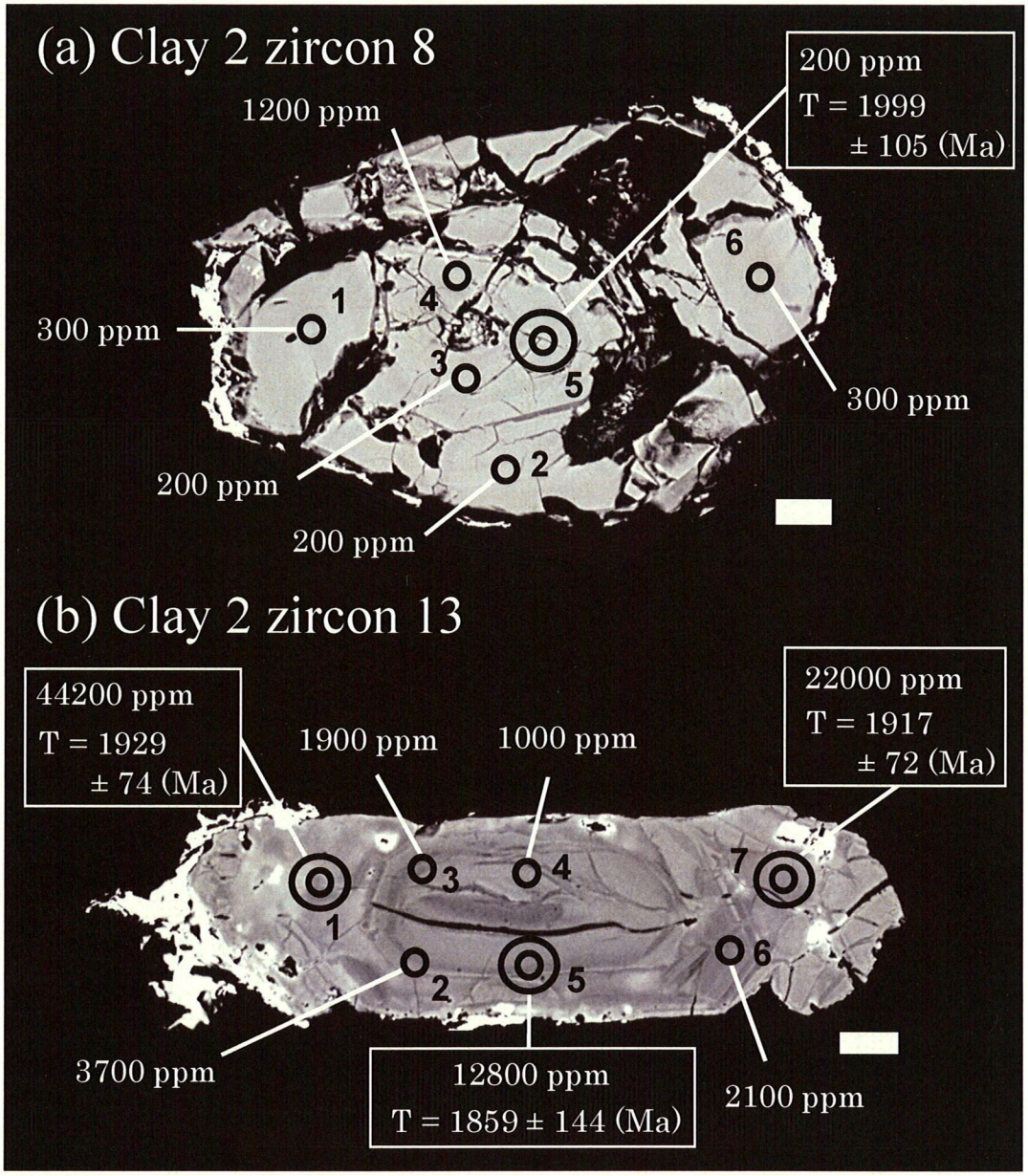

Fig. 13. BSE images of typical zircons having (a) low-U and (b) high-U contents in this study. The small circles (about 3 μm in diameter) and numbers in the photos reveal the analytical spots in EPMA analyses. U contents in each analytical spot determined from EPMA are also shown. Large circles (about 10 μm in diameter) indicate locations of SHRIMP analyses, numbers refer to data in Table 7. The corresponding $^{207}Pb/^{206}Pb$ apparent ages (T) are shown in each analytical spot of SHRIMP analysis. Individual scale bars in each grain are 10 μm.

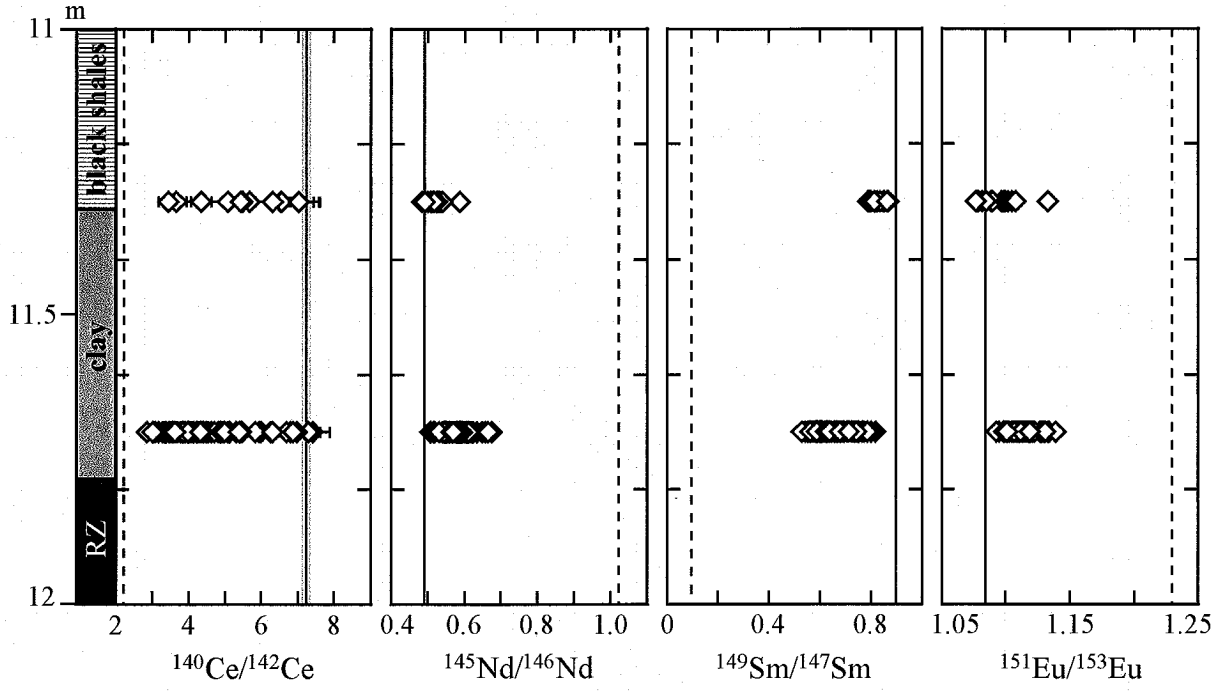

Fig. 14. Depth-dependent variations of $^{140}Ce/^{142}Ce$, $^{145}Nd/^{146}Nd$, $^{149}Sm/^{147}Sm$, and $^{153}Eu/^{151}Eu$ isotopic ratios of zircons in the BAX3 drill-core. The vertical axis shows depth from surface in m. The dotted lines (- - -) show the standard values (NIST610 standard glass) and the reactor values which are from Hidaka and Gauthier-Lafaye (2000).

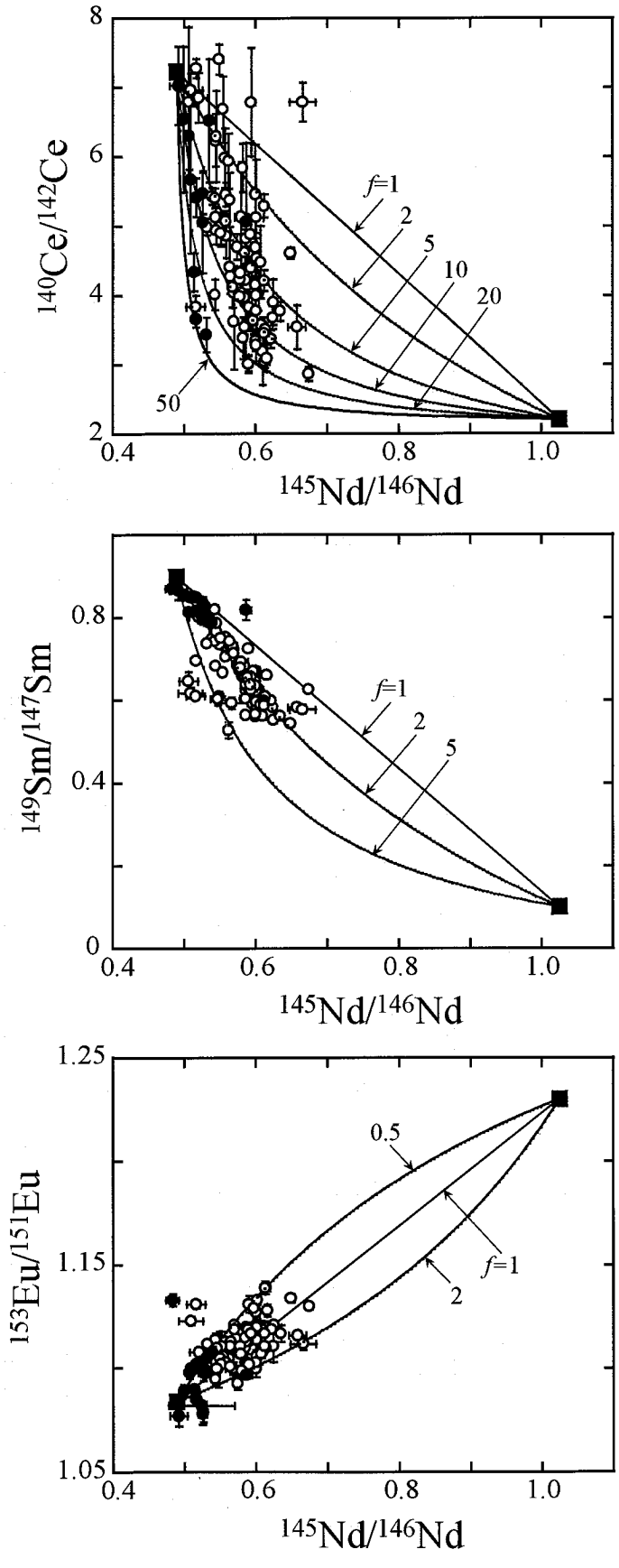

Fig. 15. Two-component mixing curves between non-fissiogenic (STD) and fissiogenic (reactor) materials. Isotopic ratios of STD and reactor in each diagram correspond to those of NIST610 standard glass and Bangombé reactor BAX3.1180 (Hidaka and Gauthier-Lafaye, 2000), respectively. ''f'' values show chemical differentiation factors of Ce, Sm and Eu relative to Nd. The closed circles show the samples of black shale layer and the open circles show those of clay layer.

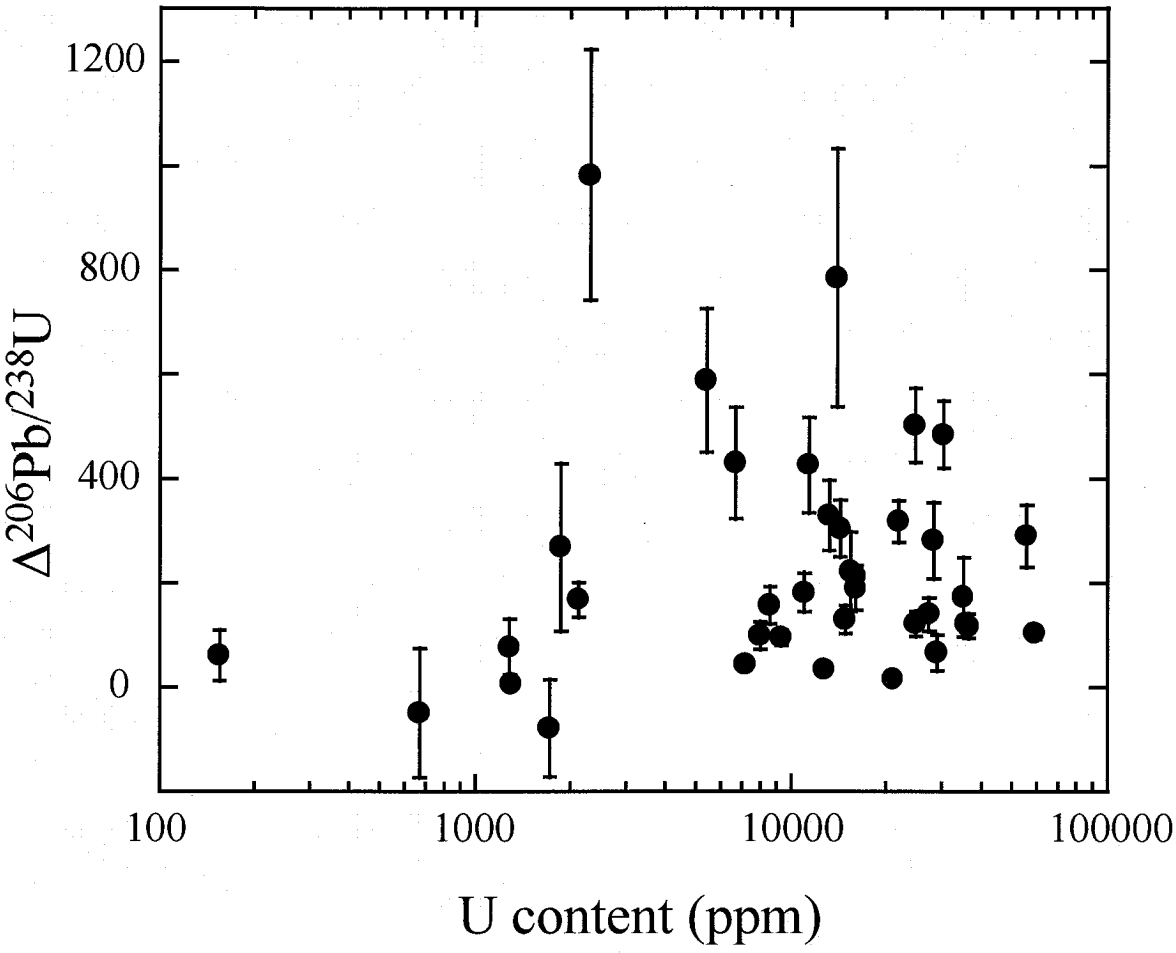

Fig. 16. Correlation plot between fractional difference ($\Delta^{206}Pb/238U$) in EPMA and SHRIMP analyses and U content. The fractional difference was defined as $\Delta^{206}Pb/^{238}U = \{(^{206}Pb/^{238}U)_{SHRIMP}/(^{206}Pb/^{238}U)_{EPMA} - 1\} \times 100$ (%).

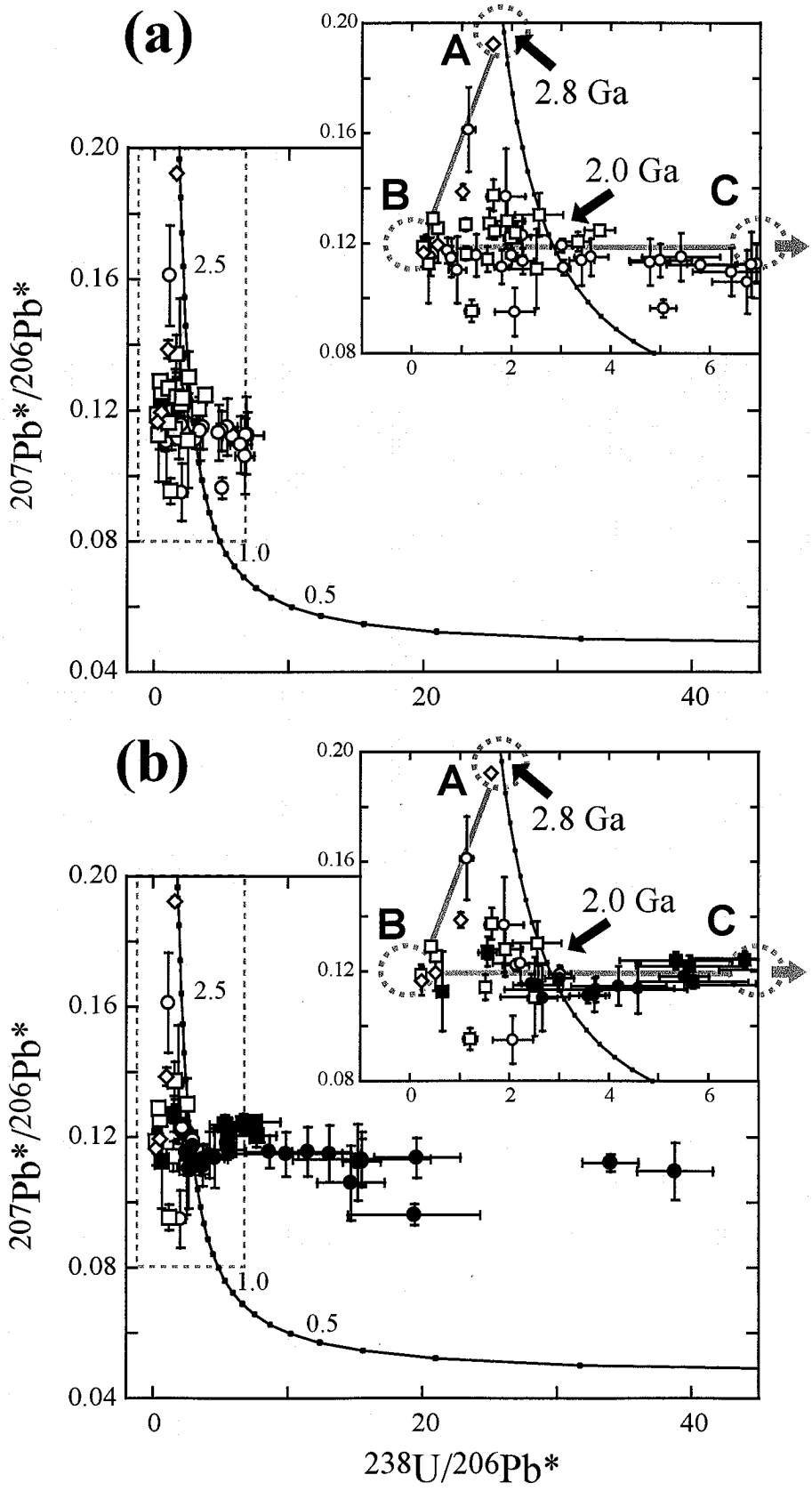

Fig. 17. Tera-Wasserburg U–Pb concordia diagram for zircon grains above the Bangombé natural reactor. (a) The diagram obtained by the conventional calibration technique in SHRIMP analysis. (b) The diagram obtained by the analytical combination of SHRIMP and EPMA analyses (see in the text). The data points with circles (clay layer) and squares (black shale layer) are from this study, and those with diamonds (clay layer) are data in Table 4. The open symbols are from SHRIMP analyses and solid symbols are from the combination of SHRIMP and EPMA analyses.

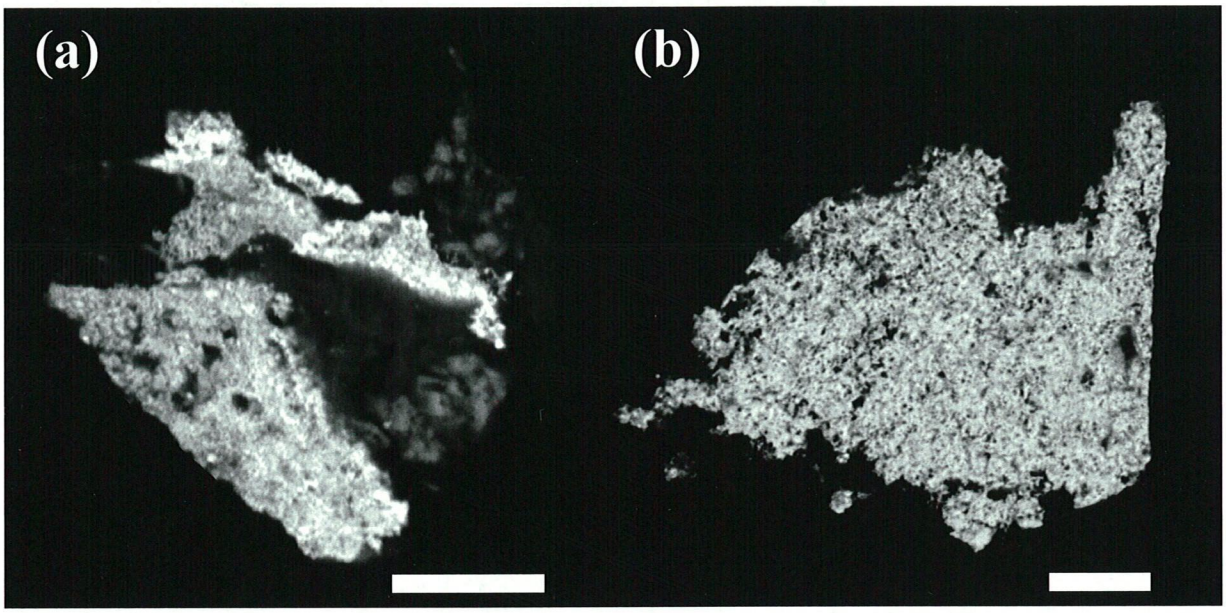

Fig. 18. Backscattered electron (BSE) image of typical metallic aggregates having micro-inclusions (a) and relatively homogeneous distribution (b) in this study. The scale bar is 10 μm.

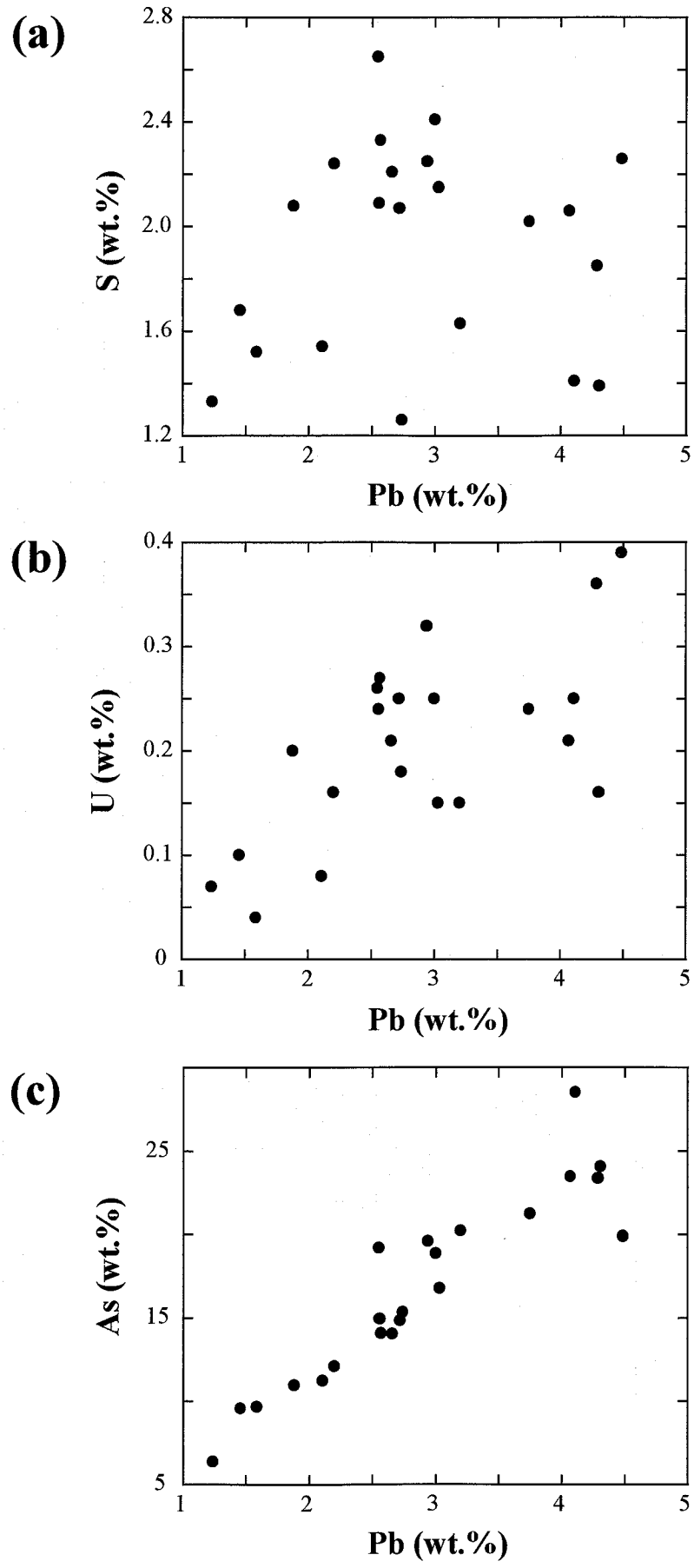

Fig. 19. Plots of Pb content vs. S content (a), Pb content vs. U content (b), and Pb content vs. As content (c) of the metallic aggregates analyzed in this study.

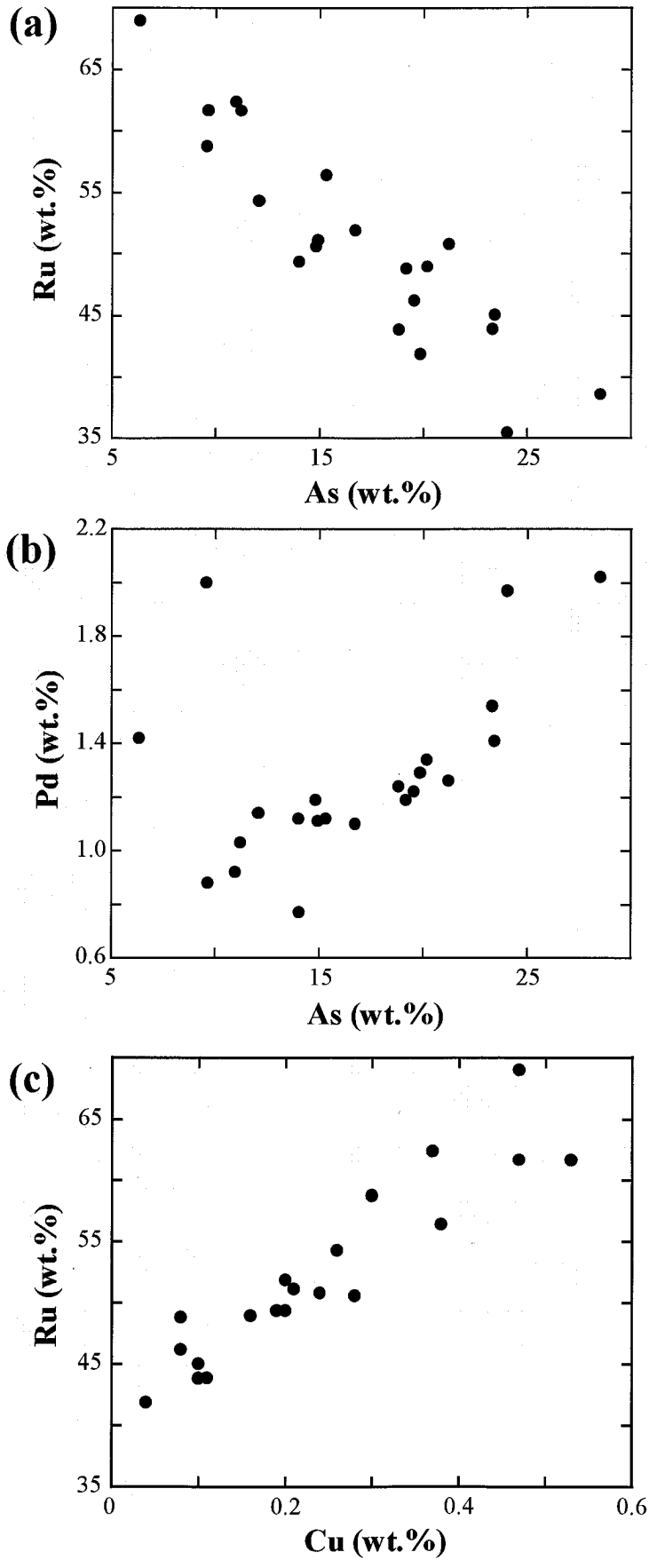

Fig. 20. Plots of As content vs. Ru content (a), As content vs. Pd content (b), and Cu content vs. Ru content (c) of the metallic aggregates analyzed in this study.

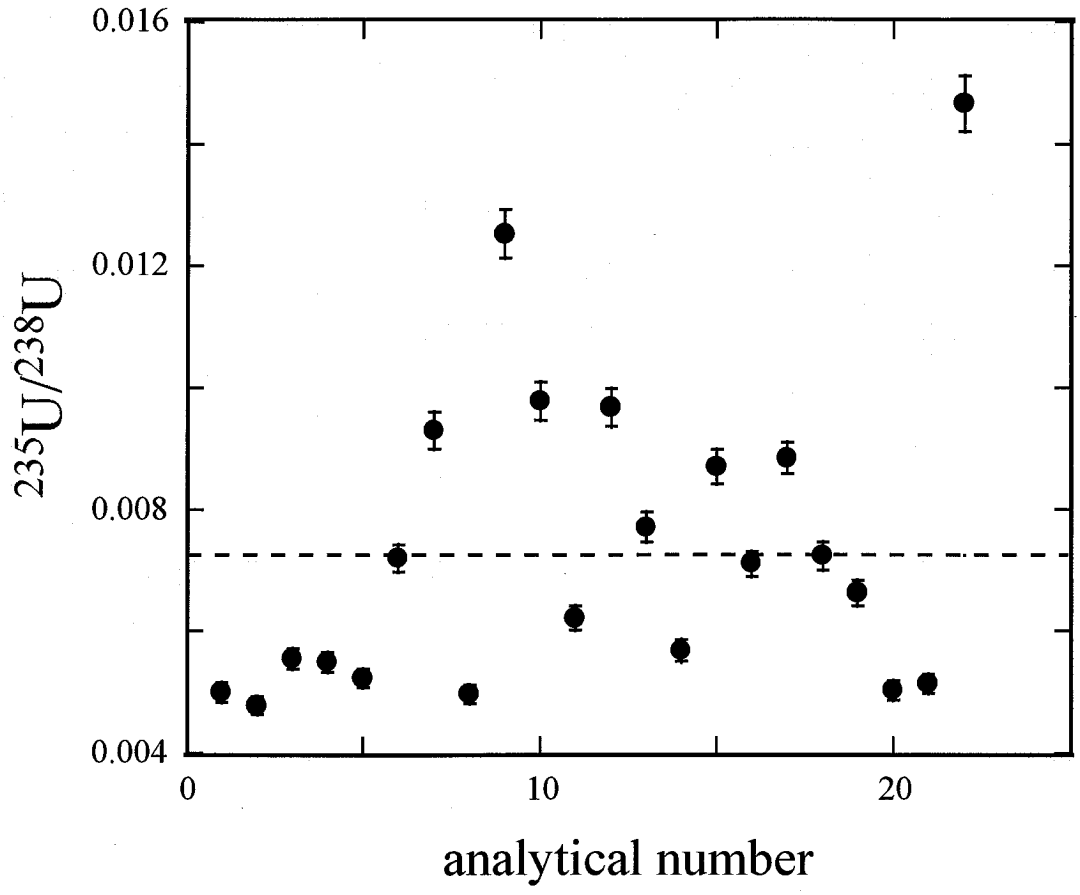

Fig. 21. Isotopic ratios of $^{235}U/^{238}U$ for the metallic aggregates analyzed in this study. The isotopic data are lined up in chronological order. The dotted line shows the terrestrial $^{235}U/^{238}U$ ratio obtained from standard zircon AS3 (0.00725±0.00004).

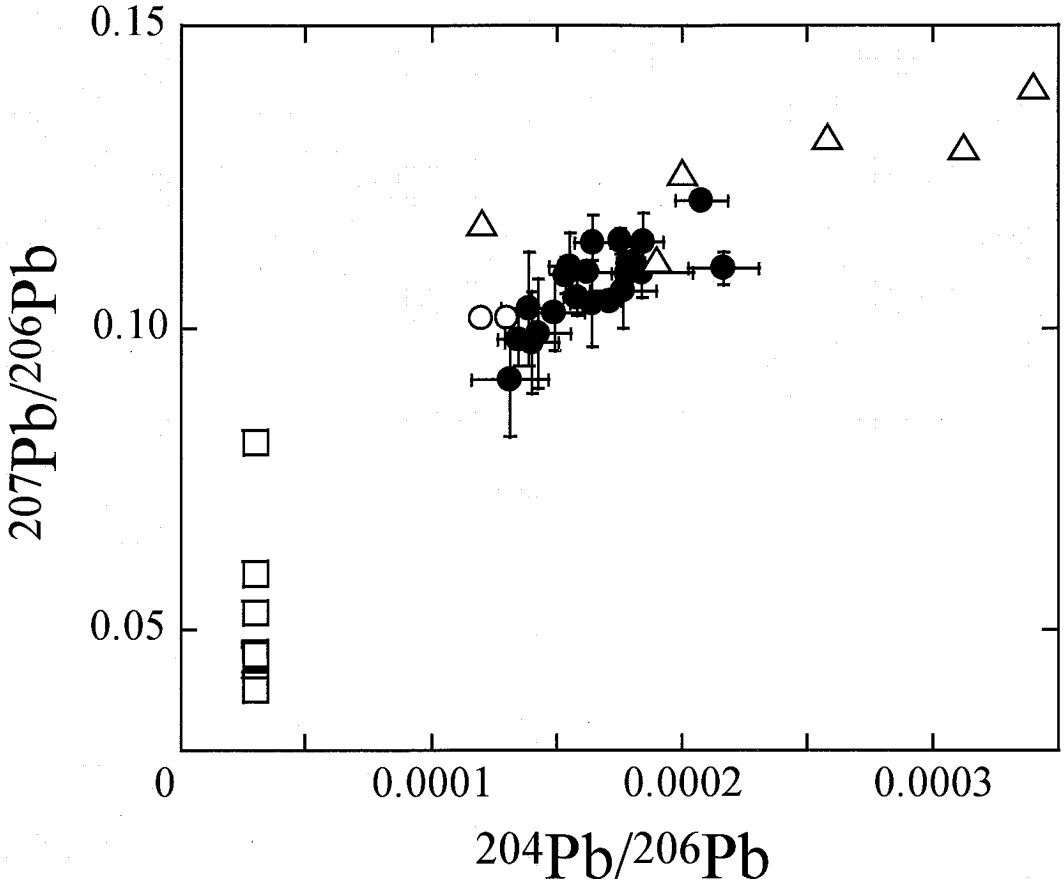

Fig. 22. $^{204}Pb/^{206}Pb$ vs. $^{207}Pb/^{206}Pb$ diagram of the metallic aggregates found in this study (●). For purposes of comparison, the data of uraninite (□) and galena (△) in RZ 13 and metal Pb (○) in RZ10 (Gauthier-Lafaye et al., 1996) are also shown.

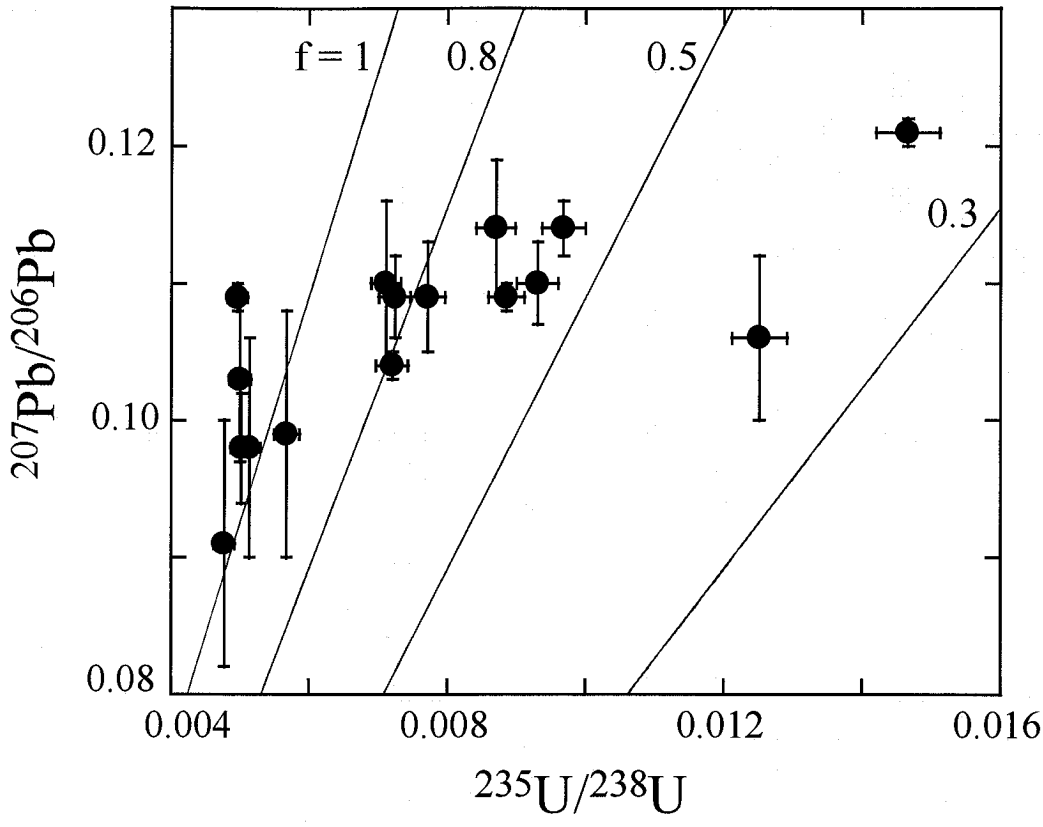

Fig. 23. $^{235}U/^{238}U$ vs. $^{207}Pb/^{206}Pb$ diagram of the metallic aggregates found in this study. "f" values in the figure show proportion of the non-fractionated U and Pb component relative to the total fraction. The definition is described in the text.

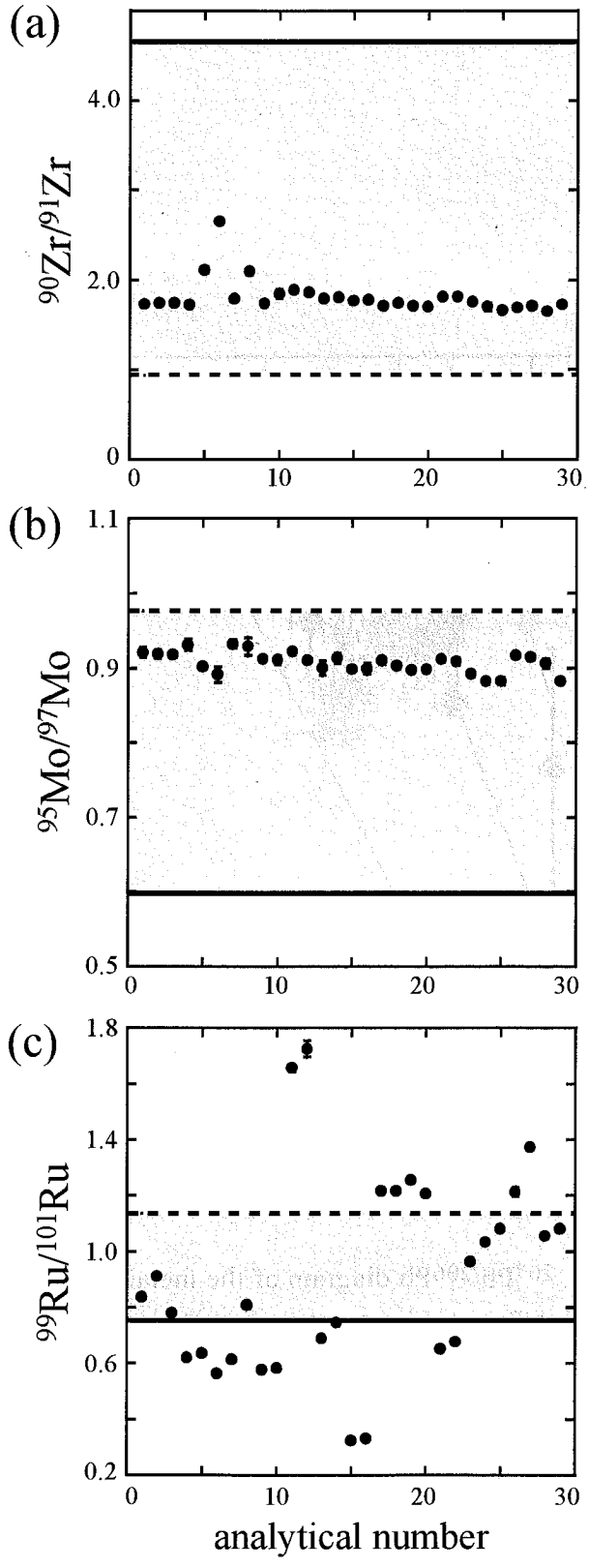

Fig. 24. Isotopic ratios of $^{90}Zr/^{91}Zr$ (a), $^{95}Mo/^{97}Mo$ (b) and $^{99}Ru/^{101}Ru$ (c) for the metallic aggregates analyzed in this study. The isotopic data in each figure are lined up in chronological order and the corresponding analytical numbers in (a), (b) and (c) mean the same analytical spots in SHRIMP analyses. The dotted lines in each figures show the isotopic ratios of fissiogenic Zr, Mo, Ru (0.9456, 0.9768 and 1.136). On the other hand, the solid lines show those of non-fissiogenic Zr, Mo and Ru determined from the standard material (4.659±0.004, 0.5986±0.0002 and 0.7550±0.0005). The shaded area indicates the expected isotopic ratios that could result from a mixing between fissiogenic and non-fissiogenic Zr, Mo and Ru.

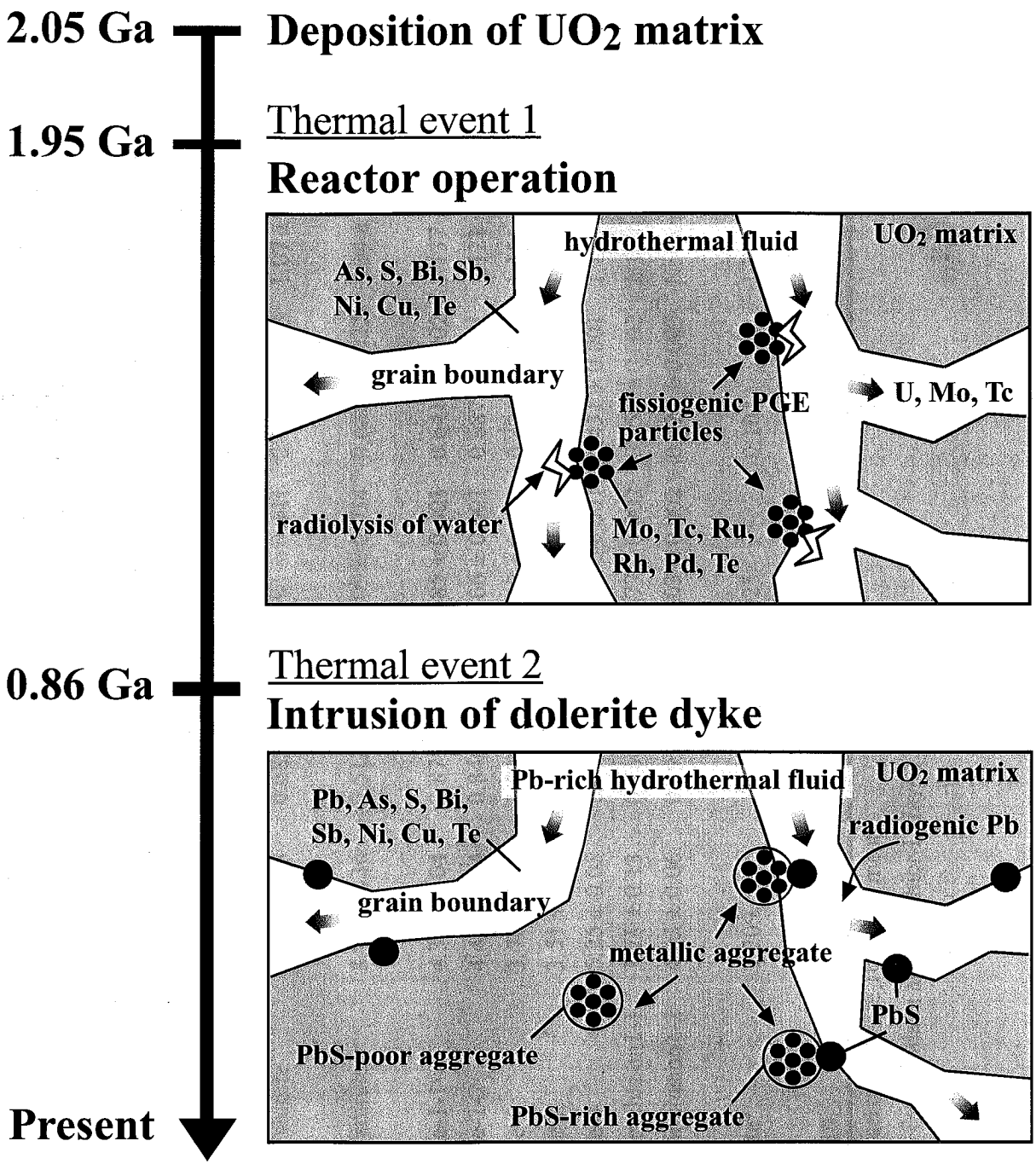

Fig. 25. Formation processes of the metallic aggregates in SD37-S2/CD (RZ13).

Table 1. REE isotopic ratios of micro-minerals by SHRIMP analyses.

(A) Ce, Nd, Sm and Eu isotopic ratios

	$^{140}Ce/^{142}Ce$	$^{143}Nd/^{146}Nd$	$^{145}Nd/^{146}Nd$	$^{149}Sm/^{147}Sm$	$^{153}Eu/^{151}Eu$
BAX3.1040					
micro-uraninite	6.64 ± 0.33	0.682 ± 0.038	0.581 ± 0.041	0.796 ± 0.003	1.07 ± 0.03
BAX3.1040					
micro-uraninite	8.07 ± 2.36	0.513 ± 0.056	0.509 ± 0.034	0.688 ± 0.022	1.14 ± 0.05
BAX3.1170					
coffinite-1-1	4.31 ± 0.04	0.875 ± 0.002	0.585 ± 0.001	0.641 ± 0.002	1.137 ± 0.003
coffinite-1-2	4.49 ± 0.04	0.846 ± 0.002	0.566 ± 0.001	0.687 ± 0.001	1.121 ± 0.002
coffinite-2	3.76 ± 0.07	1.028 ± 0.003	0.689 ± 0.001	0.425 ± 0.001	1.151 ± 0.001
coffinite-3	3.51 ± 0.23	1.017 ± 0.006	0.681 ± 0.001	0.447 ± 0.001	1.147 ± 0.001
coffinite-4	5.25 ± 0.05	0.983 ± 0.002	0.663 ± 0.001	0.431 ± 0.001	1.139 ± 0.004
U-rich inclusion1-1	3.71 ± 0.13	0.966 ± 0.002	0.677 ± 0.002	0.457 ± 0.002	1.149 ± 0.002
U-rich inclusion1-2	4.43 ± 0.06	0.893 ± 0.001	0.603 ± 0.002	0.627 ± 0.003	Not analyze
BAX3.1180					
uraninite*	2.209	1.464	1.025	0.101	1.23
STD					
NIST610	7.73 ± 0.03	0.735 ± 0.001	0.661 ± 0.002	0.906 ± 0.002	1.092 ± 0.002

Analytical uncertainties are 1σ of the mean.

*The data are from Hidaka and Gauthier-Lafaye (2000).

Table 1. continued.

(B) Gd isotopic ratios

	$^{155}Gd/^{160}Gd$	$^{156}Gd/^{160}Gd$	$^{157}Gd/^{160}Gd$	$^{158}Gd/^{160}Gd$	$(^{155}Gd+^{156}Gd)/^{160}Gd$	$(^{157}Gd+^{158}Gd)/^{160}Gd$
BAX3.1170						
coffinite-1-1	0.695 ± 0.05	0.993 ± 0.007	0.700 ± 0.003	1.194 ± 0.004	1.688 ± 0.012	1.894 ± 0.006
coffinite-1-2	0.678 ± 0.07	1.008 ± 0.007	0.706 ± 0.006	1.178 ± 0.006	1.685 ± 0.013	1.883 ± 0.011
coffinite-2	0.710 ± 0.02	0.961 ± 0.003	0.726 ± 0.002	1.139 ± 0.003	1.671 ± 0.004	1.864 ± 0.005
coffinite-3	0.683 ± 0.03	1.030 ± 0.003	0.688 ± 0.003	1.198 ± 0.003	1.712 ± 0.005	1.886 ± 0.005
coffinite-4	0.709 ± 0.08	1.065 ± 0.003	0.707 ± 0.006	1.211 ± 0.008	1.774 ± 0.021	1.917 ± 0.014
U-rich inclusion-1-2	0.732 ± 0.01	1.053 ± 0.011	0.713 ± 0.008	1.200 ± 0.010	1.785 ± 0.022	1.913 ± 0.018
STD						
NIST610	0.710 ± 0.02	0.961 ± 0.005	0.726 ± 0.002	1.139 ± 0.005	1.671 ± 0.006	1.701 ± 0.007

Analytical uncertainties are 1σ of the mean.

The data of micro-uraninite from BAX3.1040 and 1065, and U-rich inclusion1-1 from BAX3.1170 were not obtained.

*The data are from Hidaka and Gauthier-Lafaye (2000).

Table 2. Pb isotopic data of galena in BAX3.1170.

	$^{204}Pb/^{206}Pb$ ($x10^{-4}$)	$^{207}Pb/^{206}Pb$	$^{208}Pb/^{206}Pb$
galena 1-1	4.45 ± 0.05	0.1211 ± 0.0008	0.0197 ± 0.0002
galena 1-2	4.49 ± 0.04	0.1213 ± 0.0009	0.0195 ± 0.0002
galena 1-3	4.46 ± 0.07	0.1213 ± 0.0010	0.0196 ± 0.0002
galena 1-4	4.36 ± 0.03	0.1196 ± 0.0006	0.0193 ± 0.0001
galena 1-5	4.61 ± 0.03	0.1213 ± 0.0006	0.0202 ± 0.0001
galena 1-6	4.42 ± 0.04	0.1203 ± 0.0007	0.0192 ± 0.0001
galena 2-1	4.93 ± 0.11	0.1349 ± 0.0015	0.0216 ± 0.0002
galena 2-2	4.91 ± 0.10	0.1362 ± 0.0010	0.0225 ± 0.0002
galena 3-1	4.01 ± 0.10	0.1187 ± 0.0005	0.0176 ± 0.0002
galena 3-2	4.20 ± 0.06	0.1207 ± 0.0016	0.0184 ± 0.0002
galena 3-3	4.18 ± 0.06	0.1213 ± 0.0009	0.0190 ± 0.0002
galena 3-4	4.09 ± 0.13	0.1212 ± 0.0008	0.0191 ± 0.0003
galena 4-1	4.06 ± 0.12	0.1180 ± 0.0034	0.0170 ± 0.0005
galena 4-2	3.71 ± 0.08	0.1157 ± 0.0008	0.0175 ± 0.0002
galena 4-3	4.21 ± 0.04	0.1190 ± 0.0006	0.0189 ± 0.0001
galena 4-4	4.08 ± 0.10	0.1173 ± 0.0006	0.0183 ± 0.0002
galena 4-5	3.93 ± 0.07	0.1189 ± 0.0005	0.0183 ± 0.0002
galena 4-6	3.98 ± 0.08	0.1183 ± 0.0006	0.0179 ± 0.0002
galena 5-1	4.32 ± 0.10	0.1199 ± 0.0024	0.0187 ± 0.0003
galena 5-2	4.26 ± 0.15	0.1209 ± 0.0025	0.0196 ± 0.0005
galena 5-3	4.22 ± 0.07	0.1225 ± 0.0004	0.0193 ± 0.0001
galena 6-1	4.14 ± 0.06	0.1207 ± 0.0005	0.0188 ± 0.0001
galena 6-2	4.23 ± 0.05	0.1205 ± 0.0004	0.0189 ± 0.0001
galena 6-3	3.95 ± 0.16	0.1158 ± 0.0010	0.0184 ± 0.0003

Analytical uncertainties are 1σ of the mean.

Table 3. REE isotopic data of zircon in BAX3.1170.

(A) Ce, Nd, Sm and Eu

	$^{140}Ce/^{142}Ce$	$^{143}Nd/^{146}Nd$	$^{145}Nd/^{146}Nd$	$^{149}Sm/^{147}Sm$	$^{153}Eu/^{151}Eu$
zircon 1-1	6.68 ± 0.19	0.819 ± 0.02	0.557 ± 0.001	0.765 ± 0.003	1.100 ± 0.006
zircon 1-2	6.07 ± 0.06	0.796 ± 0.02	0.537 ± 0.001	0.811 ± 0.003	1.112 ± 0.002
zircon 1-3	5.79 ± 0.01	0.803 ± 0.01	0.543 ± 0.001	0.790 ± 0.002	1.117 ± 0.003
zircon 1-4	6.09 ± 0.05	0.811 ± 0.01	0.551 ± 0.001	0.756 ± 0.001	1.122 ± 0.001
zircon 1-5	5.53 ± 0.05	0.815 ± 0.01	0.549 ± 0.001	0.752 ± 0.001	1.123 ± 0.002
zircon 2-2	4.92 ± 0.01	0.906 ± 0.01	0.614 ± 0.001	0.606 ± 0.002	1.112 ± 0.011
zircon 3-2	6.03 ± 0.06	0.793 ± 0.01	0.534 ± 0.001	0.808 ± 0.001	1.116 ± 0.002
zircon 3-4	5.97 ± 0.05	0.792 ± 0.01	0.533 ± 0.001	0.801 ± 0.001	1.103 ± 0.004
zircon 4-1	5.44 ± 0.06	0.836 ± 0.01	0.564 ± 0.001	0.699 ± 0.002	1.125 ± 0.002
zircon 5-1	4.27 ± 0.09	0.900 ± 0.03	0.604 ± 0.002	0.606 ± 0.003	1.173 ± 0.003
zircon 6-2	4.60 ± 0.80	0.911 ± 0.03	0.611 ± 0.002	0.573 ± 0.002	1.136 ± 0.001
zircon 7-1	5.05 ± 0.06	0.848 ± 0.02	0.568 ± 0.001	0.693 ± 0.002	1.126 ± 0.002
zircon 7-2	5.09 ± 0.07	0.846 ± 0.01	0.570 ± 0.001	0.673 ± 0.002	Not analyzed
STD					
NIST610	7.73 ± 0.03	0.735 ± 0.01	0.490 ± 0.001	0.906 ± 0.002	1.091 ± 0.001
AS3	7.55 ± 0.06	0.741 ± 0.01	0.484 ± 0.001	0.929 ± 0.001	1.073 ± 0.005

Analytical uncertainties are 1σ of the mean.

Table 3. continued.

(B) Gd

	$^{155}Gd/^{160}Gd$	$^{156}Gd/^{160}Gd$	$^{157}Gd/^{160}Gd$	$^{158}Gd/^{160}Gd$	$(^{155}Gd+^{156}Gd)/^{160}Gd$	$(^{157}Gd+^{158}Gd)/^{160}Gd$
zircon 1-1	0.717 ± 0.009	0.994 ± 0.015	0.738 ± 0.009	1.196 ± 0.014	1.711 ± 0.024	1.934 ± 0.023
zircon 1-2	0.694 ± 0.003	0.985 ± 0.003	0.703 ± 0.003	1.175 ± 0.002	1.678 ± 0.005	1.877 ± 0.005
zircon 1-3	0.694 ± 0.004	0.985 ± 0.003	0.708 ± 0.002	1.176 ± 0.003	1.679 ± 0.006	1.885 ± 0.005
zircon 1-4	0.676 ± 0.002	0.980 ± 0.002	0.698 ± 0.001	1.178 ± 0.002	1.656 ± 0.003	1.875 ± 0.003
zircon 1-5	0.705 ± 0.003	0.982 ± 0.004	0.713 ± 0.003	1.168 ± 0.004	1.687 ± 0.007	1.881 ± 0.005
zircon 2-2	0.719 ± 0.010	0.897 ± 0.028	0.708 ± 0.011	1.208 ± 0.017	1.616 ± 0.028	1.916 ± 0.024
zircon 3-2	0.705 ± 0.003	0.991 ± 0.004	0.704 ± 0.003	1.182 ± 0.004	1.696 ± 0.006	1.886 ± 0.005
zircon 3-4	0.691 ± 0.005	0.979 ± 0.005	0.692 ± 0.005	1.171 ± 0.006	1.670 ± 0.006	1.863 ± 0.010
zircon 4-1	0.696 ± 0.003	1.002 ± 0.004	0.711 ± 0.003	1.191 ± 0.004	1.699 ± 0.006	1.902 ± 0.007
zircon 5-1	0.597 ± 0.007	0.949 ± 0.008	0.662 ± 0.004	1.174 ± 0.004	1.546 ± 0.012	1.837 ± 0.007
zircon 6-2	0.668 ± 0.002	0.976 ± 0.003	0.689 ± 0.001	1.181 ± 0.002	1.643 ± 0.004	1.869 ± 0.003
zircon 7-1	0.695 ± 0.004	0.974 ± 0.004	0.711 ± 0.004	1.156 ± 0.005	1.669 ± 0.004	1.867 ± 0.004
STD						
NIST610	0.710 ± 0.002	0.961 ± 0.005	0.726 ± 0.002	1.139 ± 0.005	1.671 ± 0.006	1.864 ± 0.007
AS3	0.696 ± 0.004	0.960 ± 0.005	0.735 ± 0.005	1.167 ± 0.006	1.656 ± 0.009	1.902 ± 0.010

Analytical uncertainties are 1σ of the mean.

Gd isotopic ratios of zircon 7-2 were not analyzed.

Table 4. U and Pb isotopic data and U contents of zircon in BAX3.1170.

	$^{204}Pb/^{206}Pb$ ($x10^{-4}$)	$^{207}Pb/^{206}Pb$	$^{208}Pb/^{206}Pb$	$^{235}U/^{238}U$ ($x10^{-3}$)	U content (ppm)		$^{238}U/^{206}Pb$
					SHRIMP	EPMA	
zircon 1-1	0.07 ± 0.04	0.1924 ± 0.0013	0.1532 ± 0.0021	7.30 ± 0.08	297	Not analyzed	1.627 ± 0.043
zircon 1-2	4.23 ± 0.12	0.1192 ± 0.0040	0.0194 ± 0.0007	7.37 ± 0.18		874	0.259 ± 0.014
zircon 1-3	4.23 ± 0.22	0.1195 ± 0.0066	0.0274 ± 0.0015	7.33 ± 0.14	1760	Not analyzed	0.516 ± 0.043
zircon 1-4	4.37 ± 0.14	0.1205 ± 0.0032	0.0208 ± 0.0006	7.37 ± 0.16		88.1	1.020 ± 0.111
zircon 1-5	4.35 ± 0.11	0.1195 ± 0.0015	0.0198 ± 0.0003	7.34 ± 0.08		461	0.736 ± 0.043
zircon 2-1	3.65 ± 0.49	0.1397 ± 0.0006	0.0331 ± 0.0004	7.24 ± 0.11	393	Not analyzed	1.025 ± 0.339
zircon 2-2	3.46 ± 0.30	0.1387 ± 0.0028	0.0308 ± 0.0008	Not analyzed	271	Not analyzed	1.018 ± 0.053
zircon 3-1	4.51 ± 0.52	0.1073 ± 0.0160	0.0176 ± 0.0026	Not analyzed	>2500	Not analyzed	
zircon 3-2	4.28 ± 0.33	0.1148 ± 0.0035	0.0336 ± 0.0011	7.34 ± 0.06	>2500	Not analyzed	
zircon 3-3	4.26 ± 0.21	0.1180 ± 0.0048	0.0260 ± 0.0013	Not analyzed	>2500	$3.36x10^3$	1.070 ± 0.089
zircon 3-4	4.15 ± 0.29	0.1165 ± 0.0052	0.0185 ± 0.0008	7.32 ± 0.06	143	Not analyzed	0.233 ± 0.024
zircon 4-1	4.25 ± 0.11	0.1226 ± 0.0034	0.0196 ± 0.0005	7.26 ± 0.04	>2500	Not analyzed	
zircon 4-2	4.42 ± 0.13	0.1202 ± 0.0006	0.0190 ± 0.0001	Not analyzed	>2500	Not analyzed	
zircon 4-3	3.84 ± 0.47	0.1141 ± 0.0047	0.0182 ± 0.0008	7.30 ± 0.08	>2500	Not analyzed	
zircon 4-4	4.50 ± 0.10	0.1199 ± 0.0019	0.0191 ± 0.0003	Not analyzed	>2500	Not analyzed	
zircon 4-5	4.33 ± 0.09	0.1193 ± 0.0020	0.0190 ± 0.0004	Not analyzed	>2500	$7.69x10^3$	0.410 ± 0.010

Analytical uncertainties are 1σ of the mean.

Table 4. continued.

	$^{204}Pb/^{206}Pb$ ($x10^{-4}$)	$^{207}Pb/^{206}Pb$	$^{208}Pb/^{206}Pb$	$^{235}U/^{238}U$ ($x10^{-3}$)	U content (ppm) SHRIMP	U content (ppm) EPMA	$^{238}U/^{206}Pb$
zircon 5-1	4.51 ± 0.15	0.1259 ± 0.0033	0.0206 ± 0.0005	7.30 ± 0.12	>2500	$2.49x10^5$	2.903 ± 0.269
zircon 5-2	4.04 ± 0.67	0.1223 ± 0.0015	0.0202 ± 0.0005	7.27 ± 0.08	>2500	$7.42x10^3$	6.024 ± 0.379
zircon 5-3	4.35 ± 0.35	0.1248 ± 0.0044	0.0182 ± 0.0006	Not analyzed	>2500	Not analyzed	
zircon 6-1	4.27 ± 0.17	0.1223 ± 0.0014	0.0195 ± 0.0003	Not analyzed	>2500	Not analyzed	
zircon 6-2	4.60 ± 0.20	0.1213 ± 0.0047	0.0187 ± 0.0009	7.26 ± 0.08	>2500	Not analyzed	
zircon 6-3	4.86 ± 0.20	0.1220 ± 0.0039	0.0192 ± 0.0007	Not analyzed	>2500	Not analyzed	
zircon 7-1	4.24 ± 0.20	0.1270 ± 0.0005	0.0293 ± 0.0003	7.31 ± 0.08	>2500	$2.69x10^4$	0.229 ± 0.142
zircon 7-2	4.16 ± 0.16	0.1237 ± 0.0007	0.0233 ± 0.0002	7.38 ± 0.04	>2500	Not analyzed	

Analytical uncertainties are 1σ of the mean.

Table 5. Chemical compositions of zircon grains found in the clay layer.

No.	SiO_2	ZrO_2	FeO	Al_2O3	UO_2	MnO	HfO_2	CaO	ThO_2	PbO	Total
BAX3.1170 (clay layer)											
1	31.47	61.68	0.17	0.10	0.06	< 0.01	1.63	0.05	< 0.01	< 0.01	95.15
2	32.13	62.85	0.09	0.01	< 0.01	0.01	1.66	< 0.01	< 0.01	0.05	96.80
3	31.98	61.45	0.09	0.01	< 0.01	0.00	1.61	0.01	< 0.01	< 0.01	95.14
4	31.97	63.45	0.12	0.01	< 0.01	< 0.01	1.73	0.01	0.02	< 0.01	97.30
5	31.93	64.59	0.11	0.02	0.07	< 0.01	1.66	0.01	< 0.01	0.03	98.41
6	30.32	61.69	0.92	0.03	0.08	0.08	1.26	0.38	0.02	0.03	94.80
7	22.52	49.75	0.98	2.45	4.16	0.08	1.10	1.03	0.32	0.26	82.64
8	30.59	62.41	0.51	0.38	0.27	0.05	1.67	0.31	< 0.01	< 0.01	96.18
9	29.39	59.97	1.08	0.67	0.28	0.09	1.58	0.54	< 0.01	0.06	93.65
10	23.44	51.51	1.37	3.39	2.41	0.04	1.15	1.01	0.11	0.62	85.05
11	31.35	63.81	0.26	0.07	0.04	0.02	1.15	0.05	< 0.01	0.04	96.78
12	30.54	61.68	0.71	0.27	0.23	0.05	1.67	0.37	0.03	0.05	95.61
13	25.10	54.55	1.31	1.88	4.44	0.11	1.48	0.63	0.23	0.11	89.83
14	28.10	58.96	0.91	0.99	1.15	0.09	1.43	0.60	0.09	0.07	92.38
15	25.01	55.80	1.29	1.79	4.07	0.11	1.31	0.65	0.26	0.25	90.55
16	30.43	62.13	0.99	0.45	0.14	0.09	1.52	0.59	0.06	0.09	96.48
17	31.98	65.40	0.25	0.17	0.04	0.02	1.36	0.11	0.07	0.04	99.43
18	30.66	61.60	0.74	0.49	0.19	0.06	1.49	0.40	< 0.01	0.02	95.64
19	32.44	61.81	0.09	0.03	0.05	0.01	1.36	0.01	0.00	0.02	95.81
20	18.83	45.51	0.81	2.40	3.99	0.08	0.97	0.91	0.22	0.38	74.10
21	32.24	65.98	0.10	0.01	0.01	< 0.01	1.85	0.01	0.00	0.01	100.20
22	25.19	55.65	0.88	1.48	0.85	0.03	1.83	0.55	0.05	0.20	86.72
23	31.48	63.48	0.41	0.02	0.09	0.02	1.81	0.05	0.03	0.04	97.44
24	32.13	64.58	0.12	0.02	0.01	< 0.01	1.54	0.02	< 0.01	0.01	98.44
25	23.03	51.34	1.09	3.10	2.83	0.03	1.43	0.83	0.16	0.17	84.01
26	30.94	62.72	0.47	0.40	0.18	0.03	1.39	0.20	0.05	< 0.01	96.38
27	19.63	49.31	0.94	2.26	9.15	0.02	1.37	0.50	0.40	0.71	84.29
28	23.43	51.22	1.59	2.87	1.37	0.07	1.18	1.46	0.15	0.09	83.42

Table 5. continued.

No.	SiO_2	ZrO_2	FeO	Al_2O3	UO_2	MnO	HfO_2	CaO	ThO_2	PbO	Total
BAX3.1170 (clay layer)											
29	32.32	64.39	0.10	0.03	0.05	0.01	1.33	0.01	0.02	0.04	98.29
30	22.80	50.16	1.67	3.36	1.83	0.04	1.14	0.83	0.34	0.70	82.86
31	23.05	52.42	1.42	3.32	3.29	0.06	1.20	0.72	0.29	0.82	86.58
32	25.88	53.89	1.37	2.84	2.16	0.04	1.53	1.10	0.20	0.27	89.27
33	30.15	61.61	0.79	0.49	0.29	0.03	1.23	0.32	0.02	0.03	94.96
34	32.65	66.46	0.05	< 0.01	0.05	0.00	1.22	0.01	0.05	< 0.01	100.49
35	30.00	61.04	0.98	0.48	0.12	0.10	1.16	0.61	0.00	0.04	94.53
36	31.92	64.05	0.05	0.00	< 0.01	0.00	1.27	0.01	0.03	< 0.01	97.35
37	32.31	65.72	0.01	< 0.01	0.07	0.01	1.31	< 0.01	0.02	0.04	99.48
38	32.13	65.39	0.03	0.00	0.02	< 0.01	1.18	< 0.01	< 0.01	< 0.01	98.75
39	32.32	65.63	0.04	< 0.01	0.04	0.01	1.19	0.00	0.02	< 0.01	99.25
40	31.75	65.81	0.34	0.01	0.07	0.03	1.22	0.03	0.02	0.07	99.33
41	30.03	62.45	0.88	0.49	0.48	0.08	1.57	0.46	0.02	0.09	96.54
42	32.44	66.06	0.08	0.01	0.07	0.00	1.42	0.01	0.01	< 0.01	100.10
43	28.07	58.20	1.04	0.85	3.45	0.08	1.57	0.56	0.13	0.09	94.04
44	32.28	62.30	0.12	0.01	0.01	< 0.01	0.99	0.01	0.01	< 0.01	95.72
45	31.79	65.14	0.21	0.11	0.10	0.01	1.11	0.08	0.00	0.20	98.75
46	26.69	57.95	1.41	1.72	2.64	0.11	1.33	0.82	0.18	0.29	93.12
47	25.21	54.92	0.95	2.66	2.81	0.05	1.27	0.83	0.19	0.07	88.95
48	23.18	50.71	1.10	2.95	2.95	0.06	1.18	0.95	0.26	0.20	83.52
49	27.67	56.15	0.75	1.39	0.85	0.04	1.42	0.82	0.13	0.06	89.27
50	17.28	35.92	0.87	2.15	25.16	0.04	0.89	0.66	0.93	1.45	85.33
51	32.21	60.97	0.05	0.02	0.02	< 0.01	1.55	< 0.01	0.02	0.01	94.84
52	28.95	56.96	0.71	1.15	1.11	0.06	1.22	0.54	0.10	0.08	90.87
53	24.82	49.02	0.63	1.41	6.33	0.07	1.25	0.74	0.34	0.30	84.89
54	22.75	48.99	1.59	3.56	1.83	0.03	0.91	0.84	0.52	0.64	81.65
55	32.33	62.71	0.06	0.03	0.03	< 0.01	1.63	0.00	< 0.01	0.01	96.81
56	23.03	47.21	1.15	3.15	3.77	0.04	3.32	0.90	0.22	0.09	82.88
57	23.00	49.03	1.18	3.34	3.23	0.05	3.06	0.75	0.52	0.15	84.30

Table 5. continued.

No.	SiO_2	ZrO_2	FeO	Al_2O3	UO_2	MnO	HfO_2	CaO	ThO_2	PbO	Total
BAX3.1170 (clay layer)											
58	32.26	64.64	0.05	0.01	0.04	< 0.01	1.42	< 0.01	< 0.01	< 0.01	98.42
59	32.58	66.03	0.03	0.01	0.03	0.01	1.34	0.01	< 0.01	< 0.01	100.04
60	31.77	64.80	0.21	0.02	0.02	0.01	1.23	0.01	0.02	0.05	98.14
61	30.83	63.68	0.62	0.08	0.14	0.07	1.23	0.26	0.01	0.09	97.02
62	32.36	65.85	0.04	0.01	0.03	0.01	1.39	< 0.01	0.02	0.05	99.75
63	32.43	65.05	0.06	0.01	0.03	0.01	1.33	0.00	< 0.01	0.03	98.93
64	31.38	62.99	0.61	0.09	0.10	0.04	0.92	0.14	0.05	0.02	96.34
65	32.04	64.49	0.17	0.04	0.11	0.03	1.30	0.02	< 0.01	0.06	98.26
66	32.94	66.01	0.12	0.05	0.05	0.00	1.31	0.01	0.03	0.08	100.60
67	21.61	51.52	0.87	3.17	6.70	0.06	1.49	0.83	0.63	1.67	88.55
68	30.35	62.65	0.50	0.42	0.62	0.03	1.22	0.18	0.03	0.22	96.23
69	21.50	50.37	1.20	3.03	5.02	0.06	2.14	0.90	0.37	0.85	85.42
70	28.64	58.27	1.48	1.78	0.42	0.11	1.91	0.94	0.07	0.13	93.76
71	29.00	59.27	1.62	1.48	0.21	0.11	1.70	0.93	0.01	0.08	94.40
72	29.80	60.20	1.15	0.97	0.12	0.10	1.59	0.68	0.04	0.01	94.65
73	27.70	55.76	1.47	3.12	1.46	0.11	1.77	0.95	0.08	0.30	92.72
74	29.19	56.07	1.67	1.92	0.23	0.13	2.47	1.02	< 0.01	0.06	92.76
75	22.39	51.14	1.63	3.26	2.49	0.04	2.37	0.84	0.26	0.77	85.18
76	31.22	62.57	0.81	0.01	0.06	0.07	1.63	0.24	0.01	0.06	96.69
77	25.49	56.19	1.18	2.31	1.50	0.07	1.32	1.01	0.14	0.16	89.36
78	26.76	57.85	1.19	2.09	1.12	0.08	1.22	1.03	0.12	0.18	91.64
79	25.53	54.69	0.90	2.00	1.16	0.07	1.03	1.48	0.15	0.05	87.05
80	31.57	63.65	0.53	0.00	0.02	0.03	2.14	0.01	0.01	0.07	98.02
81	31.06	62.83	0.81	0.01	0.09	0.09	1.65	0.29	0.04	0.06	96.93
82	26.19	55.90	1.39	1.98	1.76	0.05	1.26	0.88	0.15	0.11	89.66
83	29.50	60.11	0.95	0.70	0.30	0.08	1.39	0.56	0.07	0.12	93.78
84	30.59	62.44	0.83	0.24	0.12	0.07	1.29	0.36	0.00	0.09	96.02
85	26.07	55.45	1.53	2.12	0.76	0.07	1.25	1.07	0.22	0.17	88.71
86	28.06	58.84	0.62	1.30	1.59	0.03	1.07	0.43	0.17	0.13	92.24
87	19.73	46.35	0.82	2.83	7.96	0.04	1.46	0.66	0.59	0.16	80.59

Table 5. continued.

No.	SiO_2	ZrO_2	FeO	Al_2O3	UO_2	MnO	HfO_2	CaO	ThO_2	PbO	Total
BAX3.1130 (black shale layer)											
88	23.96	52.91	1.29	2.92	3.11	0.05	1.18	0.81	0.29	0.22	86.74
89	32.06	64.19	0.58	0.24	0.12	0.01	1.19	0.17	0.05	0.01	98.63
90	27.77	55.15	1.44	1.86	0.41	0.10	1.36	1.14	0.09	0.13	89.45
91	21.35	50.63	1.85	2.61	1.25	0.04	1.85	0.95	0.68	0.21	81.42
92	30.06	60.03	1.28	0.19	0.13	0.09	1.76	0.57	< 0.01	0.03	94.14
93	24.38	51.92	1.10	1.96	0.73	0.07	1.54	1.09	0.21	0.21	83.22
94	27.81	56.32	1.32	1.23	0.48	0.07	1.24	0.88	0.25	0.04	89.63
95	31.68	63.39	0.68	0.32	0.15	0.01	1.75	0.19	0.04	0.05	98.26
96	26.28	54.27	1.27	1.83	1.11	0.02	1.51	0.52	0.43	0.15	87.39
97	32.51	64.57	0.10	< 0.01	0.08	0.01	1.44	0.00	0.07	0.08	98.85
98	32.00	64.37	0.28	0.01	0.10	0.01	1.22	0.02	0.02	0.05	98.08
99	32.30	64.05	0.18	0.01	< 0.01	< 0.01	1.36	0.01	0.03	0.02	97.94
100	32.48	63.92	0.24	0.03	0.01	< 0.01	1.23	< 0.01	0.04	< 0.01	97.94
101	32.21	65.26	0.46	0.01	0.03	0.00	1.04	0.01	< 0.01	0.04	99.07
102	23.87	52.27	1.72	2.28	0.81	0.07	1.17	1.14	0.30	0.49	84.13
103	22.65	51.40	2.07	2.68	1.51	0.03	1.06	0.89	0.70	0.62	83.60
104	30.93	62.02	0.77	0.20	0.09	0.03	0.98	0.26	0.03	0.03	95.33
105	29.82	59.78	1.08	0.70	0.12	0.05	0.90	0.40	0.18	0.04	93.06
106	32.57	65.24	0.44	0.03	< 0.01	< 0.01	1.31	0.01	0.01	0.05	99.66
107	24.74	51.54	1.19	2.54	0.93	0.09	1.45	1.16	0.47	1.91	86.02
108	26.16	53.17	0.93	2.05	1.05	0.07	1.50	0.85	0.48	1.50	87.76
109	27.86	57.49	1.10	1.56	0.63	0.07	1.40	0.98	0.23	0.14	91.44
110	32.35	64.17	0.20	0.01	< 0.01	< 0.01	1.33	< 0.01	< 0.01	< 0.01	98.05
111	29.53	58.36	1.04	0.91	0.24	0.09	1.48	0.71	0.04	0.07	92.46
112	26.07	56.14	1.07	1.74	0.77	0.09	1.41	1.35	0.06	0.19	88.88
113	5.60	1.19	74.52	1.93	0.18	0.01	0.02	0.16	0.00	0.56	84.18
114	21.42	48.30	1.78	3.07	1.69	0.04	1.57	1.35	0.80	0.21	80.23
115	22.14	51.23	1.95	2.35	1.62	0.05	1.85	1.64	0.79	0.23	83.84
116	30.77	63.27	1.15	0.09	0.12	0.06	1.25	0.36	< 0.01	0.01	97.08

Table 5. continued.

No.	SiO_2	ZrO_2	FeO	Al_2O3	UO_2	MnO	HfO_2	CaO	ThO_2	PbO	Total
BAX3.1130 (black shale layer)											
117	23.25	49.47	1.54	2.28	1.24	0.06	1.97	0.90	0.56	1.17	82.42
118	25.30	54.68	1.22	2.15	0.91	0.08	1.28	1.21	0.41	0.12	87.35
119	27.19	57.30	1.19	1.46	0.38	0.09	1.34	0.93	0.10	0.15	90.12
120	32.47	65.06	0.40	0.02	< 0.01	0.01	1.42	0.01	0.00	< 0.01	99.39
121	32.27	65.25	0.55	0.00	0.09	0.00	1.59	< 0.01	0.05	0.06	99.86
122	24.85	55.84	1.52	2.07	0.97	0.06	1.76	0.82	0.69	0.17	88.75
123	32.40	65.02	0.17	0.03	0.05	< 0.01	1.34	0.00	0.01	0.03	99.05
124	31.77	65.37	0.25	0.11	0.10	0.01	1.32	0.05	0.00	0.05	99.04
125	32.17	64.81	0.32	0.01	0.02	0.00	1.16	0.01	0.05	0.01	98.55
126	32.55	64.22	0.45	0.03	0.02	0.01	1.35	0.01	0.00	< 0.01	98.63
127	32.17	65.85	0.48	0.02	0.04	0.01	1.06	0.06	0.02	0.01	99.72
128	22.72	50.89	1.89	2.82	1.30	0.04	1.45	0.91	0.74	0.21	82.96
129	26.11	53.42	1.80	2.24	0.79	0.07	1.45	0.91	0.40	0.27	87.46
130	26.57	55.59	1.36	1.81	0.88	0.06	1.45	0.71	0.36	0.24	89.02

All data in weight percent.

Table 6. Ce, Nd, Sm and Eu isotopic compositions in zircon grains found in black shales and clay layers.

	$^{140}Ce/^{142}Ce$	$^{143}Nd/^{146}Nd$	$^{145}Nd/^{146}Nd$	$^{149}Sm/^{147}Sm$	$^{153}Eu/^{151}Eu$
BAX3.1130					
zircon 1-1	6.53 ± 0.89	0.818 ± 0.021	0.535 ± 0.006	0.800 ± 0.015	Not analyzed
zircon 2-2	Not analyzed	0.469 ± 0.034	0.524 ± 0.046	1.653 ± 0.110	1.082 ± 0.002
zircon 5-2	5.06 ± 0.74	0.832 ± 0.010	0.526 ± 0.007	0.794 ± 0.011	1.098 ± 0.004
zircon 6-2	5.06 ± 1.14	0.715 ± 0.010	0.587 ± 0.007	0.818 ± 0.024	1.097 ± 0.002
zircon 7-2	Not analyzed	0.763 ± 0.012	0.530 ± 0.005	0.826 ± 0.006	1.099 ± 0.001
zircon 8-2	6.55 ± 1.05	0.746 ± 0.004	0.499 ± 0.003	0.852 ± 0.009	1.089 ± 0.003
zircon 9-1	6.31 ± 0.49	0.774 ± 0.004	0.507 ± 0.003	0.812 ± 0.006	1.098 ± 0.003
zircon 11-2	4.34 ± 0.28	0.767 ± 0.005	0.514 ± 0.006	0.849 ± 0.003	1.090 ± 0.002
zircon 12-1	5.68 ± 1.06	0.768 ± 0.004	0.509 ± 0.003	0.848 ± 0.006	1.100 ± 0.002
zircon 13-1	3.66 ± 0.12	0.795 ± 0.003	0.517 ± 0.003	0.848 ± 0.004	1.102 ± 0.002
zircon 14-1	5.48 ± 0.30	0.793 ± 0.004	0.526 ± 0.003	0.836 ± 0.013	1.079 ± 0.005
zircon 15-1	3.43 ± 0.25	0.828 ± 0.007	0.531 ± 0.003	0.797 ± 0.017	1.105 ± 0.004
zircon 15-2	Not analyzed	0.861 ± 0.027	0.539 ± 0.008	0.788 ± 0.024	1.108 ± 0.002
zircon 16-1	Not analyzed	0.759 ± 0.010	0.525 ± 0.006	0.801 ± 0.013	1.078 ± 0.005
zircon 17-1	5.42 ± 0.28	0.811 ± 0.009	0.517 ± 0.003	0.815 ± 0.008	1.085 ± 0.002
zircon 18-1	Not analyzed	0.781 ± 0.009	0.483 ± 0.009	0.869 ± 0.011	1.133 ± 0.003
zircon 19-1	7.03 ± 0.56	0.692 ± 0.019	0.492 ± 0.012	0.864 ± 0.022	1.077 ± 0.005
BAX3.1170					
zircon 1-1	3.90 ± 0.33	0.954 ± 0.011	0.625 ± 0.005	0.552 ± 0.006	1.121 ± 0.002
zircon 1-2	4.61 ± 0.08	0.935 ± 0.011	0.649 ± 0.005	0.544 ± 0.003	1.134 ± 0.002
zircon 1-3	4.09 ± 0.49	0.887 ± 0.005	0.600 ± 0.005	0.561 ± 0.003	1.114 ± 0.005
zircon 1-4	3.77 ± 0.14	0.935 ± 0.005	0.635 ± 0.003	0.562 ± 0.007	1.117 ± 0.004
zircon 1-5	3.68 ± 0.17	0.918 ± 0.004	0.624 ± 0.003	0.583 ± 0.004	1.111 ± 0.008
zircon 2-1	3.83 ± 0.34	0.634 ± 0.010	0.591 ± 0.003	0.634 ± 0.008	1.117 ± 0.003
zircon 2-2	3.19 ± 0.49	0.962 ± 0.021	0.610 ± 0.005	0.562 ± 0.009	1.109 ± 0.002
zircon 3-1	4.01 ± 0.22	0.844 ± 0.010	0.543 ± 0.003	0.819 ± 0.010	1.095 ± 0.003
zircon 3-2	7.41 ± 0.22	0.813 ± 0.014	0.549 ± 0.005	0.609 ± 0.012	1.114 ± 0.004

Table 6. continued.

	$^{140}Ce/^{142}Ce$	$^{143}Nd/^{146}Nd$	$^{145}Nd/^{146}Nd$	$^{149}Sm/^{147}Sm$	$^{153}Eu/^{151}Eu$
BAX3.1170					
zircon 3-3	4.10 ±0.28	0.916 ±0.014	0.595 ±0.003	0.631 ±0.007	1.118 ±0.002
zircon 3-4	3.34 ±0.14	0.914 ±0.007	0.600 ±0.003	0.646 ±0.006	1.119 ±0.006
zircon 3-5	8.04 ±2.04	0.840 ±0.020	0.547 ±0.010	0.603 ±0.015	1.100 ±0.009
zircon 4-1	6.24 ±0.38	0.845 ±0.008	0.544 ±0.004	0.683 ±0.008	1.112 ±0.003
zircon 4-2	4.10 ±0.12	0.890 ±0.004	0.597 ±0.004	0.590 ±0.003	1.120 ±0.002
zircon 4-3	3.54 ±0.32	0.892 ±0.013	0.658 ±0.012	0.583 ±0.008	1.116 ±0.002
zircon 4-4	2.86 ±0.10	0.912 ±0.015	0.674 ±0.005	0.626 ±0.004	1.130 ±0.001
zircon 4-5	4.54 ±0.28	0.904 ±0.007	0.602 ±0.003	0.586 ±0.009	1.133 ±0.002
zircon 4-6	5.46 ±0.72	0.842 ±0.198	0.600 ±0.003	0.566 ±0.008	1.100 ±0.004
zircon 5-1	3.57 ±0.09	0.901 ±0.009	0.608 ±0.006	0.608 ±0.008	1.119 ±0.004
zircon 5-2	3.38 ±0.30	0.858 ±0.013	0.583 ±0.004	0.656 ±0.008	1.108 ±0.002
zircon 6-1	3.04 ±0.09	0.598 ±0.010	0.613 ±0.007	0.598 ±0.003	1.139 ±0.003
zircon 6-2	3.09 ±0.20	0.899 ±0.010	0.616 ±0.001	0.660 ±0.008	1.128 ±0.003
zircon 7-1	4.04 ±0.38	0.861 ±0.011	0.570 ±0.005	0.724 ±0.015	1.121 ±0.001
zircon 7-2	5.99 ±0.43	0.820 ±0.006	0.557 ±0.002	0.730 ±0.006	1.113 ±0.002
zircon 7-3	4.86 ±0.32	0.826 ±0.005	0.559 ±0.001	0.749 ±0.004	1.110 ±0.002
zircon 7-4	3.28 ±0.23	0.856 ±0.018	0.601 ±0.005	0.670 ±0.010	1.114 ±0.002
zircon 8-1	4.14 ±0.56	0.870 ±0.018	0.589 ±0.004	0.665 ±0.003	1.113 ±0.001
zircon 8-2	4.62 ±0.17	0.850 ±0.007	0.585 ±0.003	0.683 ±0.007	1.110 ±0.001
zircon 8-3	3.37 ±0.13	0.925 ±0.008	0.622 ±0.005	0.599 ±0.005	1.119 ±0.001
zircon 8-4	4.23 ±0.02	0.868 ±0.003	0.577 ±0.002	0.683 ±0.003	1.119 ±0.002
zircon 8-5	3.51 ±0.11	0.921 ±0.006	0.614 ±0.003	0.609 ±0.004	1.110 ±0.001
zircon 8-6	4.02 ±0.24	0.904 ±0.008	0.604 ±0.003	0.627 ±0.005	1.107 ±0.005
zircon 8-7	3.78 ±0.30	0.903 ±0.007	0.601 ±0.002	0.597 ±0.010	1.106 ±0.003
zircon 9-1	4.82 ±0.13	0.875 ±0.004	0.587 ±0.002	0.625 ±0.003	1.101 ±0.006
zircon 9-2	4.27 ±0.13	0.849 ±0.009	0.565 ±0.003	0.732 ±0.004	1.113 ±0.001
zircon 9-3	3.01 ±0.11	1.004 ±0.009	0.590 ±0.003	0.630 ±0.008	1.131 ±0.004

Table 6. continued.

	$^{140}Ce/^{142}Ce$	$^{143}Nd/^{146}Nd$	$^{145}Nd/^{146}Nd$	$^{149}Sm/^{147}Sm$	$^{153}Eu/^{151}Eu$
BAX3.1170					
zircon 9-4	4.15 ±0.30	0.882 ±0.004	0.600 ±0.002	0.646 ±0.004	1.127 ±0.003
zircon 9-5	5.12 ±0.84	0.899 ±0.009	0.601 ±0.010	0.626 ±0.014	1.121 ±0.003
zircon 9-6	4.00 ±0.36	0.891 ±0.010	0.601 ±0.002	0.622 ±0.006	1.120 ±0.002
zircon 9-7	5.94 ±0.40	0.831 ±0.006	0.562 ±0.002	0.528 ±0.020	1.105 ±0.003
zircon 10-1	5.46 ±0.17	0.846 ±0.009	0.558 ±0.003	0.705 ±0.006	Not analyzed
zircon 10-2	5.84 ±0.35	0.885 ±0.015	0.582 ±0.003	0.659 ±0.007	1.118 ±0.001
zircon 10-3	7.28 ±0.14	0.776 ±0.006	0.517 ±0.003	0.696 ±0.005	Not analyzed
zircon 11-1	3.45 ±0.15	0.903 ±0.005	0.612 ±0.003	0.598 ±0.006	1.117 ±0.006
zircon 12-1	4.48 ±0.52	0.872 ±0.010	0.607 ±0.004	0.589 ±0.005	1.107 ±0.002
zircon 13-1	4.41 ±0.39	0.863 ±0.015	0.564 ±0.005	0.742 ±0.003	1.111 ±0.001
zircon 13-2	4.35 ±0.21	0.880 ±0.004	0.586 ±0.004	0.639 ±0.001	1.120 ±0.002
zircon 13-3	3.97 ±0.08	0.882 ±0.004	0.585 ±0.002	0.657 ±0.005	1.098 ±0.002
zircon 13-4	4.69 ±0.21	0.892 ±0.005	0.600 ±0.001	0.635 ±0.006	1.103 ±0.002
zircon 14-1	6.80 ±1.08	0.731 ±0.036	0.506 ±0.013	0.646 ±0.023	Not analyzed
zircon 16-1	6.79 ±0.28	0.798 ±0.031	0.666 ±0.018	0.577 ±0.009	1.112 ±0.003
zircon 17-1	4.22 ±0.19	0.908 ±0.008	0.586 ±0.002	0.564 ±0.003	1.113 ±0.001
zircon 18-1	6.97 ±0.24	0.759 ±0.021	0.509 ±0.017	0.618 ±0.013	1.123 ±0.002
zircon 19-1	7.73 ±1.47	0.756 ±0.036	0.567 ±0.021	0.593 ±0.014	Not analyzed
zircon 20-1	4.12 ±0.30	0.838 ±0.007	0.568 ±0.002	0.731 ±0.001	1.100 ±0.003
zircon 21-1	4.70 ±0.18	0.853 ±0.004	0.574 ±0.002	0.685 ±0.004	1.093 ±0.003
zircon 21-2	3.55 ±0.43	0.956 ±0.029	0.586 ±0.008	0.604 ±0.005	1.103 ±0.001
zircon 21-3	5.29 ±0.17	0.886 ±0.010	0.612 ±0.005	0.591 ±0.006	1.111 ±0.001
zircon 21-4	3.64 ±0.20	0.903 ±0.009	0.597 ±0.004	0.670 ±0.008	1.129 ±0.003
zircon 21-5	6.79 ±0.78	0.837 ±0.009	0.594 ±0.006	0.656 ±0.007	1.117 ±0.002
zircon 21-6	3.84 ±0.16	0.929 ±0.005	0.516 ±0.013	0.610 ±0.003	1.131 ±0.002
zircon 22-1	6.69 ±0.48	0.846 ±0.007	0.554 ±0.004	0.667 ±0.004	1.106 ±0.001
zircon 23-1	4.23 ±0.12	0.873 ±0.005	0.578 ±0.003	0.673 ±0.007	1.107 ±0.001
zircon 23-2	3.54 ±0.10	0.896 ±0.008	0.585 ±0.003	0.655 ±0.005	1.115 ±0.001

Table 6. continued.

	$^{140}Ce/^{142}Ce$	$^{143}Nd/^{146}Nd$	$^{145}Nd/^{146}Nd$	$^{149}Sm/^{147}Sm$	$^{153}Eu/^{151}Eu$
BAX3.1170					
zircon 24-1	4.21 ±0.15	0.911 ±0.005	0.612 ±0.003	0.587 ±0.004	1.117 ±0.005
zircon 25-1	4.39 ±0.17	0.863 ±0.005	0.594 ±0.001	0.624 ±0.009	Not analyzed
zircon 26-1	0.90 ±0.62	0.903 ±0.009	0.589 ±0.005	0.655 ±0.008	1.119 ±0.001
zircon 26-2	4.88 ±0.20	0.858 ±0.004	0.593 ±0.005	0.638 ±0.003	1.117 ±0.003
zircon 26-3	5.44 ±0.12	0.815 ±0.003	0.539 ±0.002	0.748 ±0.003	1.108 ±0.001
zircon 26-4	5.13 ±0.15	0.815 ±0.004	0.544 ±0.001	0.773 ±0.002	1.103 ±0.001
zircon 26-5	3.01 ±0.13	0.894 ±0.011	0.590 ±0.005	0.724 ±0.006	1.102 ±0.001
zircon 26-6	3.98 ±0.05	0.873 ±0.005	0.578 ±0.002	0.686 ±0.006	1.111 ±0.001
zircon 26-7	5.13 ±0.79	0.869 ±0.017	0.580 ±0.009	0.693 ±0.005	1.099 ±0.002
zircon 27-1	4.97 ±0.23	0.802 ±0.004	0.552 ±0.002	0.736 ±0.004	1.111 ±0.007
zircon 27-2	6.86 ±0.36	0.823 ±0.005	0.520 ±0.013	0.801 ±0.005	1.108 ±0.002
zircon 27-3	4.99 ±0.12	0.828 ±0.007	0.550 ±0.002	0.735 ±0.006	1.105 ±0.001
zircon 27-4	5.41 ±0.14	0.836 ±0.003	0.543 ±0.002	0.743 ±0.004	1.114 ±0.003
zircon 27-5	4.94 ±0.20	0.822 ±0.002	0.545 ±0.002	0.765 ±0.003	1.110 ±0.001
zircon 27-6	5.07 ±0.15	0.833 ±0.003	0.558 ±0.001	0.752 ±0.008	1.103 ±0.003
zircon 27-7	4.90 ±0.19	0.804 ±0.005	0.551 ±0.002	0.750 ±0.002	1.102 ±0.002
zircon 27-8	4.32 ±0.09	0.880 ±0.007	0.579 ±0.002	0.679 ±0.009	1.107 ±0.001
zircon 27-9	6.30 ±0.66	0.809 ±0.009	0.545 ±0.002	0.786 ±0.008	1.100 ±0.003
zircon 27-10	4.99 ±0.12	0.813 ±0.004	0.532 ±0.002	0.737 ±0.006	1.112 ±0.001
zircon 28-1	5.38 ±0.39	0.826 ±0.004	0.564 ±0.002	0.743 ±0.003	1.101 ±0.002
zircon 29-1	3.62 ±0.69	0.815 ±0.015	0.570 ±0.003	0.713 ±0.003	1.119 ±0.002
BAX3.1180					
uraninite*	2.209	1.464	1.025	0.101	1.23
STD					
NIST610	7.23 ±0.11	0.761 ±0.005	0.489 ±0.002	0.898 ±0.006	1.084 ±0.001
AS3	6.86 ±0.14	0.779 ±0.004	0.508 ±0.001	0.938 ±0.003	1.066 ±0.004

Analytical uncertainties are 1σ of the mean.

*The data are from Hidaka and Gauthier-Lafaye (2000).

Table 7. U and Pb isotopic data and U content of zircon in the clay and black shale layers above the reactor

(A) *The analytical data with U concentrations of less than 4000 ppm*

	$^{204}Pb/^{206}Pb$ ($x10^{-4}$)	$^{207}Pb/^{206}Pb$	$^{208}Pb/^{206}Pb$	$^{235}U/^{238}U$ ($x10^{-3}$)	U content (ppm)	$^{238}U/^{206}Pb$
					SHRIMP	SHRIMP
Clay 1						
zircon 1-1	4.27 ± 0.59	0.1009 ± 0.0087	0.0235 ± 0.0016	7.06 ± 0.04	1303	2.069 ± 0.404
zircon 9-1	4.42 ± 0.84	0.1427 ± 0.0172	0.0425 ± 0.0043	7.24 ± 0.04	255	1.891 ± 0.391
zircon 9-2	4.47 ± 0.20	0.1282 ± 0.0022	0.0253 ± 0.0006	7.40 ± 0.08	2111	2.130 ± 0.266
zircon 9-3	3.89 ± 1.09	0.1662 ± 0.0151	0.0651 ± 0.0061	7.22 ± 0.13	155	1.137 ± 0.131
zircon 9-4	4.38 ± 0.32	0.1250 ± 0.0023	0.0250 ± 0.0007	7.00 ± 0.11	2146	3.019 ± 0.222
zircon 9-5	4.06 ± 0.29	0.1269 ± 0.0062	0.0224 ± 0.0012	7.75 ± 0.32	3170	1.744 ± 0.160
zircon 11-1	4.10 ± 0.21	0.1240 ± 0.0030	0.0240 ± 0.0008	6.91 ± 0.20	3991	2.209 ± 0.306
Clay 2						
zircon 1-1	3.93 ± 0.29	0.1122 ± 0.0026	0.0329 ± 0.0018	7.13 ± 0.08	3958	10.681 ± 0.823
zircon 6-1	4.33 ± 0.34	0.1311 ± 0.0043	0.0323 ± 0.0016	7.30 ± 0.05	2909	5.525 ± 0.275
zircon 6-2	4.22 ± 0.69	0.1286 ± 0.0071	0.0393 ± 0.0044	7.23 ± 0.06	1721	2.221 ± 0.554
zircon 6-3	4.47 ± 0.10	0.1189 ± 0.0024	0.0179 ± 0.0006	7.38 ± 0.11	3510	0.048 ± 0.004
zircon 10-1	4.00 ± 0.19	0.1210 ± 0.0048	0.0238 ± 0.0011	6.76 ± 0.07	2906	2.009 ± 0.115
Black shale 1						
zircon 1-1	3.83 ± 0.62	0.1194 ± 0.0045	0.0348 ± 0.0008	7.19 ± 0.06	1515	1.520 ± 0.082
zircon 3-1	3.62 ± 0.38	0.1329 ± 0.0099	0.0341 ± 0.0030	Not analyzed	835	1.910 ± 0.358
zircon 5-1	6.21 ± 0.57	0.1355 ± 0.0052	0.0768 ± 0.0027	7.45 ± 0.25	1286	1.557 ± 0.093
Black shale 2						
zircon 2-1	5.73 ± 0.98	0.1185 ± 0.0142	0.0386 ± 0.0054	7.37 ± 0.05	1668	2.508 ± 0.683
zircon 3-1	5.01 ± 1.01	0.1023 ± 0.0036	0.0284 ± 0.0014	7.51 ± 0.07	2132	1.208 ± 0.142
zircon 5-1	5.23 ± 0.38	0.1140 ± 0.0059	0.0279 ± 0.0015	6.75 ± 0.38	3686	0.876 ± 0.042
zircon 6-1	5.58 ± 0.25	0.1322 ± 0.0006	0.0338 ± 0.0004	7.42 ± 0.18	3165	3.781 ± 0.308
zircon 6-2	6.35 ± 0.24	0.1274 ± 0.0036	0.0299 ± 0.0012	7.22 ± 0.07	2307	0.225 ± 0.027
zircon 7-1	6.73 ± 0.37	0.1344 ± 0.0015	0.0327 ± 0.0009	7.00 ± 0.14	939	0.524 ± 0.089
zircon 8-1	6.01 ± 0.27	0.1370 ± 0.0019	0.0300 ± 0.0005	7.56 ± 0.17	1868	0.422 ± 0.038
zircon 9-1	4.37 ± 0.61	0.1234 ± 0.0040	0.0470 ± 0.0013	7.86 ± 0.12	3439	3.634 ± 0.216
zircon 10-1	4.55 ± 1.12	0.1362 ± 0.0076	0.0521 ± 0.0048	7.02 ± 0.09	668	2.554 ± 0.484
zircon 11-1	5.25 ± 0.51	0.1443 ± 0.0056	0.0510 ± 0.0020	7.49 ± 0.07	895	1.640 ± 0.106

Table 7. continued.

(B) *The analytical data with U concentrations of more than 4000 ppm*

		$^{207}Pb/^{206}Pb$	$^{208}Pb/^{206}Pb$	$^{235}U/^{238}U$ (x10^{-3})	U content (ppm)	$^{238}U/^{206}Pb$
					EPMA	EPMA
Clay 1						
zircon 2-1	4.87 ± 0.26	0.1127 ± 0.0114	0.0226 ± 0.0012	7.35 ± 0.03	36600	14.7 ± 2.5
zircon 3-1	3.74 ± 0.20	0.1162 ± 0.0026	0.0188 ± 0.0004	7.40 ± 0.02	21200	3.58 ± 0.36
zircon 4-1	4.06 ± 0.29	0.1178 ± 0.0073	0.0256 ± 0.0015	7.65 ± 0.03	10100	15.1 ± 0.8
zircon 4-2	4.15 ± 0.20	0.1181 ± 0.0069	0.0220 ± 0.0012	7.68 ± 0.02	35900	15.5 ± 1.4
zircon 5-1	4.20 ± 0.24	0.1206 ± 0.0068	0.0185 ± 0.0012	7.43 ± 0.02	35200	9.87 ± 4.21
zircon 6-1	4.28 ± 0.20	0.1226 ± 0.0047	0.0191 ± 0.0010	7.13 ± 0.02	7510	3.94 ± 0.99
zircon 7-1	4.74 ± 0.44	0.1187 ± 0.0116	0.0200 ± 0.0021	7.31 ± 0.04	24900	15.2 ± 0.4
zircon 8-1	4.24 ± 0.28	0.1170 ± 0.0017	0.0185 ± 0.0005	7.47 ± 0.03	12000	14.7 ± 0.4
zircon 8-2	3.86 ± 0.25	0.1208 ± 0.0033	0.0185 ± 0.0013	7.31 ± 0.03	16100	2.44 ± 0.19
zircon 8-3	4.50 ± 0.25	0.1195 ± 0.0045	0.0182 ± 0.0008	7.48 ± 0.03	29000	3.74 ± 1.84
zircon 10-1	3.67 ± 0.33	0.1165 ± 0.0108	0.0224 ± 0.0018	7.82 ± 0.03	4190	5.20 ± 2.02
zircon 10-2	4.08 ± 0.18	0.1176 ± 0.0026	0.0192 ± 0.0005	7.00 ± 0.02	30400	34.0 ± 2.1
zircon 13-1	2.55 ± 0.28	0.1131 ± 0.0087	0.0196 ± 0.0015	6.89 ± 0.03	24800	38.8 ± 2.8
zircon 13-2	4.31 ± 0.24	0.1208 ± 0.0086	0.0200 ± 0.0009	7.30 ± 0.02	27400	13.1 ± 2.3
Clay 2						
zircon 2-1	2.60 ± 0.36	0.0757 ± 0.0066	0.0141 ± 0.0010	7.44 ± 0.04	9780	12.2 ± 5.1
zircon 3-1	4.71 ± 0.37	0.1201 ± 0.0061	0.0196 ± 0.0011	7.41 ± 0.04	55800	19.6 ± 3.2
zircon 4-1	4.65 ± 0.43	0.1166 ± 0.0121	0.0174 ± 0.0017	7.20 ± 0.04	16100	2.66 ± 0.30
zircon 5-1	3.58 ± 0.12	0.1013 ± 0.0032	0.0168 ± 0.0005	7.46 ± 0.01	28400	19.4 ± 4.9
zircon 7-1	4.14 ± 0.26	0.1169 ± 0.0061	0.0182 ± 0.0009	6.95 ± 0.03	59000	3.71 ± 0.30
zircon 8-1	4.11 ± 0.20	0.1207 ± 0.0068	0.0188 ± 0.0009	7.94 ± 0.02	5440	2.58 ± 0.50
zircon 9-1	3.77 ± 0.52	0.1232 ± 0.0048	0.0196 ± 0.0009	7.72 ± 0.05	44200	5.52 ± 0.50
zircon 9-2	4.14 ± 0.27	0.1193 ± 0.0090	0.0195 ± 0.0014	7.10 ± 0.03	12800	4.59 ± 0.72
zircon 9-3	4.54 ± 0.17	0.1235 ± 0.0047	0.0198 ± 0.0007	7.11 ± 0.02	22000	3.01 ± 0.29
zircon 10-2	4.01 ± 0.26	0.1186 ± 0.0084	0.0223 ± 0.0016	7.25 ± 0.03	15500	15.5 ± 5.1
zircon 10-3	4.14 ± 0.23	0.1203 ± 0.0071	0.0198 ± 0.0011	7.38 ± 0.02	6710	4.20 ± 0.96
zircon 11-1	4.24 ± 0.59	0.1213 ± 0.0076	0.0203 ± 0.0015	6.94 ± 0.06	14000	11.5 ± 3.2
Black shale 1						
zircon 2-1	6.38 ± 0.34	0.1304 ± 0.0037	0.0265 ± 0.0009	7.72 ± 0.03	11000	5.62 ± 1.07
zircon 4-1	5.80 ± 0.20	0.1345 ± 0.0024	0.0269 ± 0.0006	7.66 ± 0.02	7160	1.56 ± 0.18
Black shale 2						
zircon 1-1	5.66 ± 0.37	0.1203 ± 0.0143	0.0226 ± 0.0023	7.41 ± 0.04	9280	0.654 ± 0.054
zircon 4-1	5.80 ± 0.50	0.1284 ± 0.0033	0.0285 ± 0.0009	7.34 ± 0.05	14900	7.69 ± 1.47
zircon 4-2	6.21 ± 0.18	0.1326 ± 0.0029	0.0272 ± 0.0005	7.54 ± 0.02	14300	6.73 ± 1.09
zircon 8-2	5.93 ± 0.26	0.1318 ± 0.0029	0.0278 ± 0.0005	7.96 ± 0.03	8560	5.35 ± 1.13
zircon 12-1	4.96 ± 0.27	0.1229 ± 0.0023	0.0273 ± 0.0006	7.54 ± 0.03	11400	5.69 ± 1.11

Analytical errors are 1σ of the mean.

Table 8. Chemical compositions (weight percentage) of metallic aggregates in SD37-S2/CD.

No.	Ru	Rh	Pd	Te	Pb	U	As	S	Bi	Sb	Ni	Cu	Total
1	49.33	7.06	1.12	4.39	2.66	0.21	14.02	2.21	4.17	0.64	0.61	0.20	86.63
2	58.73	6.97	2.00	2.48	1.46	0.10	9.58	1.68	2.46	0.38	0.53	0.30	86.65
3	48.93	5.21	1.34	3.07	3.20	0.15	20.20	1.63	4.85	0.77	1.15	0.16	90.66
4	56.37	4.38	1.12	2.23	2.74	0.18	15.33	1.26	3.65	0.69	1.23	0.38	89.56
5	61.60	4.99	1.03	2.43	2.11	0.08	11.23	1.54	2.28	0.45	0.85	0.53	89.10
6	61.64	4.13	0.88	2.10	1.59	0.04	9.66	1.52	1.89	0.40	0.89	0.47	85.21
7	50.56	6.74	1.19	4.26	2.72	0.25	14.83	2.07	4.40	0.72	0.64	0.28	88.66
8	49.34	5.69	0.77	4.70	2.57	0.27	14.03	2.33	4.70	0.59	0.58	0.19	85.76
9	35.44	7.66	1.97	4.77	4.31	0.16	24.07	1.39	5.00	0.90	1.08	< 0.01	86.74
10	38.55	7.11	2.02	3.74	4.11	0.25	28.54	1.41	4.04	0.61	1.19	< 0.01	91.58
11	46.16	8.71	1.22	5.23	2.94	0.32	19.57	2.25	5.06	0.76	0.69	0.08	92.97
12	48.77	7.62	1.19	5.10	2.55	0.26	19.19	2.65	4.70	0.68	0.69	0.08	93.46
13	62.34	5.41	0.92	2.99	1.88	0.20	10.97	2.08	2.63	0.31	0.55	0.37	90.64
14	51.10	6.55	1.11	3.45	2.56	0.24	14.93	2.09	3.98	0.60	0.83	0.21	87.63
15	68.98	4.12	1.42	1.62	1.24	0.07	6.36	1.33	1.32	0.25	0.46	0.47	87.65
16	54.26	6.08	1.14	4.26	2.20	0.16	12.09	2.24	4.08	0.49	0.52	0.26	87.78
17	43.81	7.78	1.24	5.93	3.00	0.25	18.85	2.41	5.33	0.75	0.71	0.10	90.14
18	43.85	5.90	1.54	4.21	4.29	0.36	23.36	1.85	5.66	0.69	1.11	0.11	92.93
19	45.03	5.19	1.41	4.14	4.07	0.21	23.46	2.06	5.70	0.71	1.13	0.10	93.18
20	50.79	4.83	1.26	3.54	3.75	0.24	21.23	2.02	3.94	0.68	1.12	0.24	93.63
21	41.84	8.30	1.29	5.23	4.49	0.39	19.89	2.26	7.97	0.70	0.69	0.04	93.08
22	51.87	6.73	1.10	3.61	3.03	0.15	16.74	2.15	5.35	0.66	0.91	0.20	92.51
SD37-S2/CD[a]	33.51	4.64	n.r.	2.71	38.89	0.39	7.99	7.43	n.r.	n.r.	n.r.	n.r.	95.55
SF29[b]	25.06	4.63	n.r.	0.70	20.51	1.42	31.29	11.62	n.r.	n.r.	n.r.	n.r.	95.32

[a]Average chemical composition of metallic aggregates in SD37-S2/CD in previous work. Data are from Hidaka et al. (1999).

[b]Average chemical composition of metallic aggregates in SF29 (RZ10). Data are from Gauthier-Lafaye et al. (1996).

n.r. = no reported.

Table 9. Pb and U isotopic ratios of the metallic aggregates in SD37-S2/CD.

	$^{204}Pb/^{206}Pb$	$^{207}Pb/^{206}Pb$	$^{208}Pb/^{206}Pb$	$^{235}U/^{238}U$	$^{207}Pb/^{206}Pb$[a]	$^{207}Pb/^{206}Pb$[b]	Age (Ma)[b]
SD37-S2/CD							
Metallic aggregate							
1-1	0.000149 ± 0.000012	0.103 ± 0.006	0.00824 ± 0.00050	0.00500 ± 0.00016	0.101 ± 0.010	0.146 ± 0.015	2304 ± 179
1-2	0.000131 ± 0.000015	0.091 ± 0.009	0.00715 ± 0.00072	0.00478 ± 0.00015	0.089 ± 0.013	0.135 ± 0.021	2167 ± 269
2-1	N.A.	N.A.	N.A.	0.00555 ± 0.00017			
3-1	N.A.	N.A.	N.A.	0.00549 ± 0.00016			
3-2	N.A.	N.A.	N.A.	0.00523 ± 0.00015			
4-1	0.000171 ± 0.000005	0.104 ± 0.001	0.00847 ± 0.00009	0.00720 ± 0.00023	0.102 ± 0.003	0.102 ± 0.005	1667 ± 82
5-1	0.000178 ± 0.000006	0.109 ± 0.001	0.00875 ± 0.00007	0.00497 ± 0.00015	0.107 ± 0.004	0.155 ± 0.007	2407 ± 78
5-2	0.000217 ± 0.000014	0.110 ± 0.003	0.00892 ± 0.00023	0.00930 ± 0.00030	0.107 ± 0.007	0.083 ± 0.006	1279 ± 150
5-3	0.000139 ± 0.000011	0.103 ± 0.009	0.00673 ± 0.00059	N.A.	0.101 ± 0.012		
6-1	0.000176 ± 0.000013	0.106 ± 0.006	0.00803 ± 0.00046	0.01252 ± 0.00040	0.104 ± 0.010	0.060 ± 0.006	603 ± 213
6-2	N.A.	N.A.	N.A.	0.00978 ± 0.00031			
6-3	N.A.	N.A.	N.A.	0.00622 ± 0.00020			
8-1	0.000175 ± 0.000004	0.114 ± 0.002	0.00802 ± 0.00014	0.00968 ± 0.00031	0.112 ± 0.003	0.084 ± 0.004	1283 ± 84
8-2	0.000164 ± 0.000007	0.114 ± 0.005	0.00793 ± 0.00030	N.A.	0.112 ± 0.007		
9-1	0.000184 ± 0.000020	0.109 ± 0.004	0.00792 ± 0.00066	0.00771 ± 0.00025	0.106 ± 0.012	0.100 ± 0.012	1626 ± 222
10-1	0.000142 ± 0.000013	0.099 ± 0.009	0.00732 ± 0.00070	0.00568 ± 0.00018	0.097 ± 0.013	0.124 ± 0.016	2012 ± 236
10-2	0.000158 ± 0.000005	0.105 ± 0.003	0.00755 ± 0.00025	N.A.	0.103 ± 0.004		
11-1	0.000185 ± 0.000008	0.114 ± 0.005	0.00856 ± 0.00035	0.00870 ± 0.00028	0.111 ± 0.007	0.093 ± 0.006	1486 ± 132
11-2	0.000164 ± 0.000009	0.104 ± 0.007	0.00791 ± 0.00050	N.A.	0.102 ± 0.009		
12-1	0.000155 ± 0.000008	0.110 ± 0.006	0.00758 ± 0.00040	0.00711 ± 0.00021	0.108 ± 0.008	0.110 ± 0.009	1799 ± 147
12-2	0.000162 ± 0.000003	0.109 ± 0.001	0.00754 ± 0.00008	0.00885 ± 0.00026	0.107 ± 0.002	0.087 ± 0.003	1371 ± 69
12-3	0.000153 ± 0.000004	0.109 ± 0.003	0.00738 ± 0.00021	0.00724 ± 0.00023	0.107 ± 0.004	0.107 ± 0.005	1750 ± 91
12-4	N.A.	N.A.	N.A.	0.00663 ± 0.00021			
13-1	0.000135 ± 0.000008	0.098 ± 0.004	0.00726 ± 0.00033	0.00503 ± 0.00016	0.096 ± 0.007	0.139 ± 0.011	2209 ± 137
13-2	0.000140 ± 0.000011	0.098 ± 0.008	0.00722 ± 0.00065	0.00514 ± 0.00016	0.096 ± 0.011	0.135 ± 0.016	2170 ± 205
14-1	0.000208 ± 0.000011	0.121 ± 0.001	0.00894 ± 0.00009	0.01466 ± 0.00046	0.118 ± 0.006	0.058 ± 0.004	547 ± 136
14-2	0.000180 ± 0.000006	0.111 ± 0.003	0.00827 ± 0.00023	N.A.	0.109 ± 0.011		
SD37-S2/CD2[c]	<0.0005	0.12660	0.01413				
SD37-S2/CD5[c]	<0.0005	0.12590	0.01376				

Analytical errors are 1σ of the mean. N.A. = not analyzed in this study.

[a]Isotopic composition of radiogenic lead. Correction for common lead: $^{206}Pb/^{204}Pb = 18.61$. $^{207}Pb/^{204}Pb = 15.75$. (Mathieu et al., 2001).

[b]Isotopic composition of radiogenic lead and apparent age after correction for ^{235}U depletion and enrichment.

[c]The two data of the metallic aggregates in SD37-S2/CD are from Gauthier-Lafaye et al. (1996).

Table 10. Zr, Mo and Ru isotopic ratios of the metallic aggregates in SD37-S2/CD.

	$^{90}Zr/^{91}Zr$	$^{97}Mo/^{95}Mo$	$^{99}Ru/^{101}Ru$
SD37-S2/CD			
Metallic aggregate			
1-1	1.731 ± 0.005	0.921 ± 0.007	0.838 ± 0.008
1-2	1.743 ± 0.011	0.919 ± 0.006	0.912 ± 0.009
1-3	1.744 ± 0.008	0.918 ± 0.004	0.780 ± 0.008
1-4	1.721 ± 0.006	0.931 ± 0.007	0.620 ± 0.007
2-1	2.113 ± 0.035	0.902 ± 0.004	0.636 ± 0.003
2-2	2.651 ± 0.028	0.891 ± 0.010	0.563 ± 0.006
3-1	1.788 ± 0.010	0.932 ± 0.005	0.614 ± 0.007
3-2	2.093 ± 0.040	0.929 ± 0.011	0.807 ± 0.010
4-1	1.737 ± 0.011	0.912 ± 0.004	0.577 ± 0.006
4-2	1.843 ± 0.051	0.911 ± 0.006	0.582 ± 0.002
5-1	1.887 ± 0.020	0.922 ± 0.004	1.657 ± 0.012
5-2	1.858 ± 0.024	0.910 ± 0.003	1.725 ± 0.029
6-1	1.790 ± 0.010	0.900 ± 0.010	0.689 ± 0.009
6-2	1.801 ± 0.017	0.913 ± 0.007	0.746 ± 0.012
7-1	1.765 ± 0.009	0.898 ± 0.003	0.324 ± 0.001
7-2	1.774 ± 0.007	0.899 ± 0.007	0.331 ± 0.001
8-1	1.708 ± 0.009	0.910 ± 0.005	1.216 ± 0.014
8-2	1.741 ± 0.011	0.903 ± 0.004	1.216 ± 0.004
9-1	1.707 ± 0.005	0.897 ± 0.003	1.256 ± 0.010
9-2	1.698 ± 0.006	0.898 ± 0.003	1.207 ± 0.003
10-1	1.811 ± 0.010	0.912 ± 0.004	0.653 ± 0.003
10-2	1.814 ± 0.002	0.909 ± 0.005	0.677 ± 0.001

Table 10. continued.

	$^{90}Zr/^{91}Zr$	$^{97}Mo/^{95}Mo$	$^{99}Ru/^{101}Ru$
SD37-S2/CD			
Metallic aggregate			
11-1	1.769 ± 0.004	0.817 ± 0.005	1.020 ± 0.016
11-2	1.754 ± 0.006	0.892 ± 0.004	0.963 ± 0.003
12-1	1.702 ± 0.046	0.882 ± 0.004	1.034 ± 0.004
12-2	1.661 ± 0.009	0.883 ± 0.005	1.080 ± 0.005
13-1	1.692 ± 0.004	0.917 ± 0.002	1.214 ± 0.017
13-2	1.708 ± 0.005	0.915 ± 0.004	1.372 ± 0.004
14-1	1.648 ± 0.008	0.906 ± 0.006	1.056 ± 0.008
14-2	1.725 ± 0.010	0.882 ± 0.001	1.080 ± 0.002
SD37-S2/CD.2[a]	N.A.	N.A.	1.9342
SD37-S2/CD.3[a]	N.A.	N.A.	1.5611
SD37-S2/CD.5[a]	N.A.	N.A.	2.2842
STD	4.659 ± 0.004	0.5986 ± 0.0002	0.7550 ± 0.0005
Fissiogenic[b]	0.9456	0.9768	1.136

N.A. = not analyzed.

Analytical uncertainties are 1σ of the mean.

[a]The data of the metallic aggregates in SD37-S2/CD are from Hidaka et al. (1999).

[b]Fissiogenic values are obtained after consideration of the fission yields of nuclides of Zr, Mo and Ru (England and Rider, 1988) and fission contributions of ^{235}U, ^{238}U and ^{239}Pu in SD37-S2/CD (Hidaka et al., 1999).